An Experimental Investigation Into Shock-Induced Panel Flutter

Study into the effect of mean surface deformation and wind tunnel boundary conditions on panel flutter

Master of Science Thesis

Marco Radaelli

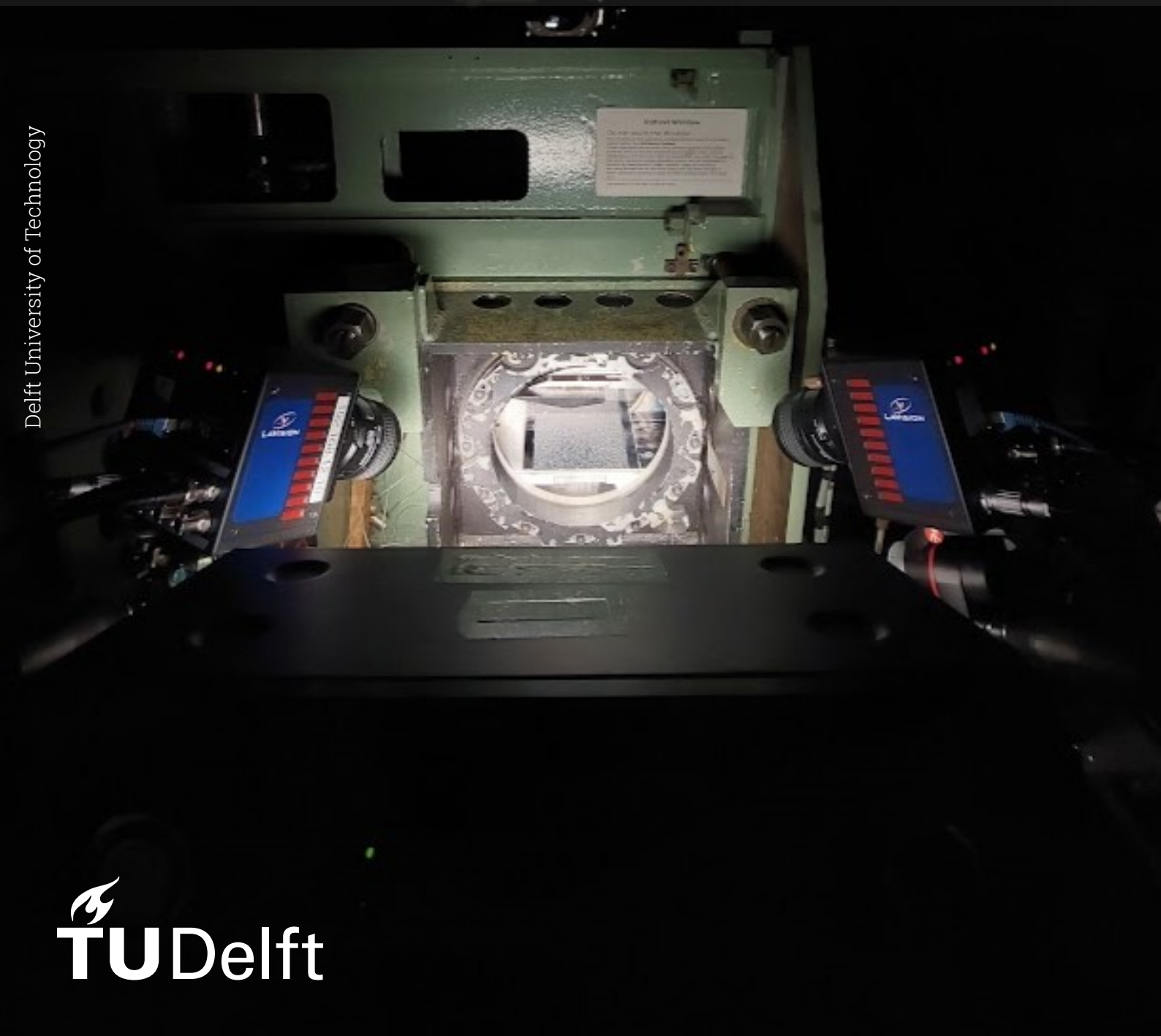

Delft University of Technology

TU Delft

An Experimental Investigation Into Shock-Induced Panel Flutter

Study into the effect of mean surface deformation and wind tunnel boundary conditions on panel flutter

by

Marco Radaelli

to obtain the degree of Master of Science
at the Delft University of Technology,
to be defended publicly on Monday, September 16th, 2024

Student number:	5063973	
Thesis committee:	Dr. S.J. Hulshoff,	TU Delft, chairman
	Dr. J. Sodja,	TU Delft, independent examiner
	Dr. ir. F.F.J. Schrijer,	TU Delft, supervisor
	Dr. ir. B.W. van Oudheusden,	TU Delft, supervisor
Others:	Dr. A. D'Aguanno, MSc,	TU Delft, daily supervisor

TU Delft

Summary

Over the years, the aerospace sector pushes to make everything faster, lighter and more durable, while ensuring reliability and safety. It is therefore unavoidable to arrive at certain limits that may not be understood well yet. In supersonic flight, the heavy vibration of thin-walled structures, more commonly known as panel flutter, is one of these limiting phenomena that is still not understood well enough, while being a critical design factor. In addition to this detrimental fluid-structure interaction (FSI) phenomenon, in the presence of shock waves, this phenomenon is further aggravated by the presence of shock-wave/boundary-layer interactions (SWBLI), of which the underlying mechanism is still debated upon by different research groups. That is why, to achieve faster, lighter and more durable flight, it is of interest to understand the fluttering behaviour of thin-walled panel in supersonic conditions. Recent investigations at Delft University of Technology in the same facility as the current study, the ST-15 wind tunnel, have successfully proven that periodicity and repeatability of the FSI phenomenon in this facility, while at the same time encountering challenges with the wind tunnel boundary conditions. Furthermore, numerical studies have made the effort to look at the difference between static and dynamic deformations of these panel structures.

Based on the recent efforts as described above, the aim of this study is to experimentally investigate the effect of static and dynamic panel deformation on the FSI in the case of shock-induced panel flutter. Great part is also to characterise the wind tunnel boundary conditions, such that a greater understanding of the facility can be obtained for FSI studies. The experiments are done at a freestream Mach number of 2.0 and a total pressure of 2.5 bar. Furthermore, the shock generator has a flow deflection angle of 12° and the inviscid shock impingement point on the panel is taken at the 55% point in streamwise direction. Three different cavity closure conditions have been investigated: an open cavity, a closed cavity and a ventilated cavity. The latter case consists out of a closed cavity but with nine little holes present in the plate closing off the cavity, such that the pressure is equal to the open-cavity case, but strong pressure waves are not able to enter it. Pressure measurements are performed to document the cavity pressure and relate the static panel deformations to this quantity, while some qualitative measurement techniques such as schlieren and oil flow visualisation help to give a general understanding of the flow field organisation. Temperature measurements are performed with an infrared camera and several thermocouples to document the temperature response of the panel. DIC and PIV experiments are also used for measuring the panel response and the flow behaviour on top of the panel, respectively.

Oil flow visualisation measurements have confirmed the typical three-dimensional flow structure of a SWBLI within a closed environment such as a wind tunnel, in particular when looking at the shape of the separation bubble at the panel surface. Furthermore, the cavity closure condition has been shown to have a significant effect on the panel response behaviour. The first effect it has, is the value of the cavity pressure: an open cavity results in a lower cavity pressure with respect to a closed one. Hence, for the open-cavity case, the mean deformation of the panel is also more downward with respect to the closed-cavity case. Furthermore, spectral and POD analysis show that for an open cavity, the panel response is dominated by a resonance phenomenon, forced by strong pressure waves entering the cavity. The presence of these waves is confirmed by schlieren experiments. For the ventilated cavity, these waves are not present, thus the oscillation amplitude of the panel becomes lower and the frequencies at which it vibrates are different. Furthermore, a phase-averaging analysis confirmed the division of the flutter motion into four clear phases, of which the shapes are mainly dominated by first bending modes. In addition to this, temperature effects have been found to not be entirely negligible over time as both panel temperature and mean panel deformation where found to change over time.

The flow field data on top of the panel shows that compared to a rigid flat plate, the dynamic behaviour of the flexible panels causes the separation area to increase. However, different from what was expected, the rigid deformed panel, which has the same mean shape as the flexible panels, resulted in a shifted mean flow organisation, as well as an even more increased separated area. At the same time, as the ventilated case, with a lower dynamic response compared to the open-cavity case, was found to have almost the same mean flow characteristics, thus making a case that it show the actual convergence to a rigid deformed case. That is why it is suggested for additional experiments and more care and time to the manufacturing of the rigid deformed panel, as inconsistencies in this panel could be the cause of the observed discrepancies. This shows again the importance of the understanding of the experimental conditions (including the test model) in order to be able to separate the physical FSI phenomena from external factors, in particular the wind tunnel vibrations.

Acknowledgements

"True education is a kind of never ending story — a matter of continual beginnings, of habitual fresh starts, of persistent newness."

– J.R.R. Tolkien

Sometimes all it takes is a good night's sleep. Especially when you work on the same subject for 8 months, it is not a matter of if but of when you will get stuck. When that happens, even a good night's sleep is not enough. That is why here I want to take a moment to thank all the people that have provided me with continuous fresh starts, which led to this wonderful thesis period.

First of all, my gratitude goes to my supervisors, Ferry, Bas and Alessandro, for giving me the chance to work on this amazing thesis and to learn from them to become a better researcher. I truly could not have wished for better supervisors with their assistance, critical thinking and suggestions.In particular, I am eternally grateful to Alessandro, who has given so much of his time to help out when all hope seemed lost; I am truly sorry for all my appearances at your office! A special thanks to Luis Laguarda for the inspiration to the one of the aspects this thesis and for all the help and enthusiasm. Also a special thanks to Jane for the help with setting up the PIV system within 1 single day; without your help, those experiments would not have been possible! I would also thank all the technicians that have helped me and have shown interest in my work: Gert-Jan, Dennis, Peter, Frits, Henk-Jan and Stefan. I learned so many practical things from all of you, which I will always remember and appreciate; it was a huge pleasure to work with all of you. Rest assured: I won't haunt you down the lab anymore to ask if you have some time to test! Special thanks to Ed, Rob and Peter from DEMO for their help in making the new panels and the designed holder for my 3D-prints.

I have also had the pleasure to share this period with an amazing group of friends: Edoardo, Francisco, Rodrigo, Alex and Nicholas. Part of what made this period so awesome was all of your company from lunches and coffee breaks to philosophical conversations and so much more! You have all been as a light in the dark basement of the HSL and made me want to come in and work, even when the motivation would be very low at times. I wish you all the best for your future, wherever that will be!

I also want to particularly thank my catholic community in Uithoorn: Gerard, Mariusz, Marco, Philippe & Iva, Bert & Atie, David & Ellen, Luc & Marília, Jan & Elisabeth, Ricardo & Evelyn, Huy & Linh, Herman, David R., Daniel, David Z., Dameria, Consuelo, Eleonore and Miriam. For me you have been truly a cornerstone for my life in these months, even when certain periods would never seem to end or when things did not always seem to go the way I wanted. Thank you for all your prayers!

A special thanks goes to my family, and in particular to my parents, for always supporting me in my studies, for all your encouragements and opinions, for all the meals, for a roof above my head, for helping me in my faith, and for teaching me to dream big! I also want to thank my girlfriend Jazmin, for being truly an amazing person. I thank you for all your support, interest and patience in these months, in particular for the busier periods. After all these months you might consider yourself an expert on shock waves and panel flutter too! Thank you for all your love and happiness you give me in life!

My final praise goes to God! Through all of these years, You have provided to me in ways I did not even think of. "*A te solo, buon Signore, si confanno gloria e onore. A Te ogni laude et benedizione.*"

Marco Radaelli
Delft, August 2024

Contents

List of Figures

List of Tables

Nomenclature

Abbreviations

Abbreviation	Definition
AR	Aspect ratio
CCCC	Fully clamped panel
CCFF	Clamped panel, free at sides
DIC	Digital image correlation
DNS	Direct numerical simulation
DOF	Depth of field
DR	Data rate
FOV	Field of view
FSI	Fluid-structure interaction
HSL	High Speed Laboratory
IR	Infrared Imaging
LCO	Limit cycle oscillation
LES	Large eddy simulation
LSM	Least-squares method
OFV	Oil flow visualisation
OMA	Operational modal analysis
PIV	Particle image velocimetry
POD	Proper orthogonal decomposition
PSD	Power spectral density
PSP	Pressure sensitive paint
PTU	Programmable Timing Unit
RANS	Reynolds-averaged Navier-Stokes
SSME	Space Shuttle Main Engine
SWBLI	Shock-wave/boundary-layer interaction
TC	Thermocouple

Symbols

Symbol	Definition
A_{sep}	Separation area
a	Panel length
a_j	POD temporal mode
a_p	Particle acceleration
b	Wien's displacement constant
C	Time coefficient matrix
c	Local light speed
c_0	Light speed in vacuum
D	Panel flexural stiffness
d_c	Orifice cavity diameter
d_p	Particle diameter
d_s	Orifice diameter
E	Young's modulus / Energy
E_σ	Seebeck emf
f	Focal length/frequency
$f_\#$	F-stop of camera
h	Panel thickness
K	Gladstone-Dale constant
k	Spatial resolution of image
L_{int}	Interaction length
L_{sep}	Separation length
l_s	Orifice depth
M	Magnification factor
M_∞	Freestream Mach number
N	Number of samples
N_t	Number of snapshots in time
n	Refractive index
P	Power spectral density
P_{sep}	Separation probability
p_0	Total pressure
p_1	Static pressure incoming freestream flow
p_c	Cavity pressure
p_{mw}	Measured wall pressure
p_w	Wall pressure
q	Dynamic pressure
q_f	Flutter dynamics pressure
R	Gas constant
Re_∞	Freestream Reynolds number
S_k	Stokes' number
S_L	Strouhal number
T	Static temperature
T_0	Total temperature
T_f	Frame temperature
T_p	Panel temperature
U	Velocity / Snapshots matrix

Symbol	Definition
U_∞	Freestream flow velocity
U_{slip}	Slip velocity
W_t	Width wind tunnel test section
x_{imp}	Streamwise shock impingement location
x_n	Signal function
x_{refl}	Reflected shock wave location
z	Out-of-plane panel displacement
z'	Out-of-plane panel fluctuation around the mean
z_{avg}	Average out-of-plane panel displacement
γ	Heat capacity ratio
Δp_w	Wall pressure variation
ΔT	Difference between panel and frame temperature
Δt	Pulse separation time
δ_{99}	Boundary layer thickness
δ_t	Pulse separation time of laser
δ_z	Depth-of-field
ϵ	root-mean-square height of orifice burs / uncertainty
ϵ_{cc}	Cross-correlation uncertainty
ϵ_{corr}	Cross-correlation uncertainty related to PIV
ϵ_{slip}	Uncertainty due to slip velocity
θ_{SG}	Shock generator angle
λ	Non-dimensional dynamic pressure / laser wavelength
λ_j	Eigenvalue POD
λ_{max}	Wavelength of maximum spectral emittance
μ	Dynamic viscosity
ν	Poisson's ratio
Π	Non-dimensional wall pressure variation
ρ	Local density
ρ_p	Particle density
ρ_∞	Freestream density
σ	Seebeck coefficient / standard deviation
τ_f	Flow characteristic time scale
τ_p	Particle response time
τ_w	Wall shear stress
ϕ_j	POD spatial mode

1

Introduction

For many years the aerospace sector has embraced the challenge to make everything faster, lighter and more durable. At the same time, it has sought to keep flights reliable and safe. That is why supersonic flight has gained a lot of interest in the fundamental understanding of its extreme conditions and the phenomena involved in this flight regime. In the pursuit of lighter structures, a common solution is to make the structures thinner; in particular, the skin, which is in contact with the airflow, is made as thin as possible. However, when putting these thin-walled structures in supersonic flow, often characterised by shock and expansion waves, a phenomenon known as *shock-induced panel flutter* appears. This interaction between the fluid and the thin structure is periodic and amplifies the loads on the structure. This, in turn, can decrease the structure's lifespan due to acoustic or resonance fatigue (Spottswood et al., 2019), highlighting the previously mentioned challenge of improving the durability of aerospace structures. An example of the consequence of such fatigue loads is shown in Figure 1.1, where it becomes evident how significant of an impact panel flutter can have.

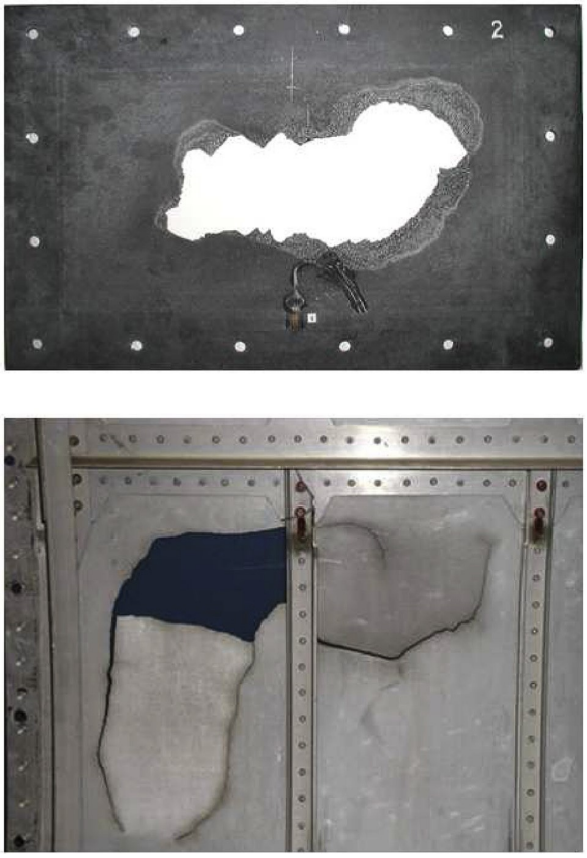

Figure 1.1: Panel failure due to dynamic resonant fatigue loads on a ceramic matrix composite (upper) and C-130 aluminium (lower) panel (Spottswood et al., 2019).

The presence of the aforementioned thin-walled structures, in combination with the presence of shock wave structures in supersonic flow, can be found in several applications. First of all, already on the German V-2 rockets in World War Two, panel flutter phenomena where observed. Since then, effort has been put into the understanding of these phenomena in various applications, such as the rockets of the Apollo missions (Dowell & Bendiksen, 2010). Furthermore, Pasquariello (2018) showed how at engine start-up of the Space Shuttle Main Engine (SSME), the formation of this interaction causes non-symmetrical pressure behaviour (see Figure 1.2) that excites the structure of the relatively thin nozzle structure; this excitement of the structure is unsteady in nature. These examples show that to achieve faster, lighter and more durable flight, in particular for commercial applications, it is important to continue to investigate the mechanisms involved in shock-induced panel flutter. For thin-walled structures, it is specifically relevant to understand the coupling between the flow and the structure: the *fluid-structure interaction*.

Figure 1.2: Transient start-up of the SSME. Figures obtained from NASA (Pasquariello, 2018).

Large part of this shock-induced panel flutter, is the presence of the interaction between the shock waves and the viscous region near the surface of an object called the boundary layer. This interaction, the *shock-wave/boundary-layer interaction* (SWBLI), is an important driving factor in the design of supersonic and hypersonic vehicles (Babinsky & Harvey, 2011). Examples of where this is relevant in the design of such vehicles are highlighted in Figure 1.3, where it is shown that in particular the intake of a supersonic engines can be quite sensitive to the presence of these SWBLIs, and therefore necessitate particular attention for an efficient design.

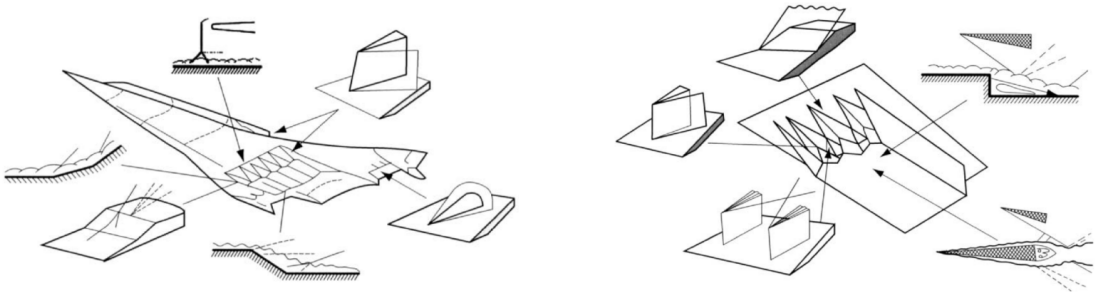

Figure 1.3: Examples of Shock-Wave/Boundary-Layer Interactions in supersonic vehicle design (Babinsky & Harvey, 2011).

Over the past years, both numerical and experimental research on shock-induced panel flutter and fluid-structure interaction has been conducted at the Delft University of Technology using a panel with a thin, rectangular portion (Aditya, 2022; Allerhand, 2020; Laguarda et al., 2024). In particular, numerical research conducted by Laguarda et al. (2024) investigated the effect of the mean deformation of the panel on the fluid-structure interaction between the flow and the panel. They conclude that the general shock structure caused by the SWBLI, is driven by the mean deformation of the panel. This could be

the basis for finding a passive flow control mechanism to counteract the undesirable features of SWBLIs. The validation of these findings in an experimental environment, together with a continuation of experimental work in this area, form the basis for this study.

The aim of this study is *the experimental investigation into the effect of static and dynamic panel deformation on the fluid-structure interaction in the case of shock-induced panel flutter*. In addition to this, effort is put into the characterisation of the wind tunnel boundary conditions for this condition, which are specifically inherent to the ST-15 supersonic wind tunnel facility at the Delft University of Technology. In order to accomplish this research objective, a couple of research questions are formulated, which serve as a backbone for the current study:

1. How do mean and dynamic panel deformation affect the fluid-structure interaction in the case of shock-induced panel flutter?
2. To what extent do the boundary conditions present in the ST-15 wind tunnel environment influence the fluid-structure interaction in the case of shock-induced panel flutter?

For the second research question, some specific boundary conditions are considered, namely the confinement by the wind tunnel walls, temperature and the cavity closure condition.

This document is structured as follows: in chapter 2, a review is presented of the literature relevant to the current research. Specifically, the mechanisms behind the important phenomena, such as SWBLI and (shock-induced) panel flutter, are introduced. Furthermore, a brief summary is given of the latest research conducted at the Delft University of Technology itself related to these subjects (see section 2.3). In chapter 3, the experimental setup is described, consisting out of a description of the wind tunnel itself, as well as the experimental techniques used in this wind tunnel environment to answer the research questions. In chapter 4, the processing techniques used in the current research are presented, which aids in the repeatability of the research and to show how the results presented in the subsequent chapters are obtained. In chapter 5, the second research question is addressed in more detail by the investigation and presentation of the panel oscillation behaviour. Furthermore, in chapter 6, findings related to the first research question are presented, aiming to understand how static and dynamic deformations affect the flow on top of the panel. Finally, the major conclusions from this research are given in chapter 7, as well as recommendations for future studies on this topic in the ST-15 wind tunnel facility.

2

Literature Review

In this chapter, a literature review on the background of the phenomena involved in shock-induced panel flutter is presented. This literature review aims to provide a foundation for the rest of the study, to identify knowledge gaps in the research area and finally to justify the research objective and questions formulated in chapter 1. As the baseline structure considered for the study consists out of a rigid panel without any flutter, it is important to understand the underlying mechanisms of a shock-wave/boundary layer interaction (SWBLI), as discussed in section 2.1. Once this concept is understood, it is possible to include the flutter phenomena to the SWBLI and how the different parameters involved could influence the interaction (see section 2.2). As the interaction does not only consists out of the flow, attention is also given to the panel oscillations. Finally, as the current study builds upon previous studies performed at the Delft university of Technology, the relevant results from those studies are discussed in section 2.3.

2.1 Shock-Wave/Boundary Layer Interactions

Flow around objects in supersonic flows is characterised by the presence of shock waves. As described by Délery and Dussauge (2009), these shock waves are caused "either by a change in the slope of a surface, a downstream obstacle or a back pressure constraining the flow to become subsonic". At the same time, a thin flow region close to the surface, where the flow is considered to be viscous, is recognised, which is called the *boundary layer* (Anderson, 2017). Even though the boundary layer is very thin compared to the rest of the flow, this region has a big impact on the flow behaviour and structures present around the object. The interaction between the two phenomena mentioned above is called *shock-wave/boundary layer interaction* (SWBLI). The shock causes a decrease in velocity and an increase in pressure, temperature and density, the amount of which is dependent on the strength of the shock. Therefore, shock waves serve as adverse pressure gradients, thickening or even separating the boundary layer flow, which in turn increases the dissipation within the flow (Sabnis & Babinsky, 2023). That is why for the current study it is important to study this phenomenon more in-depth, covering the two- and three-dimensional structure of SWBLIs (subsection 2.1.1) in the presence of an impinging oblique shock wave, as well as the unsteady behaviour of this phenomenon (subsection 2.1.2).

2.1.1 Two- and Three-Dimensional Structure of SWBLIs

Two-Dimensional Structure

The flow properties after a shock, compared to the properties upstream of the shock, are dependent on the strength of the shock wave. Similarly, the boundary layer properties are also different for different flow conditions. Thus, the exact flow structure of a SWBLI varies based on the conditions mentioned above. However, a general structure can be observed. Consider a two-dimensional case, as presented in Figure 2.1, where, similar to the current study, there is a flat surface with an impinging shock.

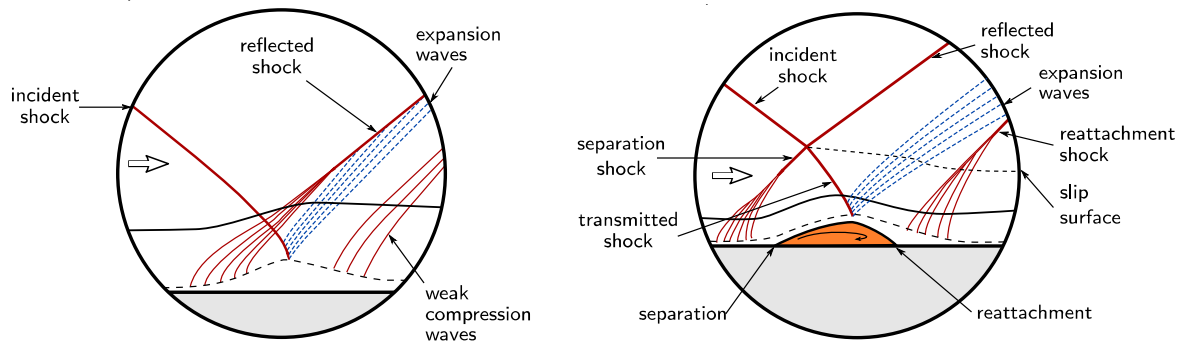

(a) SWBLI for an attached oblique shock reflection.

(b) SWBLI for a separated oblique shock reflection.

Figure 2.1: Schematic wave patterns for attached and separated flow fields corresponding to the oblique shock interaction (adapted from Sabnis and Babinsky (2023)).

For a weak shock, the flow field remains attached, such as shown in Figure 2.1a. This figure shows that because of the viscous interaction with the boundary layer, a subsonic region under the shock structure is created, feeding pressure information upstream, causing the pressure rise to be smeared over a larger region compared to the inviscid solution (Sabnis & Babinsky, 2023). The separation line (dotted line in the figure) between subsonic and supersonic flow is called the sonic line. As a response to the pressure rise, the boundary layer thickens, leading to the creation of subsequent compression waves. At some point, the flow turns back towards the surface, leading to the formation of expansion waves. Again because of some streamline curvature, some compression waves are created downstream.
Consider now the case where the shock is stronger, leading to flow separation, as visualised in Figure 2.1b; now a separation bubble is present underneath the shock structure. The shape of the separation bubble determines the wave pattern above it, consisting out of compression and expansion waves (Sabnis & Babinsky, 2023). Again, because of the subsonic region, pressure information is fed upstream, the separation takes place at a more upstream location compared to the inviscid solution (Anderson, 2017). A second shock wave is created at the separation because of external supersonic flow being deflected into itself by the boundary layer: the separation shock wave. In Figure 2.1b it can be seen that the incident shock wave and the separation shock wave interact with each other, causing the shocks to refract. These refracted portions are called the reflected and transmitted shock (Sabnis & Babinsky, 2023). Then, because of the streamline curvature, expansion and compression waves are formed at the subsonic line and the reattachment point respectively. These compression waves coalesce into a reattachment shock wave. Finally, because the total pressure behind the reflected shock is different from the total pressure behind the transmitted shock, there is a slip line originating from the shock intersection point.

To further illustrate the impact of the viscous boundary layer, it is possible to look at the wall pressure distribution shown in Figure 2.2, taken from Délery and Dussauge (2009). This figure illustrates that already well upstream of the inviscid impingement location, there is a steep pressure rise because of the separation compression waves. The same occurs at the reattachment point, but here the pressure rise is usually less steep. The inviscid solution, however, only has a jump in pressure at the impingement location, before and after which the wall pressure does not change. Figure 2.2 shows that for the analysis of SWBLI it is not enough to make use of inviscid solutions with simple adjustments, but rather the viscous effects play a crucial role (Délery & Dussauge, 2009).

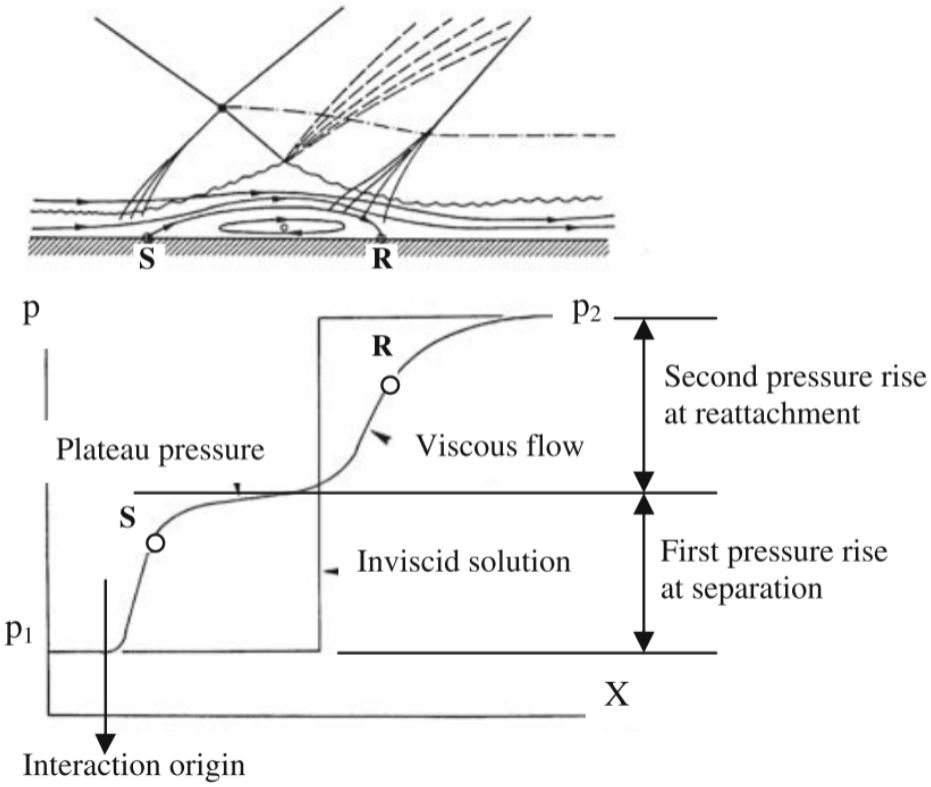

Figure 2.2: Wall pressure distribution, in a shock separated flow (Délery & Dussauge, 2009).

Three-Dimensional Structure

In reality, most of the SWBLIs are three-dimensional. For the current study, a closed wind tunnel with sidewalls is being used, and, therefore, it is relevant to study the effect of the presence of these sidewalls on the structure of the SWBLI. Bruce et al. (2011) found that when two-dimensional flow was considered for the onset of separation in normal SWBLIs, a reasonable agreement between different facilities was found. The same was not evident for three-dimensional flows. They found, however, that taking into account the tunnel confinement ratio led to the results following a clearer pattern. This study is also in agreement with earlier studies by Dupont et al. (2005) and Doerffer et al. (2010), suggesting that the separation at the centreline is linked to the corner flows at the walls of the wind tunnel. Figure 2.3 offers a schematic view of the wave pattern created by the presence of the sidewall as a consequence of corner separation.

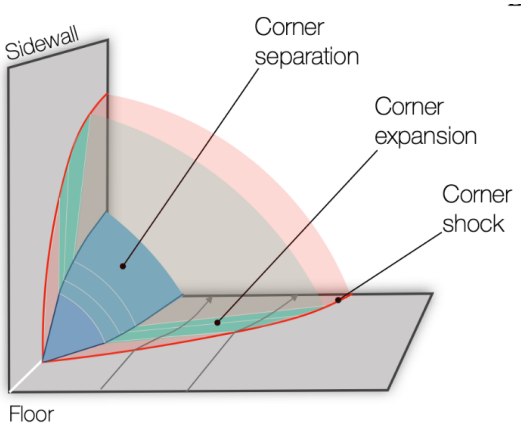

(a) Schematic of streamwise corner separation and resulting corner waves.

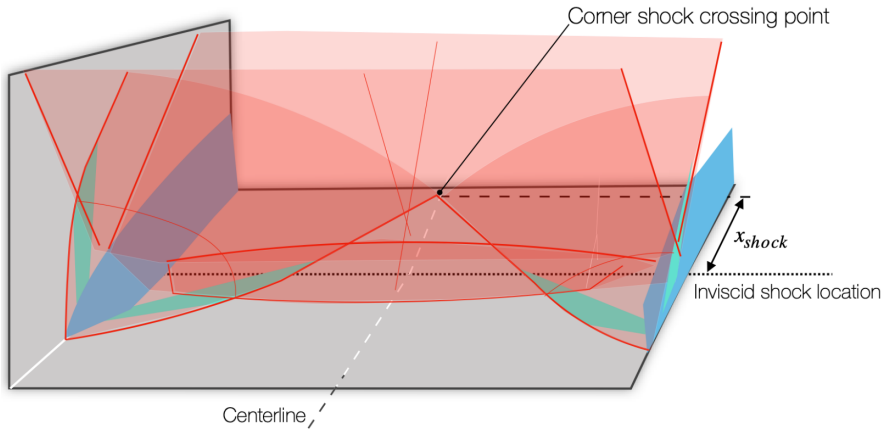

(b) Oblique shock reflection interaction in a rectangular duct

Figure 2.3: Schematic view of corner separation and the resulting shock and expansion waves and the interaction it has on an oblique shock reflection (adapted from Williams and Babinsky (2022)).

From Figure 2.3b it becomes evident that at some spanwise locations the corner shock and expansion fan interact with the shock structure on top of the separation bubble, while at other locations these waves might be located upstream or downstream of the main SWBLI structure. This confinement effect can be visualised with oil-flow visualisation, as done by Xiang and Babinsky (2019), which is shown in Figure 2.4.

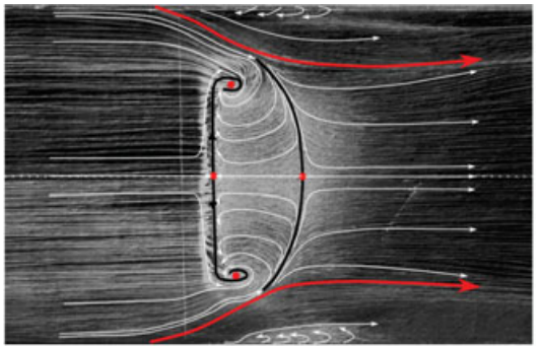

(a) Tunnel floor topology oil flow visualisation.

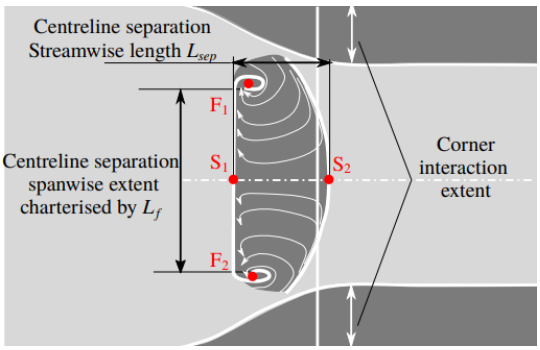

(b) Schematic illustration extracted from oil flow

Figure 2.4: Interpretation of flow topology on the tunnel floor for baseline flow by surface oil-flow visualisation; schematic illustration of separation sizes extracted from the oil flow. Limiting streamlines and the footprint of the separation are suggested for clarity; the vertical line indicates the inviscid shock location (adapated from Xiang and Babinsky (2019)).

Figure 2.4 shows that the separation bubble has a varying shape along the span of the wind tunnel, showing the three-dimensionality of the SWBLI structure. A Numerical study by Wang et al. (2015) shows that for a wind tunnel of aspect ratio equal to unity, the bubble length can increase up to a length 30 % larger than for a quasi-two-dimensional case, highlighting the importance of taking into account the walls confinement effect on the results. These numerical observations were already observed by experiments done by Babinsky et al. (2013) and later confirmed and expanded upon by Xiang and Babinsky (2019). Both experimental studies showed that for a large tunnel aspect ratio, the separation bubble length is approximately equal along the span, thus it can be considered a quasi-two-dimensional case. Then, for lower aspect ratios (assuming the same streamwise corner separation point), the corner shock and expansion fan will start interfering with the existing primary SWBLI structure; this increases the separation zone. For even lower aspect ratios, the corner waves will have a crossing point (for an example of this crossing point, see Figure 2.3b) ahead of the primary SWBLI, leading to a reduction in separation length. Recently developed "strip theory" by Williams and Babinsky (2022) predicts the separation length as a function of the streamwise location very well and confirms the experimental observations made by Xiang and Babinsky (2019). However, near the wall, this theory falls apart as there is a direct interaction between the corner and primary separations. The relevance of the results presented above for the current study is to know of the presence of these effects and to be able to identify the impact of these results at the centreline or other locations, depending on the type of measurements that are being done.

Finally, there is another three-dimensional effect, which is relevant to the experimental setup used in the current study (see section 3.2): the gap between the sidewall and the shock generator. This effect has been studied in detail by Grossman and Bruce (2019) and they found that an increase in sidewall gap leads to several changes to the SWBLI characteristics. The most relevant ones are that, first of all, a bigger sidewall gap decreases the height of the incident/reflected shock intersection. Also, the separation length decreases, while the separation width increases. Furthermore, with a larger gap, the separation and reattachment points shift downstream and the reattachment is accompanied by a decrease in static pressure rise. The evolution of the separation bubble as a function of the sidewall gap is shown below in Figure 2.5.

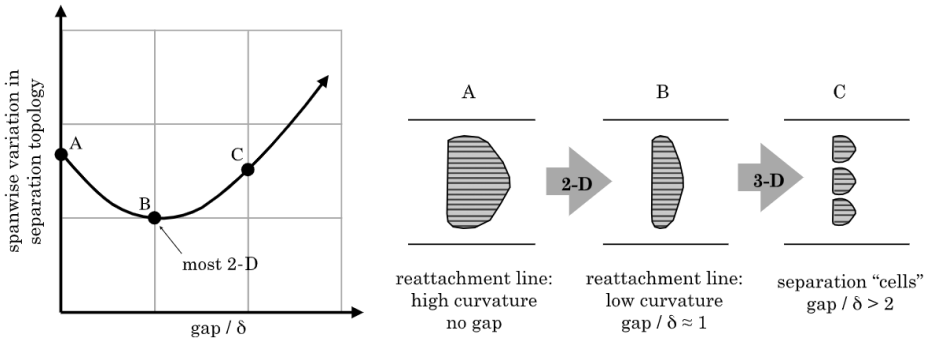

Figure 2.5: Evolution of separation bubble with sidewall gap (Grossman & Bruce, 2019).

2.1.2 Unsteadiness of SWBLIs

A characteristic of SWBLIs is their unsteady behaviour across a wide range of frequencies (Clemens & Narayanaswamy, 2014). In particular, the low-frequency unsteadiness has been a major point of discussion and opposing views. In his review at the start of the century, Dolling (2001) not only posed the question about the source of this low-frequency unsteadiness, but it was even still unclear whether these low frequencies were a general characteristic of SWBLIs or if they were generated by outside sources such as the wind tunnel. Furthermore, from a numerical perspective these low-frequency, large-scale

structures have been of interest because of the challenge involved in the modelling of them. Needless to say, with the years the tools used, both numerical and experimental, have been greatly developed to allow for more exploration and precise analysis, leading to some breakthroughs in the understanding of SWBLI low-frequency unsteadiness, which are discussed in this section.

Before diving into historical advances in the understanding of this low-frequency phenomenon, it is relevant to characterise the general unsteadiness of SWBLIs. In general, as supported by Figure 2.6 from the numerical research conducted recently by Laguarda et al. (2024), three regions with distinct dominant frequencies can be observed. First of all, upstream of the interaction region, there is a region of high-frequency fluctuations. Then, at the reflected shock and over the separation region, there is a region of low-frequency fluctuations, which is the main discussion point of this section. Finally, at reattachment, the fluctuations are of a high-frequency nature again, slowly becoming higher and higher with the flow recovering to freestream conditions. Note that the study by Laguarda et al. (2024) also studies flexible panels, which are of major relevance for the study of fluid-structure interaction (FSI) and shock-induced panel flutter; nonetheless the frequency content of all the cases presented follow the same trend.

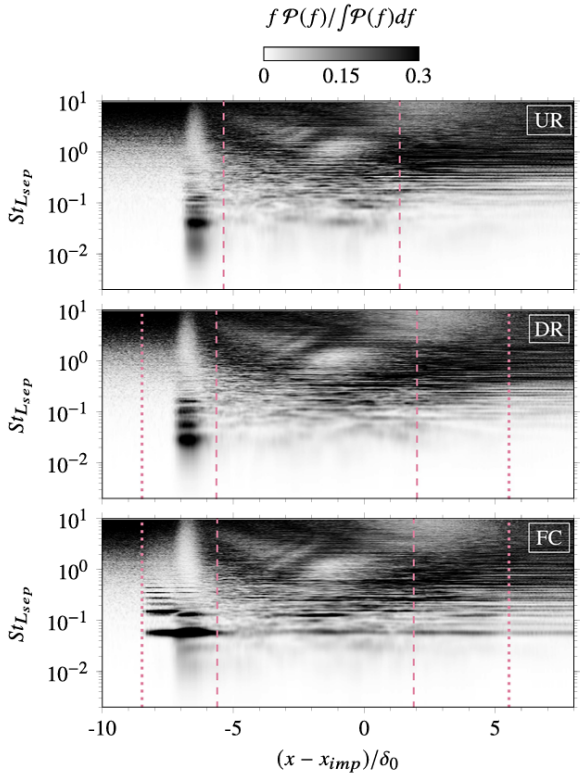

Figure 2.6: Pre-multiplied and normalizes PSD map of wall-pressure along the center-line of the investigated configurations. Dashed lines indicate the mean separation and reattachment locations, and dotted lines mark the leading and trailing edges of the flexible panel (Laguarda et al., 2024).

The separated region is very unstable and acts as an amplifier of the flow unsteadiness. This unsteady information is transmitted upstream through the bubble and starts a feedback loop, increasing the unsteadiness of the interaction (Babinsky & Harvey, 2011).

On the numerical front, a lot of progress has been made since the review by Dolling. The research by Morgan et al. (2013) has made the effort to address modelling errors associated with Reynolds-averaged Navier-Stokes (RANS) simulations, showing that inaccuracies arise due to the way the turbulence trans-

port term is modelled and the assumption of an isotropic dissipation rate. Pasha and Sinha (2012) proposed modifications to the models used for RANS simulations, which showed a better match with experimental results in particular cases. Overall, however, compared to large eddy simulations (LES) and direct numerical simulations (DNS), RANS is not deemed viable to explore the SWBLI behaviour. The effectiveness of these simulations has been showed by several studies such as by Pasquariello et al. (2015, 2017) (LES) and Priebe et al. (2009) (DNS). In addition to this, Poggie et al. (2015) compared data from flight tests, wind tunnel experiments and LES. Agreement across the compared data shows that this unsteadiness has common across a wide range of compressible flows and is not forced by outside sources/effects, such as wind tunnel and Reynolds number effects.

Historically, there has been a lot of debate about what the source is of this low-frequency unsteadiness. These views are summarised as follows (Ligrani et al., 2020):

- **Upstream Mechanism**: several experimental studies such as Humble et al. (2009) and Ganapathisubrama et al. (2007) detected regions of low- and high-speed flow with particle image velocimetry (PIV) measurements in the upstream flow. According to this upstream model, the reflected shock wave would move downstream whenever a large region of high-speed flow would approach the shock wave, while the opposite would be true whenever low-speed flow would approach. Other similar approaches, such as the one proposed by Beresh et al. (2002), look at the fullness of the boundary layer, and show that there is a strong correlation between the positive and negative velocity fluctuations with downstream and upstream motions of the reflected shock respectively.
- **Downstream Mechanism**: rather than looking at the incoming flow, the downstream mechanism focuses on the effect of the separation region behind the shock. In his study, Piponniau et al. (2009) proposed a method where mass would enter into the separation region, accumulate within the region, and, once big enough, the region would let a larger mass flow rate out. The experiments conducted suggest that this breathing of the separation bubble is correlated with the movement of the reflected shock wave: the reflected shock wave would move upstream with an increasing separation region, and vice versa for a shrinking separation region. LES conducted by Grilli et al. (2012) showed the same behaviour and coupling between the breathing motion of the separation bubble and the motion of the reflected shock wave.

Clemens and Narayanaswamy (2014) have made the effort to reconcile these opposite views, stating that ”both mechanisms are always present in all shock-induced turbulent separated flows but that the downstream mechanism dominates for strongly separated flows, and a combined mechanism dominates for weakly separated flows”. Similarly, Souverein et al. (2010) conclude that both mechanisms are always present, but depending on the specific case, one mechanism is more present than the other. Whenever no or little separation occurs, the upstream mechanism seems to be more dominant with high frequencies. When large separation occurs, it is the downstream mechanism, with the breathing motion of the separation region, that seems to be more dominant. Finally, for incipient cases, they conclude that both mechanisms can be equally present, depending on whether instantaneous flow separation is likely or not.

2.2 Shock-induced Panel Flutter

In engineering applications, weight saving is one of the challenges engineers have to deal with. As a consequence, thin plates are often used. Characteristic of these thin structures, when immersed in high-speed flow, is their coupled interaction with the air, known as *panel flutter*. When combined with the SWBLI phenomenon, as discussed in section 2.1, an even more complex but interesting phenomenon is obtained, which is called *shock-induced panel flutter*. The latter phenomenon is the main focus of this section. In addition to this, this section aims to lay a base for the study of the coupling between the flow and the panel, which is commonly called *fluid-structure interaction* (FSI). First, however, the case of common panel flutter, in the absence of an impinging shock wave, is shortly treated as a baseline for the case with the impinging shock (see subsection 2.2.1). After that, the effect of the impinging shock is treated in subsection 2.2.2. Then, some parameters, such as the panel boundary conditions (subsection 2.2.3) and the cavity pressure (subsection 2.2.4), and in particular their effect on the flutter, are discussed. Finally, the three-dimensional effects of panel flutter are treated in subsection 2.2.5.

2.2.1 Panel Flutter Without Impinging Shock

Panel flutter refers to the self-exciting vibrational motion of thin panels in supersonic flow, characterised by large amplitudes, potentially leading to fatigue damage (Vedeneev, 2012). The flutter of thin panels is similar to the flutter observed on airfoils and wings but differs in some important aspects (Dowell & Bendiksen, 2010):

- Stream-wise bending deformations are more dominant than span-wise bending deformations
- Nonlinear structural forces become more significant when plate deformations are on the order of the thickness of the plate
- Nonlinear aerodynamic effects due to the viscous boundary layer have a greater effect in high-speed flows

The boundary between the occurrence of a stable and unstable structural response of the panel is called the *flutter boundary*. This boundary is dependent on various aerodynamic and geometric parameters and needs to be carefully taken into account when designing an aerodynamic vehicle in supersonic flow. A commonly used parameter for determining the onset of flutter is the dynamic pressure, q. Often, however, when talking about flutter, a non-dimensional form of the dynamic pressure is used, defined as (Dowell, 1970):

$$\lambda = \frac{2qa^3}{D} = \frac{\rho_\infty U_\infty^2 a^3}{D}, \tag{2.1}$$

where a is the length of the panel and D is the flexural stiffness of the panel, defined as (Vedeneev, 2012):

$$D = \frac{Eh^3}{12(1-\nu^2)}, \tag{2.2}$$

where E is the Young's modulus, h is the thickness of the panel and ν is Poisson's ratio. By using this definition of the dynamic pressure for the flutter boundary, both aerodynamic and structural components are connected. Figure 2.7 shows the maximum panel deviation at different values of dynamic pressure.

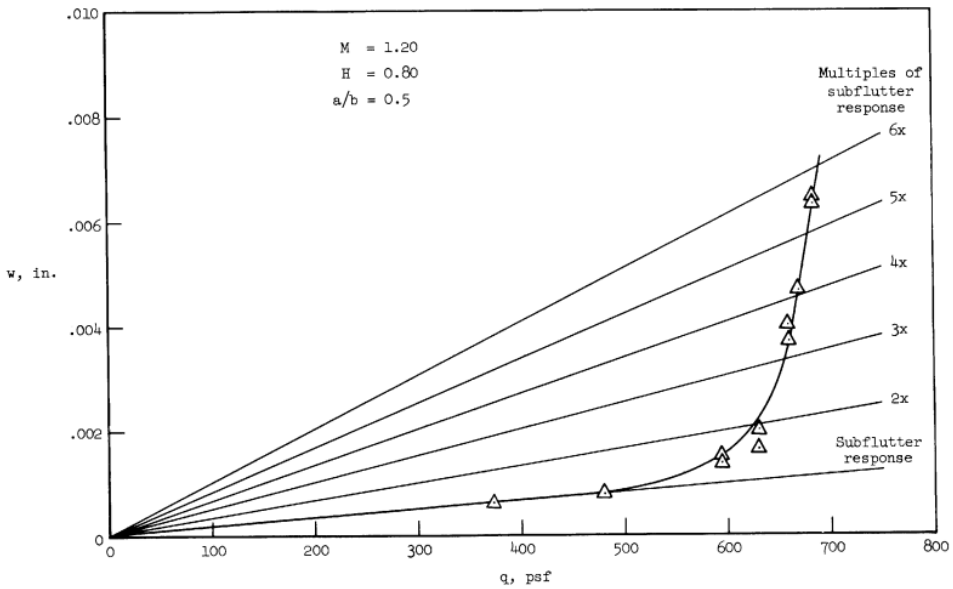

Figure 2.7: Typical variation of maximum panel response with dynamic pressure (Muhlstein et al., 1968).

These experimental results can be clustered into three different characteristics. For this, let's define a flutter dynamic pressure: q_f. For the experimental results shown in Figure 2.7, $q_f \approx 650$ psf. With this definition, it is now possible to distinguish the different stages of flutter:

- $q < q_f$: the panel response shows random oscillations, in the order of a fraction of the thickness of the plate, caused by fluctuations in the turbulent boundary layer. Moreover, the frequency of these oscillations is near the first natural frequency of the panel (Dowell, 1972).
- $q \to q_f$: the panel response becomes of the order of the panel thickness and a feedback loop with the flow kicks in; the motion of the panel and the fluctuations in the boundary layer influence each other. Oscillations become more periodic rather than being random (Dowell, 1972).
- $q > q_f$: the amplitude of the panel response increases, until a limit is reached. This limit is determined by structural and aerodynamic non-linear effects (Dowell & Bendiksen, 2010); the non-linear structural forces cause a stiffening of the panel (Dowell, 1974) and lead to limit cycle oscillation (LCO) (Dowell & Bendiksen, 2010). During LCO, the panel and the fluid exchange energy between one another, leading to a self-sustained oscillatory motion of constant amplitude and frequency.

As mentioned before, the nature of panel flutter is dependent on several parameters. However, for the current study, and in-depth analysis of the effect of all these parameters is out-of-scope. Rather, some of these parameters are discussed for the case where there is an impinging shock in the following sections.

2.2.2 Effect of Impinging Shock

With the inclusion of an impinging shock wave on a thin panel, not only simple panel flatter needs to be considered but also the effect the SWBLI has on flutter. This influence can be seen in the response of the panel in terms of flutter dynamic pressure, amplitude, frequency, mode shapes and pressure on the panel. Those changes with shock impingement are discussed in the rest of this section. A lot of research has also been conducted on the temperature effects. Those effects, however, are out-of-scope of the current study and, therefore, not included here.

Amplitude

Several studies, such as the one conducted by Willems et al. (2013), Visbal (2014) and Shinde et al. (2019), have shown that with the impingement of a shock, both asymmetric mean and dynamic dis-

placements are present. This asymmetry is attributed to the change in pressure distribution over the panel, as a consequence of the presence of shock and expansion waves. Figure 2.8 shows an example of such an asymmetrical distribution of static and dynamic deformations, which, as shown in Figure 2.9, "corresponds to the asymmetry in the wall pressure on panel in the upstream and downstream regions of the shock-impingement location" (Shinde et al., 2019).

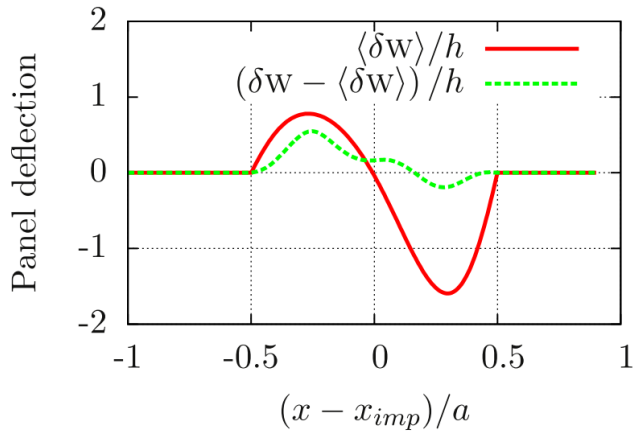

Figure 2.8: Panel deflection along the mid-span location (Shinde et al., 2019).

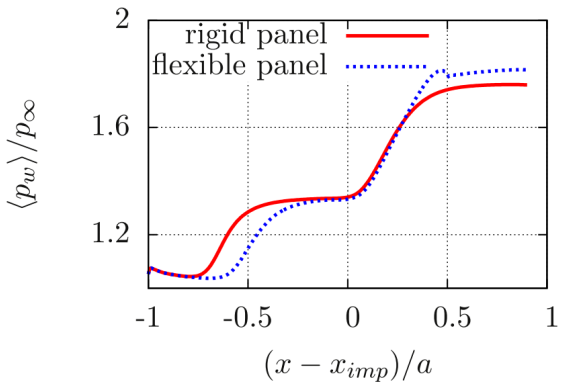

Figure 2.9: Time-averaged wall pressure profile at the mid-span location for the rigid and flexible panel cases (Shinde et al., 2019).

The static deformation shape in Figure 2.8 is also confirmed theoretically by Meng et al. (2020), using a similar shock impingement location, stating that the location of maximum vibration amplitude is located at the three-quarter point of the panel length. This location changes for different shock impingement locations (Willems et al., 2013) as a consequence of a different wall pressure distribution over the panel. Moreover, Beberniss et al. found, by comparison, that shock impingement leads to a larger displacement amplitude than without an impinging shock, as shown in Figure 2.10. An exception to this is for weaker shocks ($\frac{p_3}{p_1} \approx 1.2$), where Boyer et al. (2021) showed that the maximum amplitude decreases and the flutter dynamic pressure increases.

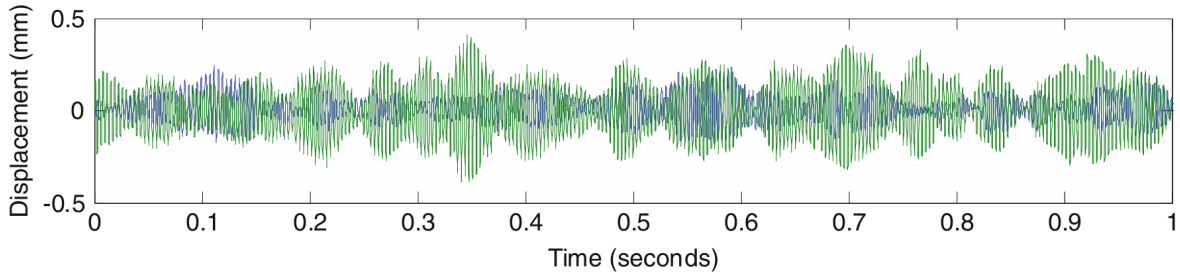

Figure 2.10: Panel centre displacement time history for shock (green) and no shock (blue) (Beberniss et al., 2016).

Frequency

With the presence of an impinging shock, Beberniss et al. (2011) found there to be a positive frequency shift in the dominant modes of the panel, as well as a widening of those peaks. Similar to what is explained in subsection 2.2.1, the impinging shock causes a stiffening effect on the panel, therefore shifting the response of the panel to higher frequencies. This is shown visually in Figure 2.11.

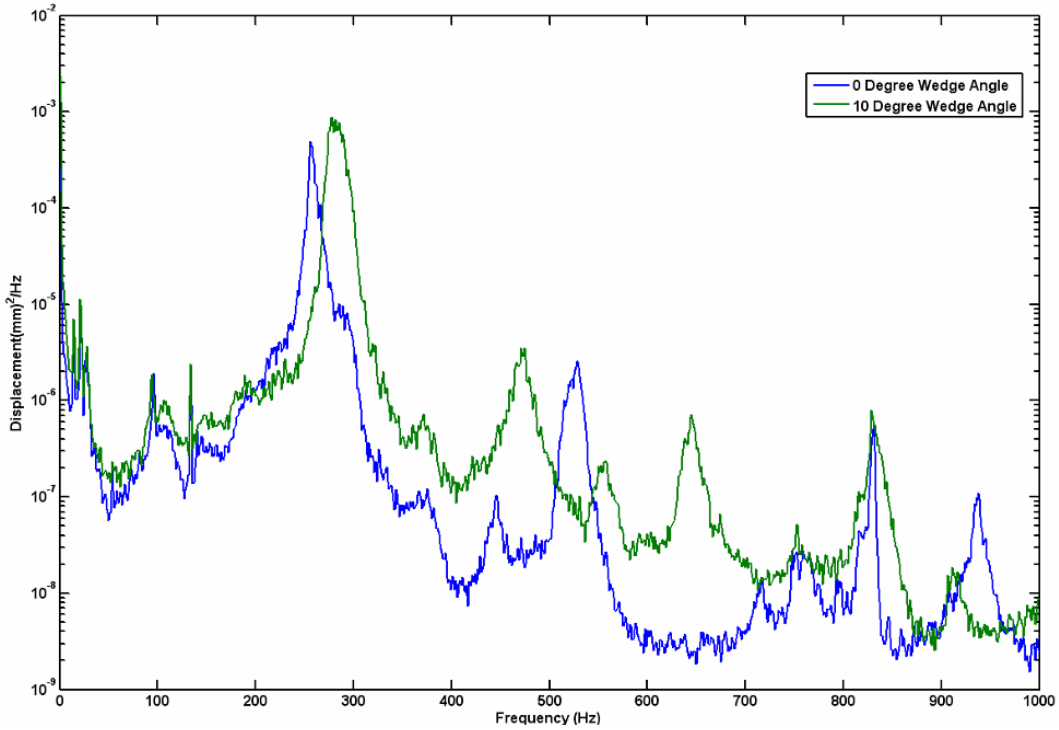

Figure 2.11: DIC displacement measurement PSD at panel centre with 0 degree (blue) shock wedge angle and 10 degree (green) wedge angle (Beberniss et al., 2016).

Furthermore, Visbal (2014) did a two-dimensional simulation where without a shock, a single dominant mode is present (see Figure 2.12a). The presence of an impinging shock changes this response to lower Strouhal numbers and a more chaotic behaviour with multiple dominant modes (see Figure 2.12b). Similar simulations for a semi-infinite panel in laminar flow, done by Boyer et al. (2021), have shown the exact peak frequency response for an incoming laminar boundary layer is very dependent on the dynamic pressure but that in general, compared to the case without an impinging shock, flutter frequency is increased for the case with an impinging shock.

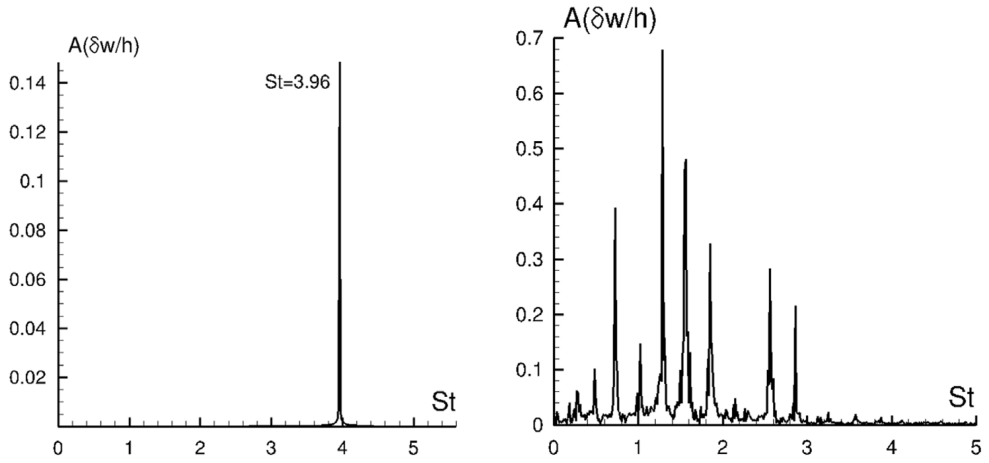

(a) No shock impingement. **(b)** With shock impingement

Figure 2.12: Frequency spectrum of panel response for laminar boundary layer interaction, without and with shock over flexible panel (Visbal, 2014).

Mode shapes

In their study, Spottswood et al. (2012) obtained three-dimensional digital image correlation (DIC) measurements, tracking the displacement of the used thin panel over a period of time. With the use of operational modal analysis (OMA), the modal modes and frequencies were identified, which are shown in Figure 2.13.

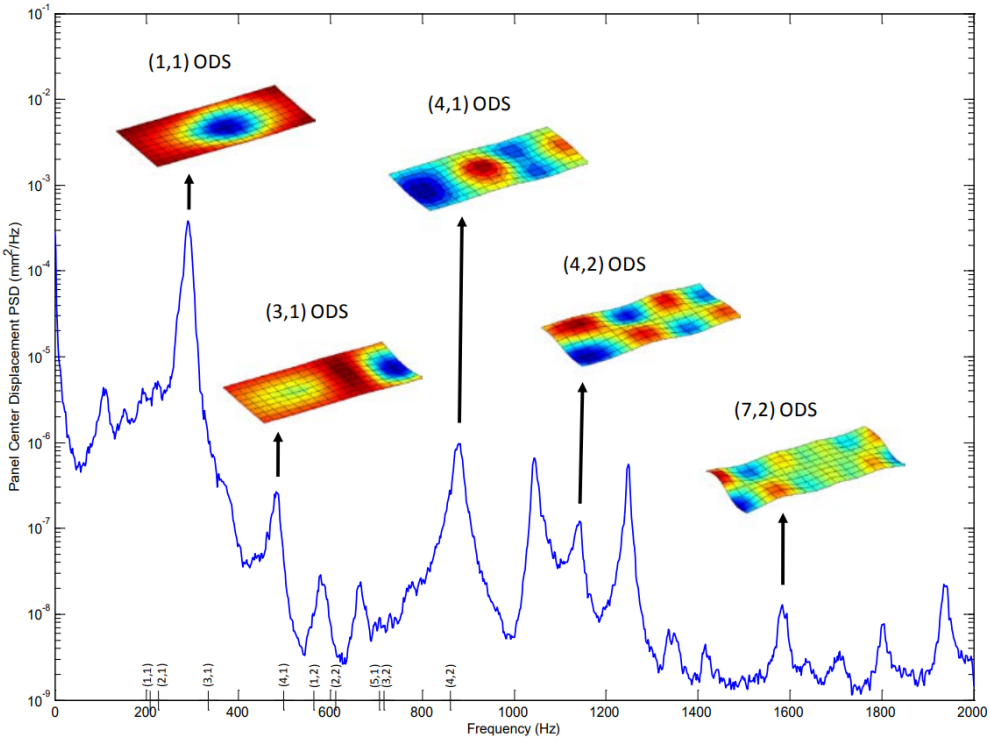

Figure 2.13: Panel centre displacement power spectral density and full-field displacement-based operational deflected shapes at $M_\infty = 2$ and $q_\infty = 123$ kPa (Spottswood et al., 2012).

Similar measurements on a fully clamped panel are done by Aditya (2022) but instead, a proper orthogonal decomposition (POD) was done on the DIC measurements to obtain the dominant modes. This study also makes a comparison with the case where there is no impinging shock and shows the amount of energy contained by each mode, as shown in Figure 2.14. A couple of observations can be made about these results. First of all, the dominant modes of oscillation drastically change with the presence of an impinging shock wave, which is no surprise considering the different nature of the flow interaction at the panel. Secondly, with an impinging shock wave, the dominant mode is similar to the one observed by Spottswood et al. (2012), namely a first bending mode. Moreover, this mode is also the most energetic one. In addition to this, especially the higher-order terms do not seem to be entirely symmetric around a streamwise plane at the middle of the plate, suggesting the presence of some kind of torsional mode. This is also true for the case without an impinging shock. Finally, the POD analysis reveals that it is mainly the first three to four modes that contribute to the most energetic content of oscillation; these energetic modes are also of a lower order, suggesting that higher frequency modes are less dominant in the fluid-structure interaction of a thin panel. A similar observation is made by Acosta and Austin (2024), where modal analysis showed that the lower-order modes ”represent over 98% of the energy in the panel response”, thus claiming that he panel response can be mainly made out by analysing a limited number of modes. Tripathi et al. (2024) did not compare the most dominant modes that the different cases exhibit, but rather looked at the first four bending motions ((1,1), (2,1), (3,1) and (4,1)) and looked at the difference with and without an impinging shock. For both Mach 2 and Mach 5, the frequency of the same mode would decrease in the case of an impinging shock compared to the case

without a shock. The magnitude of this shift was observed to be larger for the Mach 2 case. However, the amplitude of the vibrations increased for the case with a shock compared to the one without.

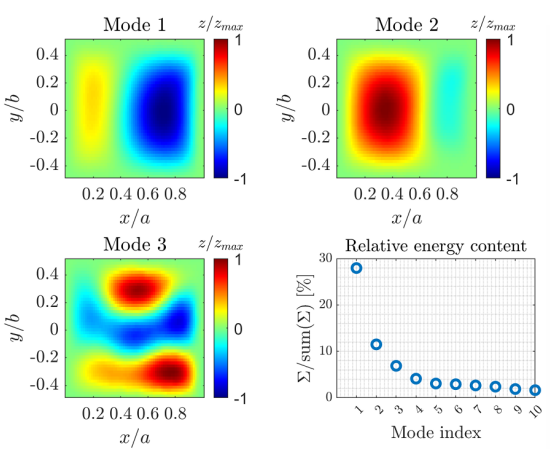

(a) No shock impingement.

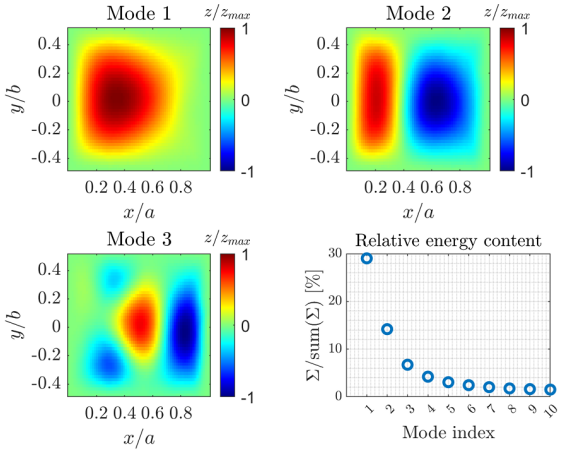

(b) With shock impingement and flow deflection of 12°

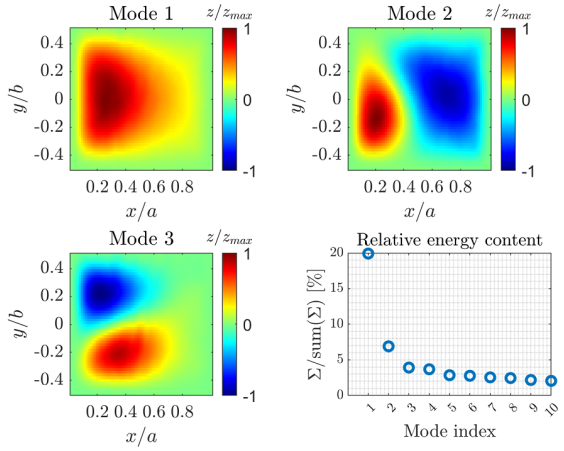

(c) With shock impingement and flow deflection of 15°

Figure 2.14: First three POD modes of a fully clamped, flexible panel with varying shock generator angles (Aditya, 2022).

A numerical study by Visbal (2014) also compared cases with and without shock impingement, but in a two-dimensional case. Instead of OMA or POD, the flutter behaviour on the x-t plane is analysed, which is shown in Figure 2.15. The clear difference that these diagrams show is that without an impinging shock, the panel exhibits a stable higher-order behaviour, while with an impinging shock, this behaviour becomes more chaotic, along with disturbances travelling back and forth along the panel. In the study, it was also shown that the lower-order terms make up the mean deformation of the panel, while the higher-order terms make up the dynamic deformations.

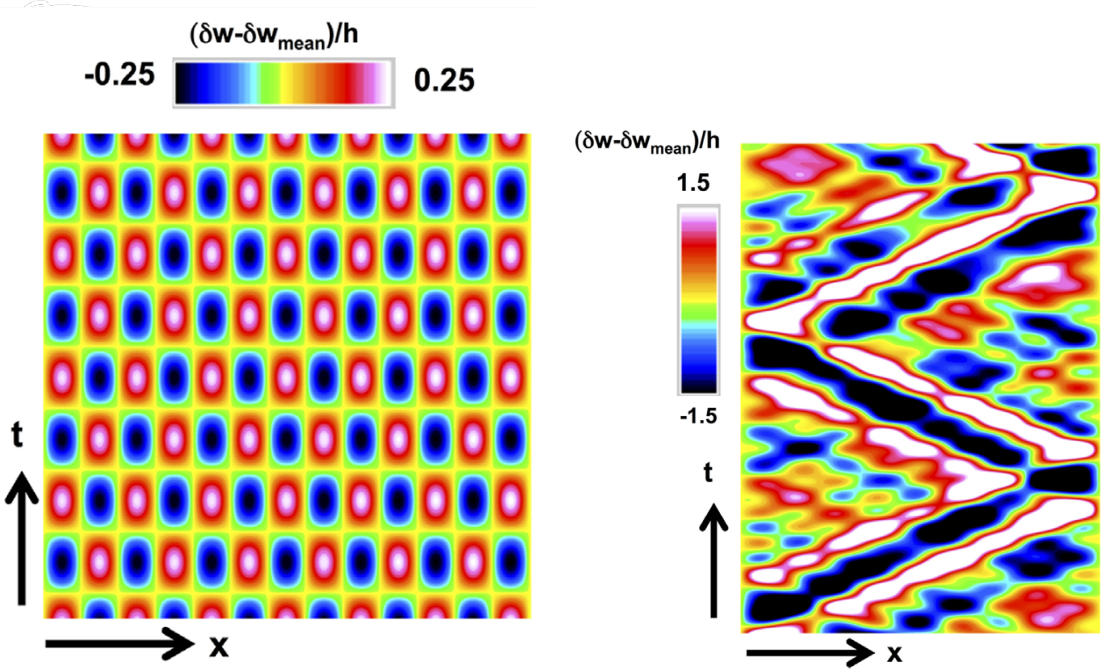

(a) No shock impingement.

(b) With shock impingement

Figure 2.15: X-t diagram of panel deflections for laminar boundary layer interaction, without and with impinging shock (Visbal, 2014).

Pressure

Already from the discussion in subsection 2.1.1 and as shown in Figure 2.2, it is clear that the impingement of a shock has a great influence on the wall-pressure distribution on the panel. Figure 2.16 shows both pressure maps obtained with pressure sensitive paint (PSP) and the PSD of the panel oscillations, obtained by (Spottswood et al., 2012) (2012). The pressure maps show the clear effect of the shock impingement: without a shock, the pressure remains constant, while with an impinging shock, clear pressure gradients can be distinguished, caused by the SWBLI structure. Furthermore, the figure shows that this difference in pressure distribution also causes shifts in the frequencies of the dominant modes. In their study, Shinde and Gaitonde (2022) use the wall-pressure information to show the presence of the ranges of turbulent scales and unsteadiness, for example, the low-frequency unsteadiness associated with the separated flow, which is consistent with the literature.

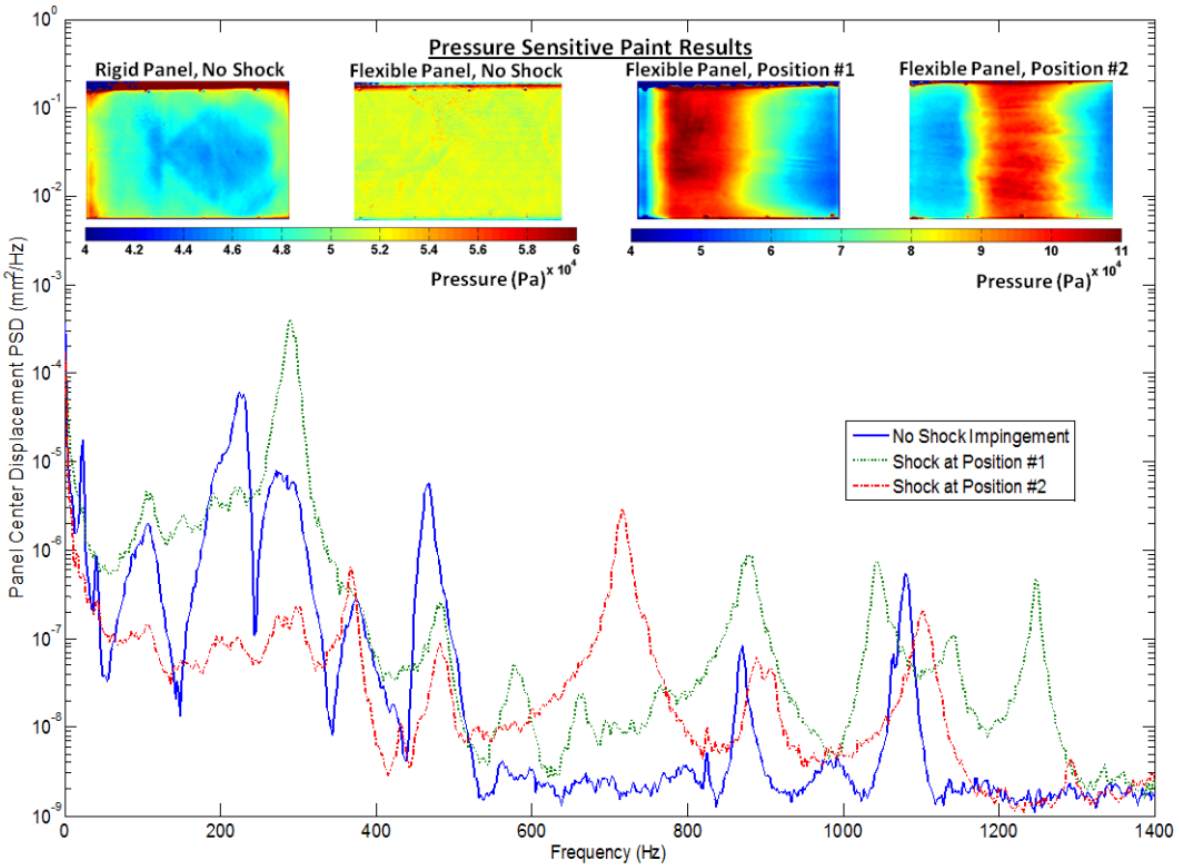

Figure 2.16: Panel centre displacement power spectra and corresponding full-field, time-averaged pressure maps for different shock impingement conditions at $M_\infty = 2$ and $q_\infty = 123$ kPa (Spottswood et al., 2012).

2.2.3 Effect of Panel Edge Boundary Conditions

One of the geometrical considerations to make is the clamping conditions of the panel. Most commonly found in literature are the fully clamped configurations (CCCC) and the configuration where two sides are unclamped (CCFF). While a lot is known about the effect of those clamping conditions with coalescent flutter, few studies have investigated the effect of this on shock-induced panel flutter. Allerhand (2020), however, did study the effect of varying boundary conditions in the same facility as the current study and, therefore, it is relevant to discuss some results here.

First of all, the surprising observation was made that the mean and dynamic deflection of the panel was more or less the same for both CCCC and CCFF. One would expect more rigidity from a fully clamped panel (Dowell & Bendiksen, 2010) but it is hypothesised that the increased mean deformation of the CCFF panel leads to additional stiffening that matches the deflected CCCC panel, and, as a consequence, to similar dynamic deflections (Allerhand, 2020).
Secondly, the CCCC panel exhibited a larger interaction length and separation area, but the experimental setup used did not allow for a conclusive answer on whether the two are connected or not.
Furthermore, a comparison in the frequency response of the reflected shock's motion shows a clear shift in dominant frequencies between the CCCC and CCFF panels. In particular, for the CCCC panel, it is shown that not only the dominant frequencies of the SWBLI are increased, but also that when close to the frequency of the Mach block's vibrations, the SWBLI frequency is locked to that frequency. The results obtained suggest that even though the resonance with the wind tunnel seems to drive the fluttering frequency, fluid-structure coupling is still present.
Finally, Allerhand (2020) looks at the modes of the panels and one of the most notable results is the

spanwise variation in the oscillations due to the clamping of the sides. However, it is concluded, after a spectral analysis, that these asymmetric spanwise variations only contribute in a minor way to the periodic motion of the panel. From these observations, it is clear that, for the fully clamped panel in particular, great care needs to be taken in the manufacturing and the condition of the panel, as manufacturing errors or exposure to (thermal) stresses might lead to torsional behaviour.

2.2.4 Effect of Cavity Pressure

Previously, the effect of SWBLI on the wall-pressure distribution has been discussed, which is the pressure on top of the panel. This section aims to present the effect of the pressure underneath the panel: the cavity pressure, p_c. In his numerical study, Visbal (2014) considered three cases: $\frac{p_c}{p_1} = 1.0, 1.2, 1.4$, where p_1 is the static pressure of the incoming freestream flow. The cavity pressure in these cases corresponds to the theoretical value upstream of the incident shock, the "zero net loading" pressure and the value downstream of the reflected shock respectively. For the net zero loading case ($\frac{p_c}{p_1} = 1.2$), LCO behaviour was observed. In the case of transverse loading ($\frac{p_c}{p_1} = 1.0, 1.4$), a steady buckled solution was observed, as well as the elimination of the LCO. Not only does this affect the mean shape of the panel, but also the mean wall-pressure distribution, as shown in Figure 2.17.

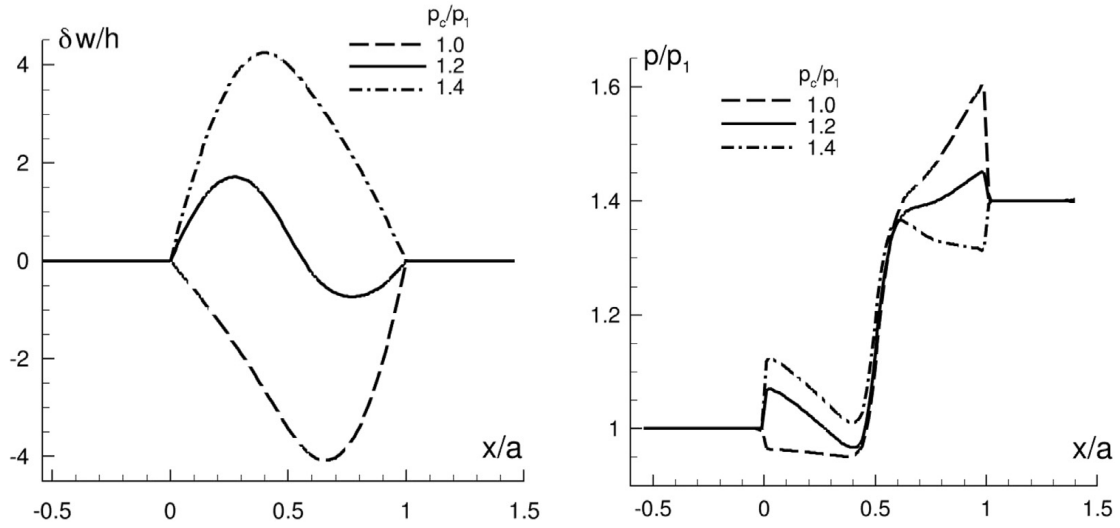

(a) Time-averaged panel deflection.

(b) Time-averaged surface pressure

Figure 2.17: Effect of cavity pressure for inviscid interaction with $M_\infty = 2.0$, $\frac{p_3}{p_1} = 1.4$ and $\lambda = 875$ on the mean panel deflection and surface pressure (Visbal, 2014).

Another numerical study by Zhou et al. (2023) shows that for $\frac{p_3}{p_1} = 1.4, 1.8$, the LCO frequency increases and the amplitude decreases, the latter being similar to the study by Visbal (2014). Furthermore, this study highlights that a change in cavity pressure affects the bifurcation characteristics of the panel response. Shahriar and Shoele (2024), however, observe an opposite behaviour in their numerical study regarding the shift in frequency, namely that the frequency of the panel response is lowered with increasing cavity pressure. This however can be attributed to differences in the numerical models and (boundary) conditions and shows the importance of the documentation of the conditions. This is highlighted by the experiments by Brouwer et al. (2021a) and Brouwer et al. (2021b) where an attempt was made to study the hysteresis effects on shock-induced panel flutter by varying the cavity pressure. Because of a changing independent temperature differential between the panel and the wind tunnel blocks, it is not clear whether the differences observed across the experiments are due to the hysteresis effects caused by the variation in cavity pressure, or because of this changing temperature differential.

Another experimental study by Gramola et al. (2020) also looks at the panel deflection and the effect on

the pressure distribution at the wall. These results are shown in Figure 2.18. What can be seen is that when the cavity pressure is low, the mean shape of the panel is more downward, while when the cavity pressure is higher, the opposite is true. This is to be expected as when the pressure on top is higher than below, the plate deflects downwards and vice versa. For intermediate cavity pressure, a sinusoidal shape is obtained. Moreover, the shape at the leading edge has a great effect on the pressure distribution, as, dependent on the curvature of the leading edge, shock or expansion waves might be created, and thus, the pressure might increase or decrease respectively (see Figure 2.18b). Experiments by Tripathi et al. (2021) show similar behaviour as found by Gramola et al. (2020), with an additional observation that the interaction length of the SWBLI is also a function of the cavity pressure.

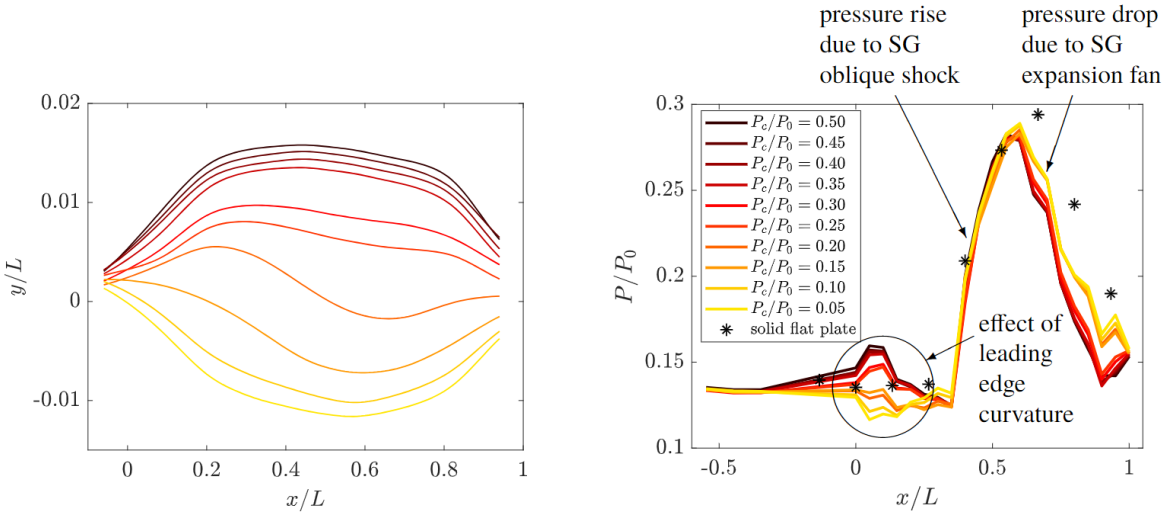

(a) Centerline plate displacement.

(b) Centerline pressure distribution.

Figure 2.18: Centerline plate displacement and corresponding pressure distribution for a $M = 2$ oblique shock with $x_s/L = 0.4$ and cavity pressures between $p_c/p_0 = 0.05 - 0.5$. The baseline pressure profile for a solid flat plate is added for comparison. The same legend applies to both plots (Gramola et al., 2020).

2.2.5 Three-Dimensional Effects of Panel Flutter

As a continuation of the three-dimensional effects in SWBLI (see subsection 2.1.1), this section aims to address the three-dimensional in the presence of shock-induced panel flutter. In a numerical study, Boyer et al. (2018) found that the qualitative behaviour of the three-dimensional configuration is similar to the two-dimensional one. However, quantitatively, the flutter dynamic pressure increases, the flutter amplitude slightly decreases and significant spanwise variations occur. The latter was also observed by Shinde et al. 2018, 2019, where transitional SWBLIs using DNS were conducted. They also found that for transitional SWBLIs, the assumption of cylindrical bending (i.e. the derivatives in the spanwise direction are zero) is not valid for three-dimensional, viscous shock interactions.

Many factors can play a role in experimental studies, as discussed in previous sections. Flow interaction with the side-walls and the gap between the shock generator (if not large enough) and the side-wall are sources of shock wave bending, introducing a three-dimensional effect, as observed for example by Willems et al. (2013). As discussed in subsection 2.2.3, the clamping condition of the panel could also introduce span-wise disturbances or components because of the bending modes of the panel or torsional moments that are introduced. The difference produced in the pressure distribution can also be seen in Figure 2.16, where the pressure varies in the spanwise direction. Tripathi et al. (2021) shows, using oil flow visualisation on a thin panel, that a change in cavity pressure can also contribute to the three-dimensionality of the flow, as shown in Figure 2.19.

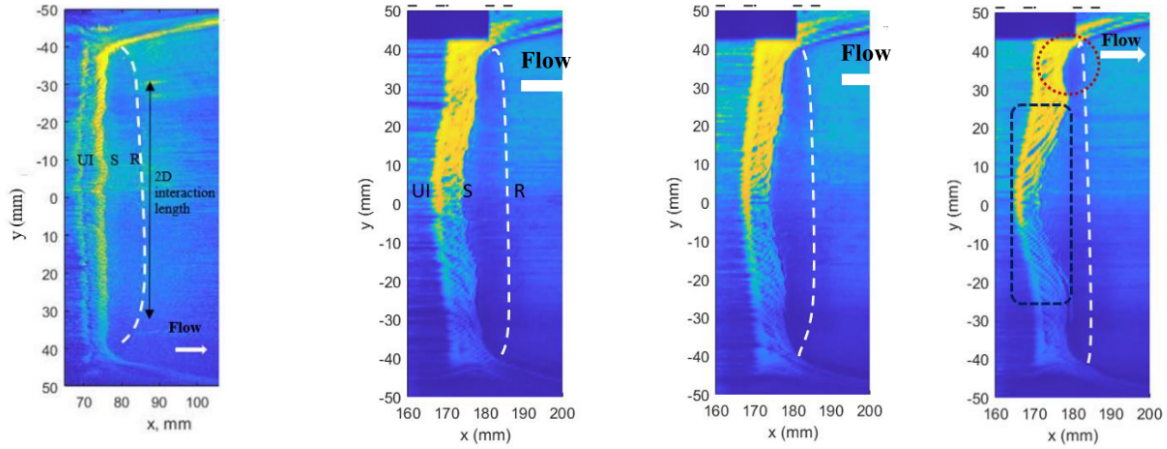

Figure 2.19: Surface oil flow visualisation for $3/4^{th}$ shock impingement location. A rigid plate is shown on the left and the rest is a thin panel, with decreasing cavity pressure from left to right (Tripathi et al., 2021).

2.3 Latest Research at TU Delft

The current study is a continuation of recent studies conducted at the Delft University of Technology, as a part of a MSc thesis at this university. This section aims to present the results of recent studies concisely as a foundation and justification of the formulated research questions. This includes work from past MSc theses of Allerhand (2020), Aditya (2022) and Mathijssen (2022). Other considerations from these studies such as measurement techniques, setup and analysis methods will be discussed in their respective part of this thesis, when relevant. In addition to this, conclusions from a recently published paper by Laguarda et al. (2024) are briefly presented as well.

2.3.1 Experimental Investigations in ST-15 wind tunnel

Before the current study, some other experimental studies have been conducted concerning (shock-induced) panel flutter in the ST-15 supersonic wind tunnel facility at TU Delft. Mathijssen (2022) analysed panel flutter on thin panels, while Allerhand (2020) and Aditya (2022) did it with the presence of an impinging shock. Several optical measurement techniques have been used, such as schlieren, DIC, laser Doppler vibrometry and PIV.

Allerhand (2020) made a successful effort to conduct simultaneous PIV and DIC measurements. As one might expect, there is some optical distortion because of the SWBLI shock structure. However, it is suggested that this has a negligible effect on the DIC displacement measurements. Due to the oscillation of the panel, the laser reflections become unsteady and cause a loss in accuracy close to the panel. The coupling between the panel and the flow was shown in several ways. First of all, the frequency of the reflected shock oscillations seems to match the energy peaks in the motion of the panel. Furthermore, phase averaging and cross-correlation of the vertical flow velocity signal and the panel's displacement signal at the mid-span location show strong correlation coefficients, where this is stronger in some regions than others. A similar exercise has been done by Mathijssen (2022), where simultaneous DIC and schlieren experiments were done. These two studies both showed that (shock-induced) panel flutter is a repeatable and periodic phenomenon, which is the reason why Aditya (2022) chose to do DIC and schlieren measurements separately, to reduce possible interference effects of simultaneous experiments and make the setup of the measurement equipment in tight spaces easier.

Something that was observed in all three studies, was the presence of wind tunnel vibrations, causing the panel to resonate at the same frequencies of those vibrations. The fact that this was also the case for Mathijssen (2022), suggests that this is a phenomenon inherent to the ST-15 wind tunnel and not to

FSI phenomena as studied by Allerhand (2020) and Aditya (2022). Aditya (2022) tried to investigate the source of these vibrations and hypothesised different sources, such as thermal effects because of the cooling down of the wind tunnel and the fact that the cavity underneath the test section was not closed and, thus, connected to the test section flow. The presence of these vibrations and the lock-in resonance effect, as hypothesised by Mathijssen (2022), makes it hard to make conclusive statements about the fundamentals of FSI in the presence of an impinging shock.

2.3.2 Numerical Investigation Into Mean Panel Deformation Effects

Laguarda et al. (2024) conducted a numerical simulation, using similar parameters and conditions as used by Allerhand (2020) and Aditya (2022), to investigate the FSI in the presence of an impinging shock wave on a rigid, thin and rigid deformed panel. One of the main focuses of the study has been to identify the effect of static and dynamic panel deformations. This is done by making a deformed, rigid panel which has the shape of the mean deformation of the thin panel. This way the effect of the static deformation is isolated from the dynamic deformations. Analysis of the flow field and the spectral content of the flow show that the separation characteristics are mainly established through the mean deformation of the panel. The dynamic behaviour of the panel can, however, accentuate SWBLI and FSI features that may or may not be desirable. The author has therefore expressed interest in an experimental comparison to validate the findings from this research.

3

Experimental Setup & Measurement Techniques

In the pursuit of answering the research questions posed in chapter 1, it is necessary to dive into the methods used to achieve the goals of this study. As this is an experimental study, this involves the use of a (supersonic) wind tunnel and several measurement techniques that each have their distinct purpose and contribution to answering the research questions.

The aim of this chapter is to present the various aspects that have been part of conducting the experiments in the ST-15 wind tunnel environment, which starts with a brief introduction of the wind tunnel facility itself in section 3.1, followed by an explanation of the test section setup in section 3.2. After that, section 3.3 discusses the design of the used panels; in particular it aims to explain how the rigid deformed panel was manufactured to be placed in the wind tunnel. section 3.4 to section 3.8 introduce all the experimental techniques used in this study. In section 3.4, it is discussed how the cavity pressure is measured. After that. section 3.5 introduces some techniques that reveal the flow field organisation in a qualitative way. Furthermore, section 3.6 explains which techniques are used for temperature measurements, to analyse its affects on the interaction. DIC and PIV measurements, presented in section 3.7 and section 3.8 respectively, show how the separate motion of structure and flow is investigated. Finally, an uncertainty analysis is performed for the DIC and PIV experiments in section 3.9.

3.1 Supersonic Wind Tunnel Facility

The experiments conducted for the current study are all conducted in the ST-15 wind tunnel of the High-Speed Laboratory (HSL) at the Delft University of Technology (see Figure 3.1). This wind tunnel is a blowdown tunnel, which is connected to a pressure vessel supplying dry air. This pressure vessel has a volume of $300\,\mathrm{m}^2$ and can store the air up to 40 bar using a $6\,\mathrm{MW}$ compressor. A schematic of the ST-15 is shown in Figure 3.2, showing the convergent-divergent nozzle design of the tunnel needed to achieve supersonic conditions in the test section. Contrary to many modern supersonic tunnels, the ST-15 does not have a flexible-wall nozzle, to set the Mach number. Rather, specific Mach blocks can be installed in the upper and lower sides of the wind tunnel to achieve Mach numbers of either 1.5, 2, 2.5 or 3. For the current study, Mach blocks are installed such that a Mach number of 2 is reached in the test section. The test section itself is a $15\,\mathrm{cm} \times 15\,\mathrm{cm}$ rectangular test section, equipped at both sides with $25\,\mathrm{cm}$ windows. More details about the test section setup are given in section 3.2. The conditions as measured in the settling chamber are considered to be the total conditions of the flow. While the temperature cannot be set, the total pressure in the settling chamber can be set from $p_0 = 2.0\,\mathrm{bar}$ to $p_0 = 4.8\,\mathrm{bar}$ for Mach 2. To achieve similar flow conditions as Allerhand (2020) and Aditya (2022), the total pressure in the settling chamber is set to $p_0 = 2.5\,\mathrm{bar}$. Behind the test section, a convergent-divergent diffuser is present which slows the flow down to subsonic conditions while minimising pressure losses. The wind tunnel design assures that the pressure at the entrance of the diffuser is much lower than the atmospheric pressure, at which the diffuser discharges air. This is needed so that the pressure in the vessel can be lowered to achieve the pressure ratio required to operate the wind tunnel.

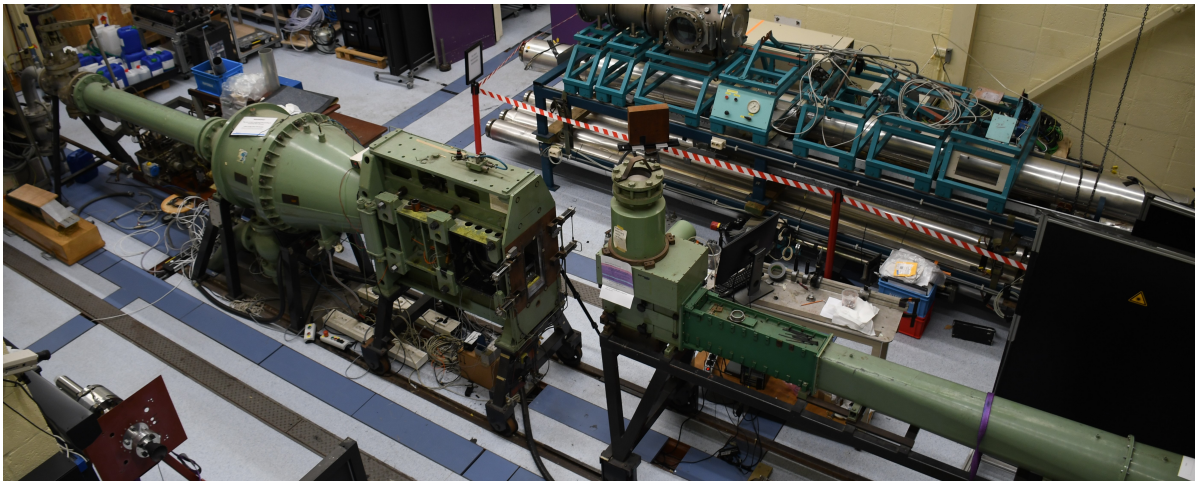

Figure 3.1: Photograph of the ST-15 wind tunnel taken from an upper angle. Air flows from left to right.

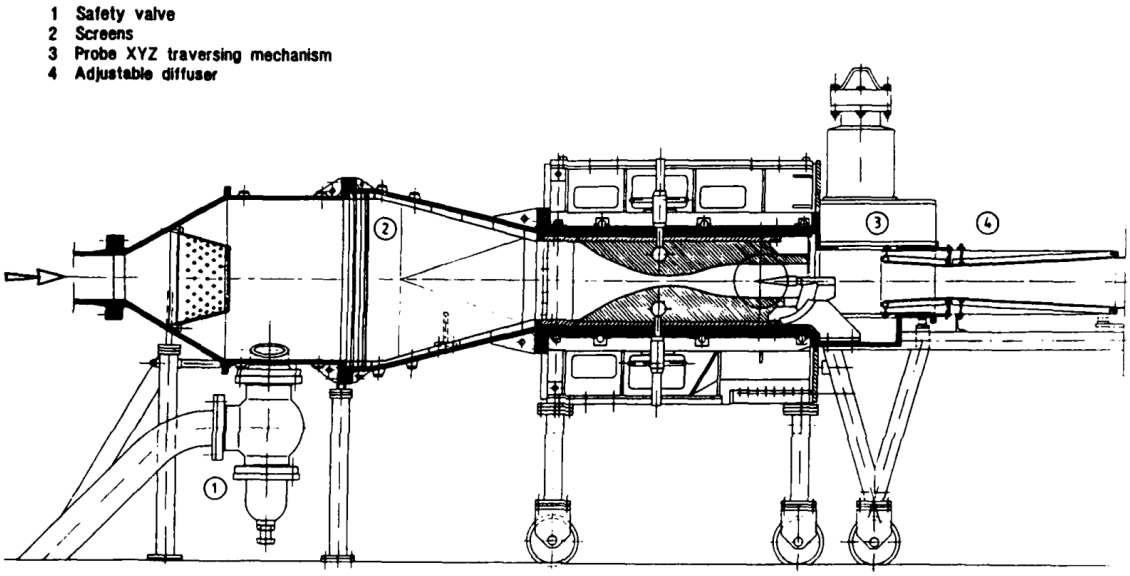

Figure 3.2: Schematic of the ST-15 wind tunnel (Kingsbury, 1990).

3.2 Test Section Setup

The test section can be found at the end of the convergent-divergent nozzle where, with the used Mach blocks, the free-stream Mach number is 2. The 15 cm $\times$ 15 cm rectangular test section has two 25 cm windows that allow for optical access. For the current study, three components are used in the test, all shown in Figure 3.3: the panel model, the clamping pieces and the shock generator. The panel model is the object of interest, to be studied. This is either a solid panel, a thin panel or a 3D-printed panel. More information about the panel model is presented in section 3.3. To ensure that the panel does not move, clamping pieces are used, which are bolted to the lower Mach block with two M4 hexagonal bolts each. Finally, above the model, attached to the upper Mach block, a shock generator is present, which creates the impinging shock wave onto the panel. The angle of the shock generator determines the shock strength: the larger the angle, the shock the shock.

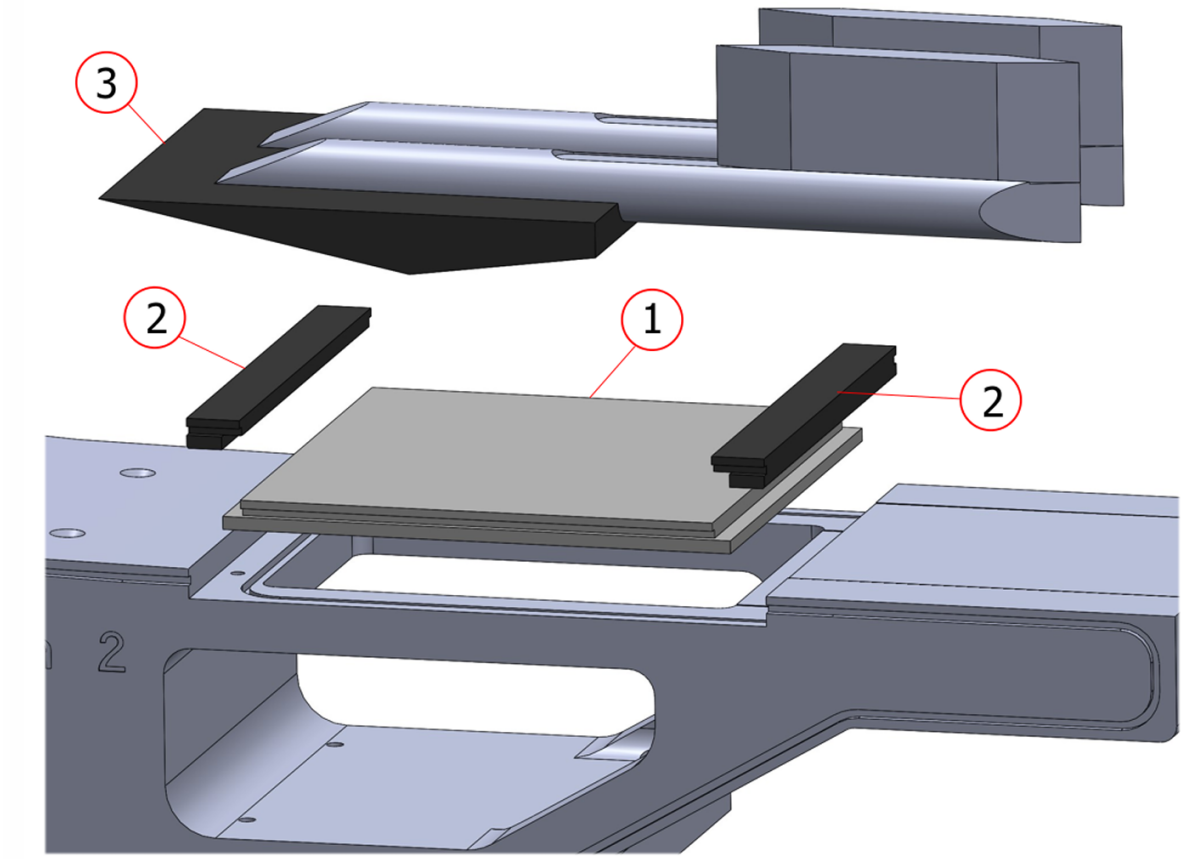

Figure 3.3: CAD model of the wind tunnel test section setup showing: 1) panel model 2) clamping pieces 3) shock generator (Allerhand, 2020).

Table 3.1 shows the flow conditions as used in this study. Those are chosen to have similar conditions to previous studies on shock-induced panel flutter in the ST-15 (Aditya, 2022; Allerhand, 2020). In particular, the shock impingement location, normalised with the thin panel length a, is kept similar as it has been shown that this has a great effect on the static deformation of the panel. The reported boundary layer thickness at the start of the test section, $\delta_{99,0}$, was measured by Giepman et al. (2018) in the ST-15.

Table 3.1: Flow and shock properties in test section.

Parameter	Value
M_∞	2
p_0	2.5 bar
q_∞	0.89 bar
$\delta_{99,0}$ (Giepman et al., 2018)	5.2 mm
Re_∞/L	3.33×10^7 m^{-1}
θ_{SG}	12°
x_{imp}/a	0.55

Another inspection of Figure 3.3 reveals that underneath the test section, a chamber, called the cavity, is present, which allows for the placement of measurement equipment underneath the test section. In previous studies in the ST-15, this cavity was not fully closed: flow downstream of the test section was able to flow down and back into the cavity. This is shown schematically in Figure 3.4.

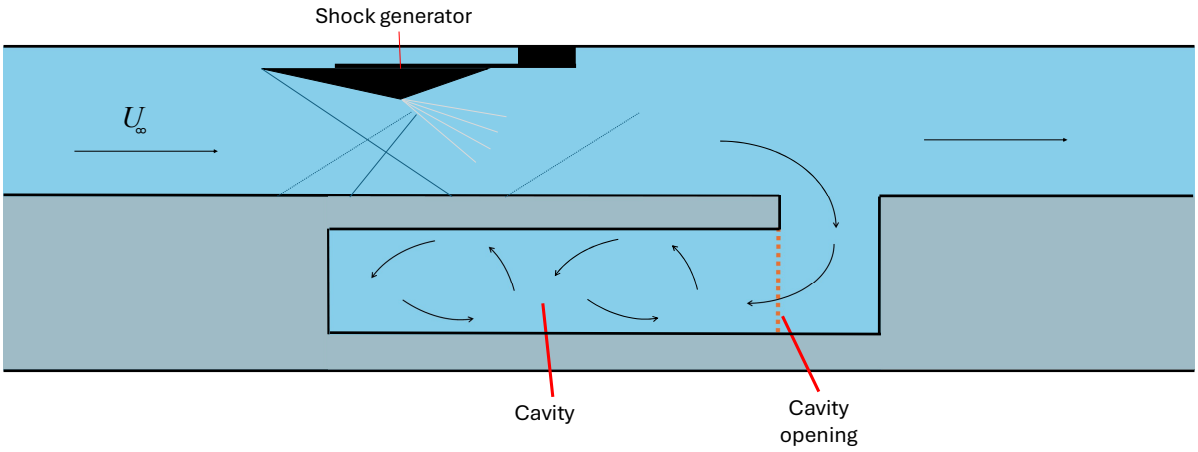

Figure 3.4: Schematic showing the test section with shock generator and the location of the cavity opening in the ST-15 wind tunnel environment.

By these previous studies, it was hypothesised that this flow coming inside the cavity forces the panel into resonance motion (Aditya, 2022; Allerhand, 2020; Mathijssen, 2022). As a solution, suggestions were made to close off the cavity. Hence, the closure of the cavity is one of conditions to be considered in the current study. To achieve this, an aluminium plate is manufactured such that it closes off the cavity from the flow coming from the test section. Nine holes are drilled into this plate and closed off with bolts; this allows for choosing to remove some of these bolts and equalising pressure between the cavity and the region downstream of the test section, without large pressure waves entering the cavity. The three conditions considered are shown in Figure 3.5: the open-cavity case, a ventilated cavity where nine holes are left open, and a completely closed-off cavity.

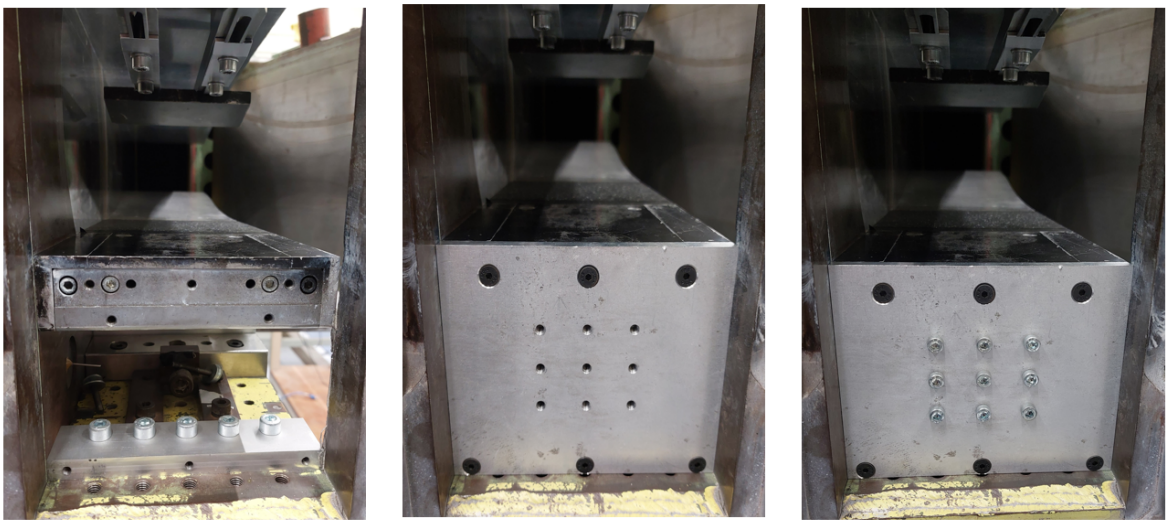

Figure 3.5: Cavity closure conditions inside the ST-15 wind tunnel facility. The three cases considered are the open cavity (left), a ventilated cavity with nine holes open (centre), and a completely closed cavity (right).

Figure 3.6 illustrates how much of the test section is visible from an outside perspective. From a central location, it is possible to view the entirety of the panel, as well as parts of the Mach block surface both up- and downstream of the panel. However, once cameras are put at an angle with respect to the window (e.g when using a stereo configuration with two cameras) the edges of the window start covering parts of the panel. Thus, a good positioning of the cameras is needed to ensure that no information is lost.

From Figure 3.6 it is also visible that there is very little optical access into the cavity. That is why optical measurement techniques are deemed impractical for measuring the flow inside the cavity.

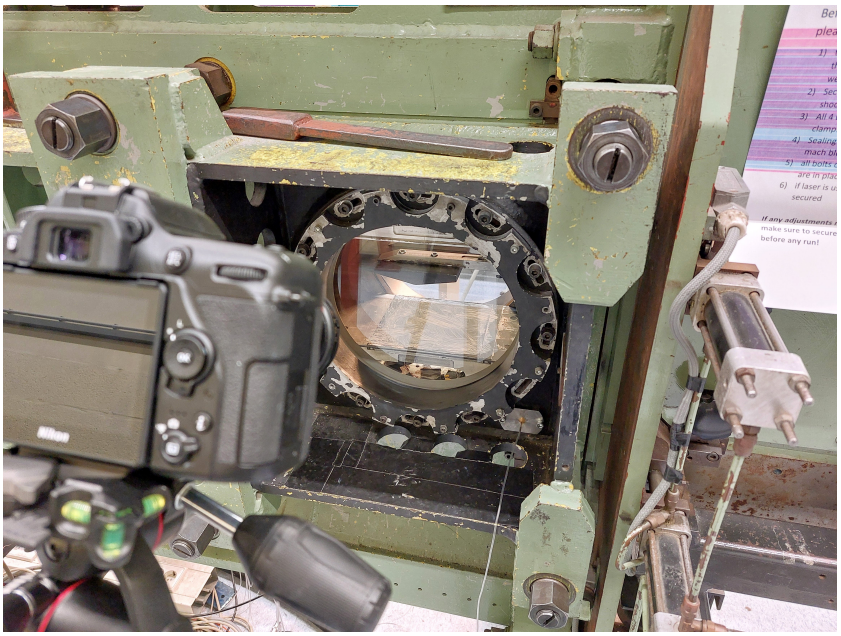

Figure 3.6: Visibility of test section through window from outside the tunnel as seen during an oil-flow visualisation experiment.

3.3 Panel Model Design

The model to test in this study is a flat plate, clamped between two clamping pieces, as shown in Figure 3.3 in the previous section. More specifically, the centre part of the plate is made very thin, down to a thickness of 0.3 mm. Moreover, the aspect ratio of this rectangular thin portion of the plate is 1.5. It is chosen to use a fully clamped (CCCC) panel for two reasons:

1. In order to perform reliable pressure measurements inside the cavity, no air must escape or enter through any free edge of the panel. A fully clamped panel ensures that no air flow goes directly from test section to cavity or viceversa.
2. Data for a CCCC panel with aspect ratio 1.5 is already available to compare to from previous experiments conducted by Aditya (2022), making it possible to compare results.

The fully clamped configuration of the panel leads to the study of a three-dimensional behaviour of the panel movement, compared to the 2-dimensional one of a panel with two free edges. The dimensions of the panel can be found in the technical drawing presented in Appendix B. Additionally, a rigid panel is used as a reference case without any fluid-structure interaction.

As the thickness of the panels is extremely thin, the manufacturing process is not trivial. After milling the outside shape of the panel and removing most of the inside of the panel forming the thin portion, the upper side of the panel is put on a vacuum suction plate. This ensures that the upper side of the panel does not move while the machine mills the last part of the panel, down to 0.3 mm. Some stress is introduced into the thin part, making the panel slightly buckle. However, the plate is manufactured such that when clamped into the wind tunnel at its sides, this stress is relieved as much as possible, eliminating most of, if not all of the buckling. On top of this, the actual forces on the panel are much greater than this, thus keeping the influence the little buckling has on the deformations to a minimum.

The current study investigates the effect of the mean deformation of the plate on the fluid-structure interaction. To achieve this, cases are analysed where a thin panel has a mean deformed shape, together with dynamic oscillations around that mean. In addition to this, a case is analysed where the mean deformation of the thin panel is used and restricted to move, as if it was a rigid deformed plate. The current study accomplishes this by 3D-printing the shape with the measured mean deformation. For more information on the technique used to obtain the plate deformation, refer to section 3.7. As it is not possible to clamp such a 3D-printed block directly into the ST-15 wind tunnel, a holder needed to designed to fit inside the tunnel and restrict the movement of the printed block. Furthermore, it is desirable to swap out different blocks with different shapes, without damaging either the block or the holder themselves. That is why the holder has 8 evenly distributed holes at the bottom, matching those in the 3D-printed block, allowing bolts to be used to secure or release the block from the holder. A technical drawing of the final holder product is presented in Appendix B. Figure 3.7 shows the fit of the holder and the deformed block into the wind tunnel.

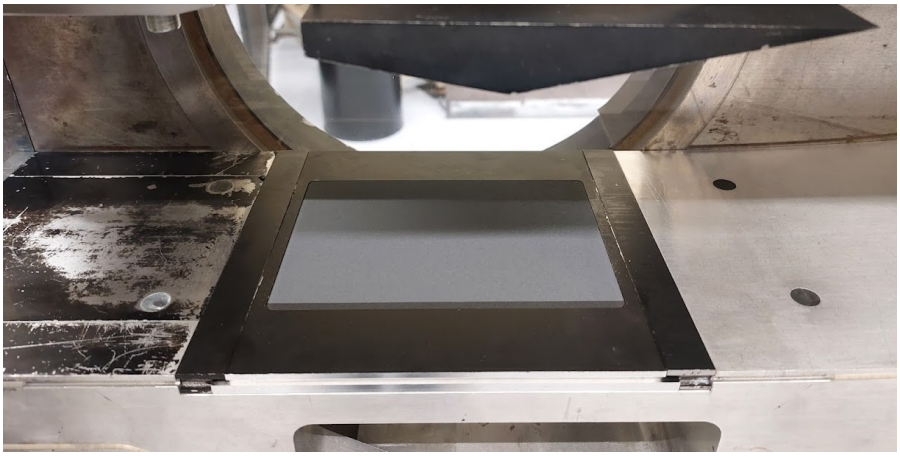

Figure 3.7: Fit of the rigid deformed panel inside holder and ST-15 wind tunnel.

Taking a step back, the making of the 3D print itself is also not entirely trivial. This paragraph aims to describe the process step-by-step on a high-level. The first step, after performing and processing the structural field measurements, was to export the out-of-plane vector field and open it in MATLAB. In MATLAB, the mean of the deformations was computed, after which the mean of the rigid panel case was subtracted. As the rigid panel is not supposed to deform, any deformations that are detected can be considered as an error in the measurement system and can therefore be used as a correction. The computed cloud of points, representing the mean deformation of the panel, were then exported to a CAD program; in this study, the 3DEXPERIENCE of Dassault Systèmes was used. In this program, it is possible to construct a mesh, and, with that, a three-dimensional surface from the cloud of points. Before constructing the final surface, a smoothing process was implemented to eliminate any rough parts. Once the final surface was generated, this surface was extruded and then cut to the proper dimensions to fit into the holder. Finally, the nine holes were made at the bottom to make it possible to tighten the generated block to the holder. A high-level overview of the process discussed in this paragraph is showed in Figure 3.8. Additionally, a summary of all the flexible, rigid and rigid deformed panel parameters is shown in Table 3.2. Note that the parameters shown in Table 3.2 are the values for the middle portion of the panel, where there is a deformation present, except for the rigid case, where no deformation is present.

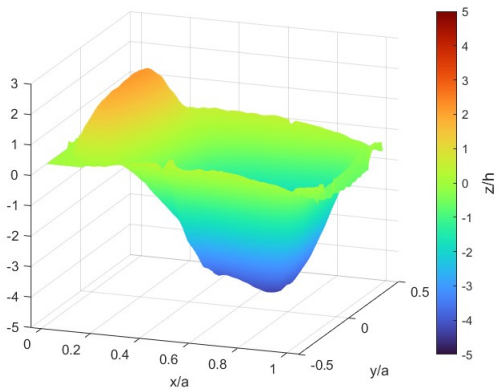

(a) ”Raw” mean deformation from DIC data (*MATLAB*)

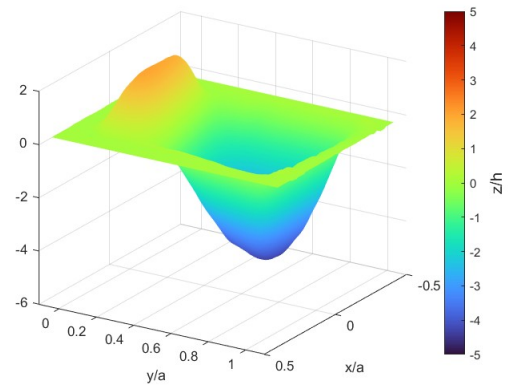

(b) Mean deformation corrected for offsets and treated with MATLAB smooth function (*MATLAB*)

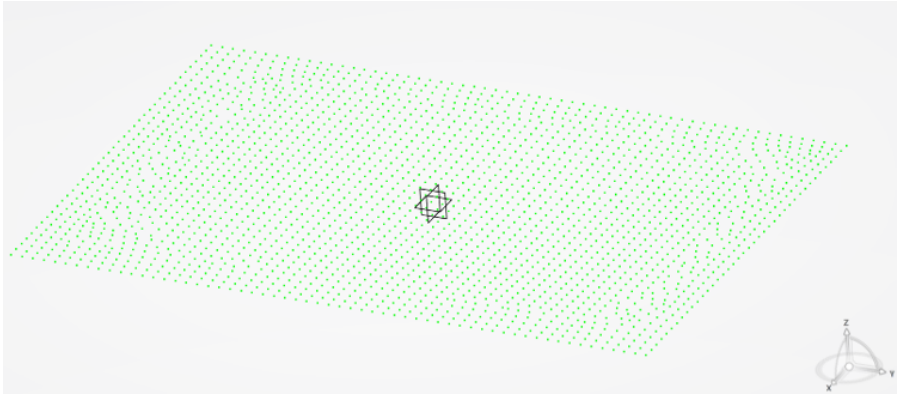

(c) Generated cloud of points in 3DEXPERIENCE (*Digitized Shape Preparation Mode*)

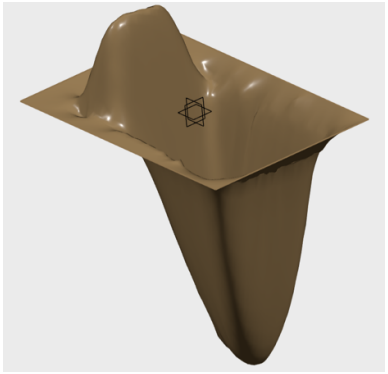

(d) Surface made out of cloud of points; out-of-plane displacements 100x magnified (*Digitized Shape to Surface Mode*)

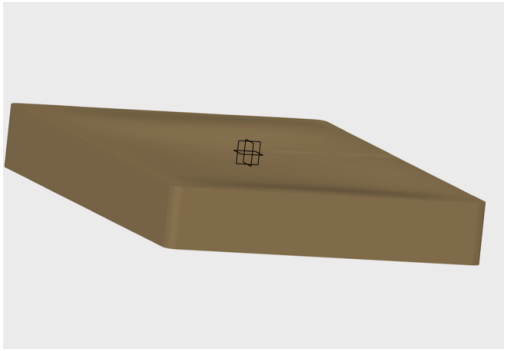

(e) Final CAD design (*Part Design Mode*)

Figure 3.8: High-level step-by-step (from a to e) overview of the production in MATLAB and 3DEXPERIENCE of the rigid deformed plate to be 3D-printed.

Table 3.2: Panel parameters for the thin, rigid and rigid deformed panels.

Parameter	Thin	Rigid	Rigid Deformed
Thickness [mm]	0.3	-	-
Length [mm]	128	143	132
Width [mm]	84	150	90
Material	Aluminium	Aluminium	PLA-CF

3.4 Pressure Measurements

In subsection 2.2.4 the influence of the cavity pressure on the panel deformations is discussed. That is why for the current study it is highly relevant to measure and document this cavity pressure, to be able to explain the physics behind the mean shape of the panel and the displayed flutter. This is done by means of static pressure measurements at the side of the wall, as will be explained in this section.

Working Principle

To measure the static pressure of the flow at the wall of the wind tunnel, small orifices are made in the wall. Those orifices are connected to a pressure transducer that transforms the measurement into a pressure value. An example of such a transducer, as used for this research (see Figure 3.4), is a *gauge pressure transducer*. This type of transducer measures the difference in pressure between the wanted pressure and a reference pressure, such as the ambient pressure. The pressure taps are connected to the transducer through flexible tubes, in which, for a steady flow, it can be assumed that the pressure losses are negligible. A schematic of such an orifice is given in Figure 3.9. The actual pressure can be written as (McKeon & Engler, 2007):

$$p_w = p_{mw} - \Pi \tau_w, \tag{3.1}$$

where p_{mw} is the wall pressure as measured by the transducer, Π is the non-dimensional pressure variation due to errors induced by particular parameters ($\Pi = \frac{\Delta p}{\tau_w}$), and τ_w is the wall shear stress. The error included in Π is generally a function of the following variables (McKeon & Engler, 2007): freestream flow conditions, orifice depth and diameter, Mach number, diameter of the cavity behind the orifice and height of burrs on the edge of the orifice. Going into more detail about the effect of these parameters is outside the scope of this section. Readers who are interested in this are encouraged to read the book by McKeon and Engler (2007).

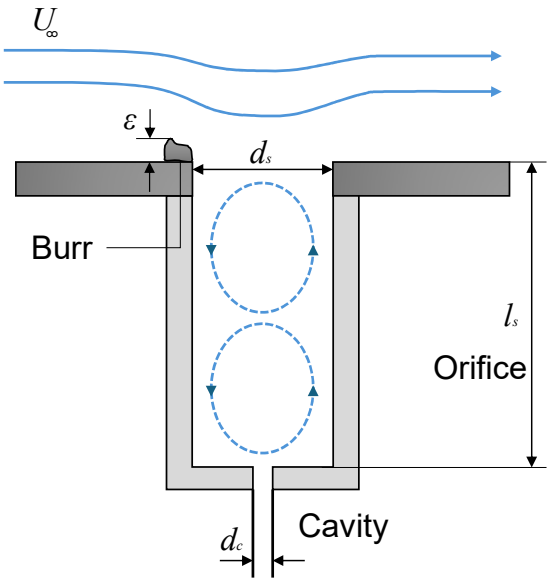

Figure 3.9: Schematic representation of wall taping method for static pressure determination (adapted from McKeon and Engler (2007)).

Side Wall Pressure Measurements in ST-15

The ST-15 wind tunnel has incorporated 12 pressure taps on both sides of the wind tunnel, covering positions in front of and behind the throat, upstream of the test section. In addition, on both sides, there is the possibility to attach a pressure port that has access to the cavity below the test section. The position of these pressure ports on the side of the ST-15 is shown in Figure 3.10. On top of the pressure taps available at the sides of the wind tunnel, there is also a tube connected to the settling chamber, making it possible to measure the total pressure directly during the run.

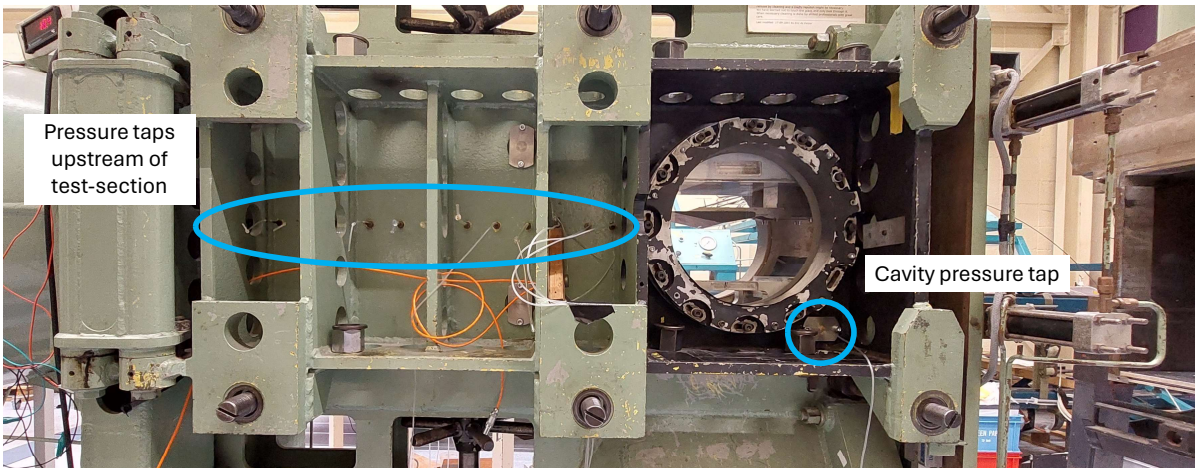

Figure 3.10: Position of pressure taps in ST-15 wind tunnel (Rotterdam side).

The pressure transducer used in this study is the ScaniValve DSA3217/16Px, with a pressure measurement range of 50 psi (≈ 3.45 bar). Figure 3.11 shows the ScaniValve and it can be seen that there are only 16 available connections to one of those pressure scanners. This is less than the total number of pressure ports available at the side of the wind tunnel. Therefore a selection of ports needs to be made.

Figure 3.11: ScaniValve DSA3217/16Px (50 PSID) pressure scanner.

Firstly, entries 1 and 16 are connected to the cavity pressure port and the total pressure port respectively. The other 14 available entries are distributed over the other ports available on both sides of the wind tunnel. Because of the size of the tube coming out at the side, not all of them were suited for a direct connection to the ScaniValve. In the end, at every position except one, a tube from at least one of the sides was connected from the wind tunnel to the pressure scanner. Keeping the REF port open on the ScaniValve (see Figure 3.11) results in measuring the difference in pressure to the ambient pressure. Recall from the previous section that pressure transducers measuring the difference in pressure to a ref-

erence are called gauge pressure transducers, meaning the transducer used in this study is one of those.

The measurement parameters used for measuring the pressure during the experiments are listed in Table 3.3. A LabVIEW program was used, newly developed by a student working at the HSL, which automatically incorporated most of the inputs for the ScaniValve, which are shown in Table 3.3. The program made it possible to export the data in a convenient way for importing it into MATLAB and made it easy to change the measurement parameters. Note for example that the data rate (DR) is not one of the inputs for the DSA module, but rather is defined through the following relation:

$$DR = \frac{1}{PERIOD \cdot 16 \cdot AVG}, \tag{3.2}$$

where $PERIOD$ is the interval between channel samples and AVG is the number of samples the scanner acquires before producing an averaged output. With the values from Table 3.3 this gives a sampling frequency of $41.67\,\text{Hz}$. For more information about each of the input values, the reader can refer to the instruction manual of the DSA module (Scanivalve, n.d.).

Table 3.3: Measurement parameters used by pressure scanner during experiments, used as input for DSA module. TD = test dependent

Parameter	$PERIOD$	AVG	FPS	$XSCANTRIG$	$FORMAT$	$TIME$	EU	ZC	BIN	SIM	$QPKTS$	$UNITSCAN$	$CVTUNIT$	$PAGE$
Value	150	10	TD	0	0	0	1	1	0	0	1	BAR	0.068948	0

3.5 Qualitative Flow Field Organisation

It is not always necessary to obtain quantitative results to understand how the flow and structure behave. Often it is even preferred to start with qualitative measurements to have a general idea of the phenomenon to be studied. In the current study, this is done in the form of schlieren imaging (see subsection 3.5.1) , where the qualitative flow field organisation can be seen, and in the form of oil flow experiments (see subsection 3.5.2), which enables to understand the footprint the interaction has on the panel surface.

3.5.1 Schlieren

Schlieren imaging is a powerful optic technique that enables for the identification of the main flow structures, such as shock waves and expansion waves. This technique is attractive because it has a simple and fast setup compared to other techniques, such as PIV. In this study, schlieren imaging helps in determining the interaction length of the SWBLI structure and some first insights into the unsteadiness of the phenomenon. The aim of this subsection is to introduce the physical principles on which schlieren imaging is based. Moreover, it is shown how such a system is set-up in the ST-15 environment. This section starts with a brief explanation of the working principle behind thermocouples, after which it is shown where the thermocouples are placed in the wind tunnel environment.

Working Principle

Schlieren imaging is an optical method that can be used to visualise density variations in the flow field. This allows for observing flow structures, such as shock waves, acoustic waves and expansion waves, as those structures cause local variations in the density. Schlieren imaging uses the fact that the velocity of light varies through a medium with a varying density, and consequently, the refractive index of the medium (Settles, 2001). The density can be related to the refractive index as follows:

$$n = \frac{c_0}{c} = 1 + K\rho, \tag{3.3}$$

where n is the refractive index, c_0 the speed of light in vacuum, c the local light speed, K the Gladstone-Dale constant and ρ the local density of the medium. The Gladstone-Dale constant, K, depends on the composition of the medium and for the medium of interest, air, it is normally around $2.26 \times 10^{-4}\,\mathrm{m^3\,kg^{-1}}$. Mathematically, the deflection of the light rays in the presence of a gradient in refractive index is described as:

$$\frac{\partial}{\partial s}\left(n\frac{\partial \bar{x}}{\partial s}\right) = \nabla n, \tag{3.4}$$

where s is a spatial coordinate parallel to the deflected light ray. Assuming that the light deflection is small and the beam displacement is normal to the z-coordinate (the coordinate in the spanwise direction of the wind tunnel), $ds = dz$. Furthermore, the refractive index of air can be taken to be unity. These simplifications lead to:

$$\frac{\partial^2 x}{\partial z^2} = \frac{\partial n}{\partial x}; \quad \frac{\partial^2 y}{\partial z^2} = \frac{\partial n}{\partial y}, \tag{3.5}$$

where x is the coordinate in the streamwise direction and y is the coordinate in the wall-normal direction. In addition to this, the light is only deflected inside the test section and, therefore, taking the deflections in the streamwise direction and using the Gladstone-Dale equation (Equation 3.3), the expression above can be integrated from along the width of the test section:

$$\epsilon_x = \frac{\partial x}{\partial z} = \int_0^{W_t} \frac{\partial n}{\partial x} dz = K \int_0^{W_t} \frac{\partial \rho}{\partial x} dz, \tag{3.6}$$

where W_t is the width of the test section. Equation 3.6 shows that the light deflections in the streamwise direction are related to the density gradient in the same direction, integrated in the spanwise direction. A similar expression can be obtained for the deflections in the wall-normal direction.

In practice, it is more complex to obtain a quantitative density field because it involves making assumptions of the density gradient as a function of the spanwise coordinate. Therefore, schlieren imaging is mainly used to obtain direct qualitative information about the flow. In addition to this, the setup is relatively simple. A schematic of such a schlieren setup is illustrated in Figure 3.12, where the setup consists of a light source, mirrors, lenses, a knife edge and a camera to capture the schlieren image.

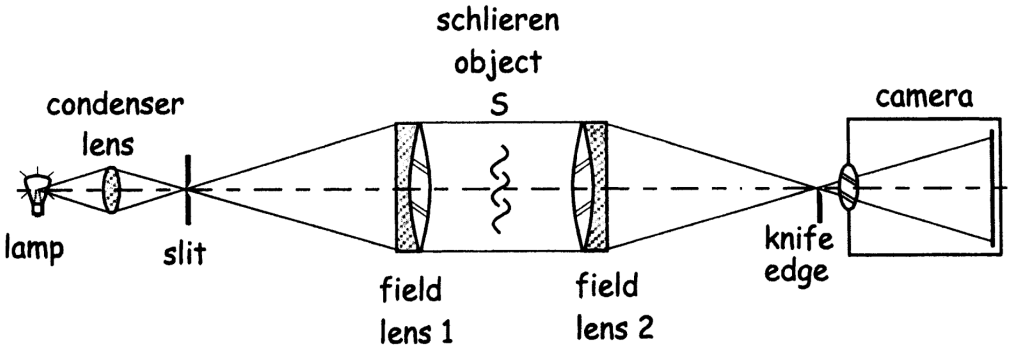

Figure 3.12: Dual-field-lens schlieren arrangement (Settles, 2001).

Firstly, the light from the source is condensed by the condenser lens into a point, where, using a pinhole (slit) the dimension of the light beam can be set. After the pinhole, the light is collimated by a lens such that the light is parallel when going through the test section. After the test section, a second lens focuses the light into a point again. The knife edge is placed in this focal point, allowing for cutting away part of the light going into the camera. The sensitivity of the schlieren system is set partially by

the dimension of the light beam at the knife edge, which in turn should be equal to the dimension of the light beam set by the pinhole. Flow phenomena in the test section change the density of the flow and, by the mathematical basis provided by Equation 3.6, this causes the light to refract and thus go around the knife edge (light area in the image) or be blocked by the knife edge (dark area in the image), depending on the configuration of the knife edge. It is possible to make the schlieren system more or less sensitive to deflections by cutting off more or less light respectively. However, this comes at the expense of the brightness of the image captured by the camera. To solve this, a brighter light source can be used. If, however, the sensitivity is good enough, but the image is too bright, it can also be considered to change the camera exposure.

Z-type Schlieren Configuration in ST-15

This research makes use of a Z-type schlieren configuration. This configuration has the advantage that it can save room because of the folded setup, and it allows for a larger field of view without an increasing number of lenses or mirrors. However, the nonlinear configuration comes at the price of coma and astigmatism. A schematic representation of the configuration as used in the ST-15, together with the actual representation around the ST-15, is shown in Figure 3.13.

After the light source, a collimating lens and a normal lens are placed to collimate and converge the light, such that the light is focused in a pinhole. The size of the latter component controls the intensity of the collimated beam, and therefore the sensitivity of the system. A set of normal and parabolic mirrors is used to direct the light through the test section and to the camera sensor. For the light to be collimated through the test section, it is important that the pinhole is in the focal point of the first parabolic mirror. On the other side of the tunnel, before entering the camera, a knife edge is present, which cuts away part of the light beam, making it possible to visualise the density gradients. As the knife edge is set in the vertical direction, the used configuration is sensitive to streamwise density gradients. It is required that the knife edge is placed in the focal point of the second parabolic mirror for the gradients to be visible. Otherwise, part of the image would be simply be cut away, rather than the entire image becoming lighter or darker.

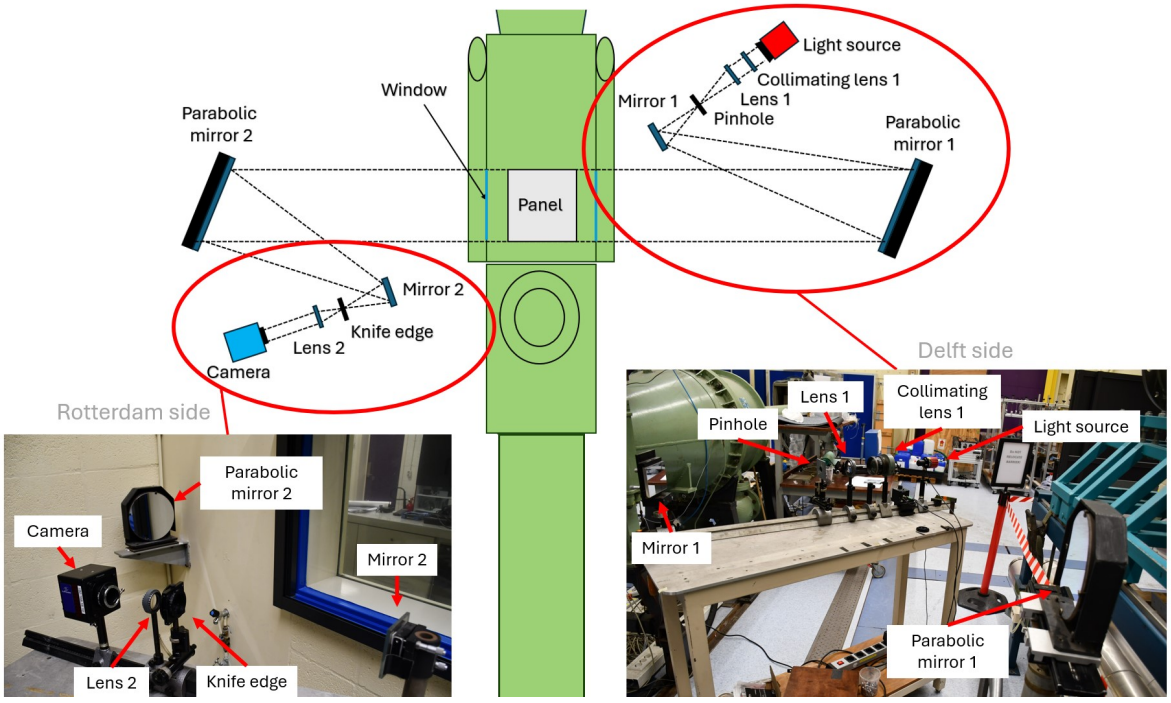

Figure 3.13: Schlieren setup used in ST-15 wind tunnel facility.

After the knife edge, another lens is present to focus the image onto the camera sensor. This lens ensures that the proper field of view (FOV) was captured by the sensor. For the current study, a Photron FASTCAM Mini AX100 was used to record images at a frequency of 7200 Hz and a resolution of 1024 $\times$ 608 pixels. The chosen acquisition frequency ensures that frequency phenomena can be captured and reconstructed up to a frequency of 3600 Hz without aliasing. For each run, 10000 frames where saved, resulting in a total saved test time of around 2.5 s. Table 3.4 contains an overview of the components and their relevant specifications as used during the schlieren experiments.

Table 3.4: Specifications of used schlieren equipment.

Equipment	Description
Light source	Thorlabs MCWHLP1 White LED
Collimating lens	F2.5 f = 178 mm
Converging lens 1 & 2	f = 200 mm
Knife edge orientation	Vertical
Parabolic mirrors	f = 2000 mm
Camera	Photron FASTCAM Mini AX100

3.5.2 Oil Flow Visualisation

In many applications, it is not only interesting to understand what happens in the flow around the object, but also how the air flows at the surface of the object. This gives insight into flow phenomena such as flow separation and recirculation. A simple way to obtain this qualitative information is by putting coloured oil on the surface and observe how it is pushed around at the surface by the incoming flow. The aim of this subsection is to explain how Oil Flow Visualisation works and how this technique was used in the ST-15 wind tunnel.

Working Principle

Oil Flow Visualisation (OFV) generally determines the velocity direction near a surface and some basic flow features, such as separation and steady vortices. This technique is purely qualitative and, in most cases, provides time-averaged flow streamlines close to the surface, as the response time of the oil is too large for it to react to higher frequency responses of the flow. The method operates based on a high-viscosity layer, such as oil, moving due to friction from the airflow around the model. Because of the low velocity and Reynolds number (creeping flow) the advective inertia forces are negligible compared to the viscous forces. At the interface between the air and the oil, there is a no-slip condition, which imposes an equal velocity for both fluids (see schematic in Figure 3.14), as well as the shear stress being continuous at this interface. The velocity slope in the thin oil layer is much smaller than in air as the dynamic viscosity of oil is larger, resulting in a balance between viscous forces and the pressure gradient in that layer. That is why when the pressure gradient is small compared to the wall shear stress, the oil gives a good indication of the flow direction. However, in the case of separation, pressure forces become dominant, thus the skin-friction lines are not visualised correctly.

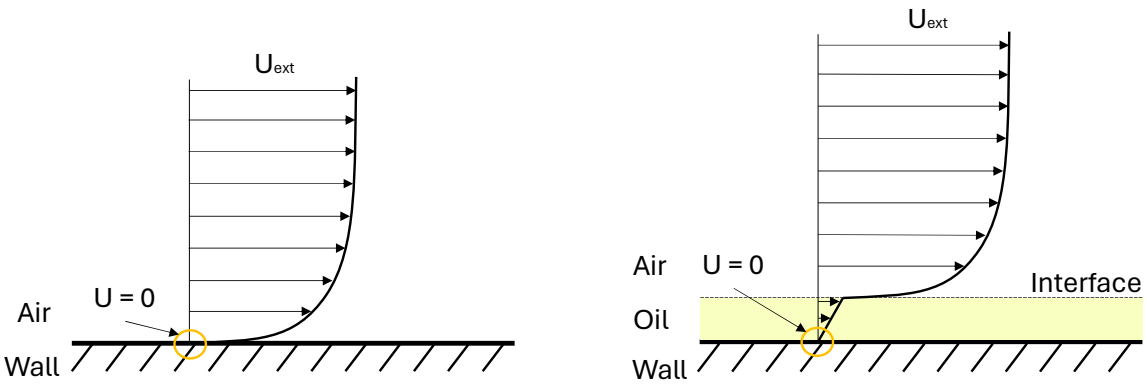

Figure 3.14: Schematic representation of boundary layer profile without and with oil layer.

Oil Flow Experiments in ST-15

To perform an oil flow experiment a simple camera, that can record, suffices. The recorded video can be used to visualise the development of the oil pattern on the surface of the plate during the run and to see if any oil is pushed away at the end because of the passing shock wave at shut-off. On top of the camera, a light source is used for brighter recordings. Afterwards, the plate can be taken out of the test section and a picture can be taken of the pattern. In Figure 3.15 the setup used for the oil flow visualisation is shown, together with a schematic to illustrate the position of the camera and light source to the wind tunnel.

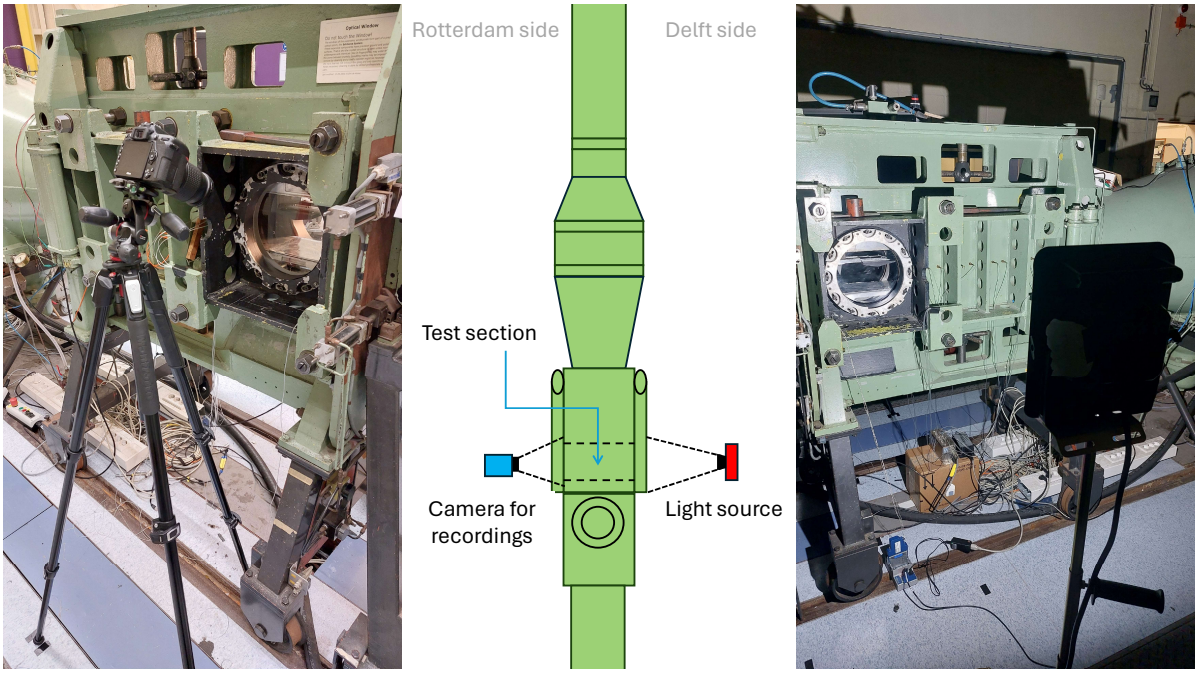

Figure 3.15: Setup of camera and illumination for oil flow visualisation experiments in ST-15 wind tunnel facility.

Before the run, the oil must be applied to the plate. This has to be done in a ”quasi-random” pattern, as shown in Figure 3.16, such that no preferential directions are created for the oil to flow along. Two cameras were used for the OFV: the NIKON D7500 and the Fujifilm X-E3. The reason for using two different cameras is the limited availability of the NIKON D7500 at the HSL. Most of the recordings and photos are therefore taken with the Fujifilm X-E3. As OFV is a qualitative technique and the patterns

seen on the surface are captured well by both cameras, the (little) differences between the cameras are not important. Depending on the light source available, the f-stop and exposure time of the camera had to be changed accordingly. At the same time, in all the cases both cameras used a lens with a focal length of approximately 55 mm.

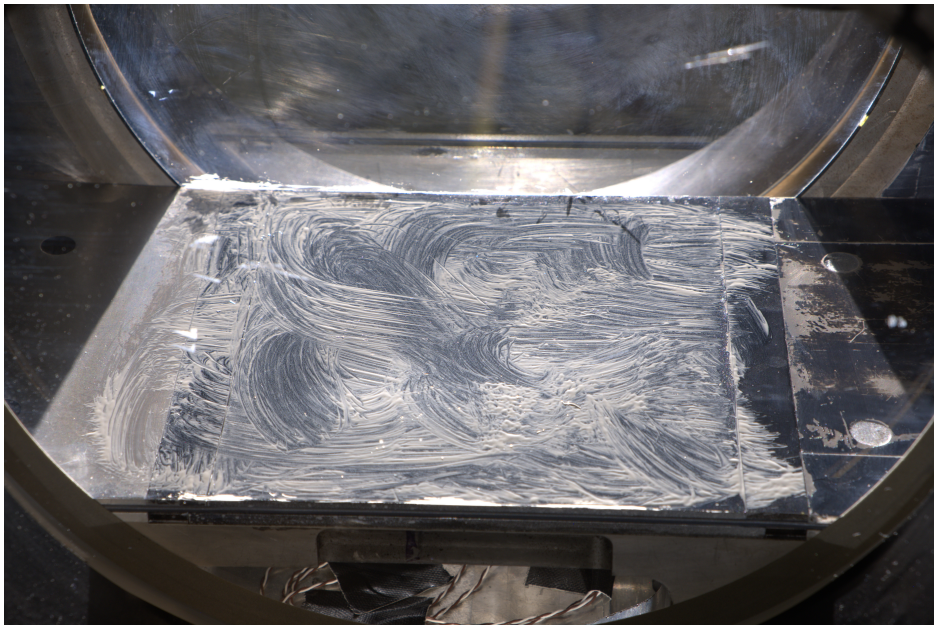

Figure 3.16: Oil layer applied to the plate before the run.

3.6 Temperature Measurements

One of the relevant boundary conditions to track in supersonic flow is the temperature; more specifically, the plate temperature and possible gradients could greatly influence the movement of the plate. That is why some attention is given to this boundary condition through temperature measurements. In subsection 3.6.1 the infrared imaging technique is introduced, while subsection 3.6.2 explains the use of thermocouples inside the wind tunnel environment.

3.6.1 Infrared Imaging

One way to measure the plate temperature is through infrared imaging. This technique enables measuring the plate's surface temperature in a simple and non-intrusive way. The aim of this subsection is to briefly explain the working principle of this technique, after which some practical considerations are given in the set-up of the system.

Working Principle

Infrared imaging follows the principle of spectral emittance of a black body. For such a body, the wavelength at which the maximum spectral emittance occurs at a specific temperature can be calculated using Wien's law:

$$\lambda_{max} = \frac{b}{T}, \tag{3.7}$$

where b is Wien's displacement constant, equal to $0.0029\ \text{m} \cdot \text{K}$, T the surface temperature of the object. Equation 3.7 predicts that bodies with a surface temperature of about 300 K mostly radiate in the infrared spectrum, making infrared imaging attractive for these bodies. However, proper radiation detectors are required. For the imaging system to convert the detected radiation into a voltage, a calibration procedure

is needed. This can be done by taking a reference black body at a known and controlled temperature and recording the output. A calibration curve can be established by repeating this process for multiple temperatures, making it possible to link the camera output to surface temperatures for black bodies. As normal glass has a low transmissivity in the infrared spectrum (i.e. they seem opaque), Germanium windows are generally used for the optical access of wind tunnels when using infrared imaging because of their high transmissivity in this range. Thus, infrared imaging is a relevant measurement technique for temperature measurement because the maximum spectral emittance of the expected temperatures occur in this range; adequate measures have to be taken to capture this type of radiation.

Infrared Imaging in ST-15

In practice, in the ST-15 wind tunnel environment, a couple of additional considerations have to be considered. First of all, the Germanium window used in this study is smaller than the normal window, making the optical access to the tunnel smaller as well. Nevertheless, the thin portion of the aluminium panel was entirely within the field of view, thus no relevant panel information was lost. Furthermore, because of the low emissivity of aluminium, the surface acts as a mirror. As a consequence, the infrared camera does not measure the true panel temperature, but rather the reflected temperature from other surfaces. To resolve this, the panel had to be painted with black paint, such that the emissivity of the surface was raised, and the true temperature of the panel could be captured by the camera.
The camera used in the experiment, the Optris PI640, together with the software, already provides calibration curves, such that the user does not have to do this beforehand. On top of this, the camera has a sensor adjusting for temperature effects because of heating or cooling of the camera itself. Figure 3.17 shows how the camera and the Germanium window are setup for the current study in the ST-15 facility.

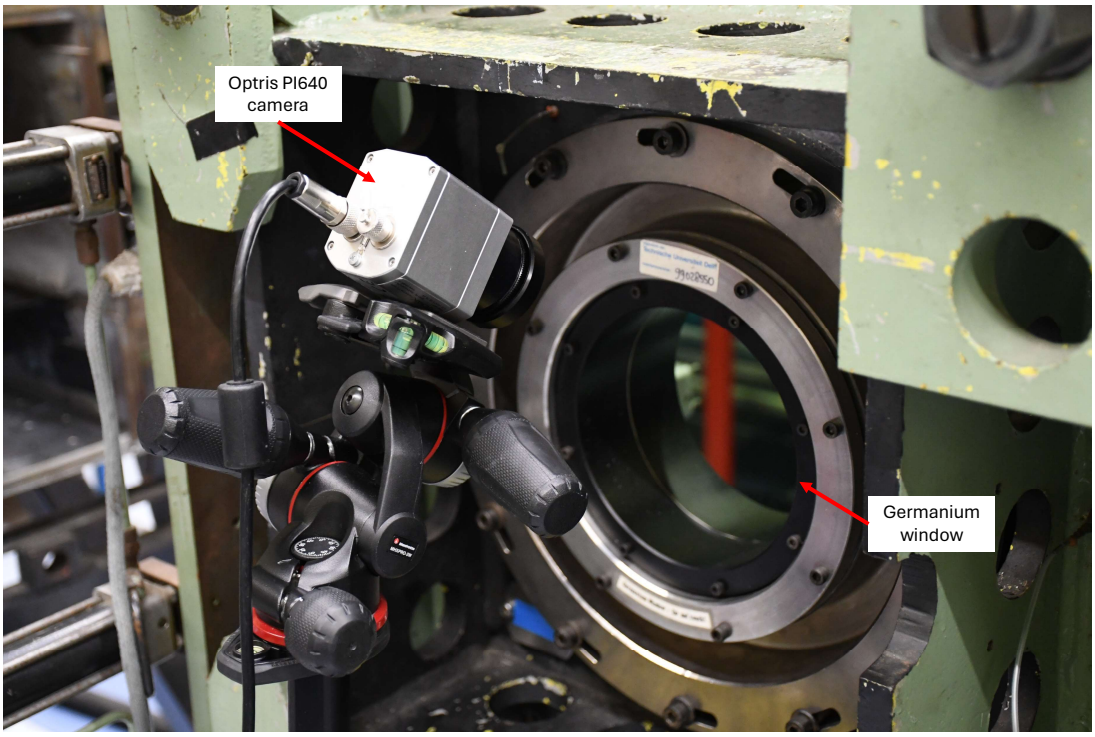

Figure 3.17: Infrared imaging setup in ST-15 wind tunnel facility: infrared camera looking through a Germanium window.

3.6.2 Thermocouples

Without optical access, obtaining temperature information with infrared imaging is impossible. Furthermore, as a special germanium window is needed to use the infrared camera, this would necessitate the continuous use of this window, constraining the optical access for other optical measurement instruments. That is why in this subsection, the use of thermocouples (TC) is discussed, as they can be used in locations where there is no optical access but temperature data is still desired, such as in the cavity underneath the panel.

Working Principle

The driver behind the working principle of thermocouples is the *Seebeck effect*, which describes how "the *Seebeck electromotive force* (emf) is the internal electrical potential difference that is viewed externally as a voltage between the terminals of a thermocouple" (American Society for Testing and Materials, 1993). In practice, this occurs in conducting materials where the temperature is not uniform across the material. The governing relation used to calculate the absolute Seebeck emf in a single material with inhomogeneous temperatures at its ends is called the *fundamental law of thermoelectric thermometry* and is given as:

$$dE_\sigma = \sigma(T)\, dT, \tag{3.8}$$

where E_σ is the Seebeck emf, σ is the Seebeck coefficient and T the temperature. In reality, however, two different materials are used, such that there is a relative Seebeck emf of the pair of materials. This relative Seebeck emf between materials A and B is written as, by using Equation 3.8:

$$E_{AB} = (E_\sigma)_A \Big|_{T_1}^{T_2} - (E_\sigma)_B \Big|_{T_1}^{T_2}, \tag{3.9}$$

where E_{AB} is the relative Seebeck emf of the pair and T_1 and T_2 are the temperatures at the ends of both materials. The relation above states that the relative Seebeck emf of a pair of materials is the difference in absolute Seebeck emf of the individual materials. With this dependence between the induced voltage and the temperature at the free ends and the junction of the two materials, it is possible to perform temperature measurements. With the development of modern electronics, it is not needed anymore to keep the free ends of the thermocouples in a real reference temperature environment (e.g. an ice bath of known temperature) but rather this reference temperature is obtained electronically.

Thermocouple placement in ST-15

Thermocouples need to be connected to the environment outside of the wind tunnel. Therefore, their placement inside the cavity is not trivial and requires a particular solution. The problem to tackle is the fact that it is desired to keep a constant pressure inside the cavity during a run. Any holes connecting the cavity to the outside environment would change this and make it equal to atmospheric pressure. To solve this problem, the hole connecting the cavity and the outside environment is filled with plasticine. The use of this product has proven to keep the cavity pressure, once pressurised by tunnel start-up, constant, and therefore, deemed as an appropriate solution for the thermocouple connection.

The thermocouples themselves are placed in various locations. Two thermocouples, as shown in Figure 3.18a, are placed onto the plate: one on the frame of the panel and one at the edge of the thin portion. For a rigid plate, the entirety of the panel can be considered as the frame. A third thermocouple is attached to the bottom of the cavity and placed such that its end is completely in the air (see Figure 3.18b). This way, the ambient temperature inside the cavity is measured. Finally, a fourth thermocouple was sometimes attached to the plate closing the cavity. This thermocouple enters the wind tunnel through a hole downstream of the test section and just upstream of the diffuser, such that no interference is created with the measurements in the test section and the cavity.

(a) Thermocouple placement at the bottom of a thin panel inserted in the lower Mach block of the ST-15 wind tunnel.

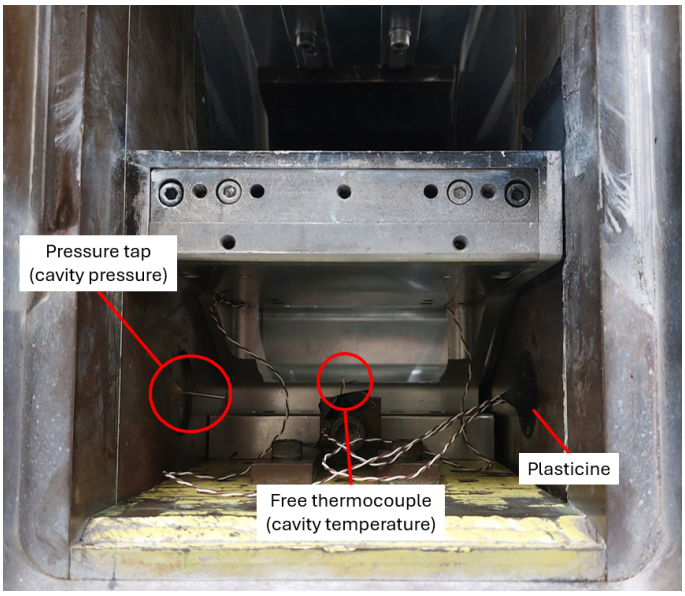

(b) Cavity setup with thermocouples coming in from outside environment and protected with plasticine against pressure losses. Thermocouple in the air and pressure tap are present to measure cavity temperature and pressure respectively.

Figure 3.18: Thermocouple placement (a) at the bottom of a thin plate and (b) with free end in the air for measurement of plate temperature and cavity temperature respectively.

3.7 Digital Image Correlation

Part of the fluid-structure interaction is the structural deformation of the panel. This makes the measurement of the structural movement a significant part of the test campaign where it becomes desirable to do it by means of a non-intrusive method. Any intrusive measurement technique would interfere with the movement and the panel and therefore contaminate the results. That is why it was chosen to make use of the digital image correlation (DIC) technique, which makes use cameras to measure the out-of-plane displacement of the panel. The aim of this section is to briefly explain the working principle of this technique, after which it is explained how this technique was set-up in the ST-15 environment.

Working Principle

DIC is an optical, non-intrusive measurement technique used to measure full-field deformations of a surface. The DIC process starts before its setup with the creation of optical markers on the surface of the specimen of interest. The markers are illuminated with a light source and their displacement tracked with two cameras. For the tracking to be possible, the contrast between the background and markers needs to be high enough. Rather than tracking individual markers, DIC estimates the average displacement of a group of markers, also called a *subset*. This solves two problems that arise when tracking individual markers: the *aperture problem* and the *correspondence problem* (Schreier et al., 2009). The aperture problem describes the problem where, if the displacement of the individual marker is greater than the size of the interrogation window, no match in subsets can be found between two images such that the displacement can be determined. The correspondence problem describes the problem where it becomes ambiguous to find the single marker between two images because the grey-scale value of the marker may match the value of other markers in the image. Tracking a pattern of smaller markers instead of individual markers solves these problems and makes it possible to have a higher spatial resolution and more accurate results. In practice, the displacement is found through the cross-correlation technique, indicating for which shift the image pair of the chosen subset corresponds to one another. An example of a cross-correlation map is shown in Figure 3.19.

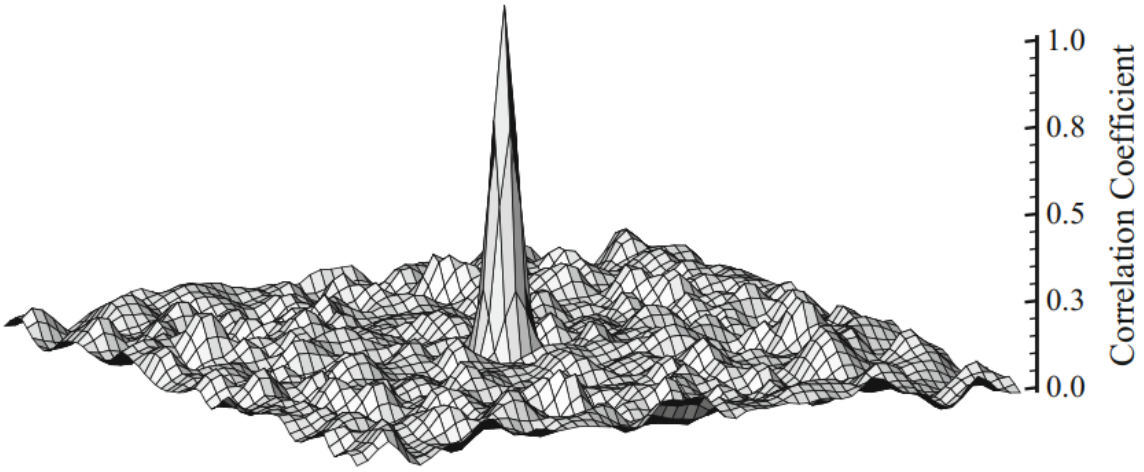

Figure 3.19: Correlation map of a shear flow with multi-step correlation and window deformation (Raffel et al., 2018).

The quality of the speckle pattern has a strong influence on the accuracy of the DIC results (Roncella et al., 2012), and this quality is determined by several parameters:

- **Speckle distribution**: ideally, the distribution should be isotropic, i.e. the speckles should not show any preferred direction. The pattern should be non-periodic and random, minimising mis-registration problems (Schreier et al., 2009).
- **Speckle size**: the speckles should be large enough such that peak-locking is avoided. This phenomenon occurs when the size of the speckle is smaller than the size of the pixel and therefore the sub-pixel displacement of the speckle cannot be tracked accurately (see Figure 3.20). At the same time, it is desirable to have small speckles for higher spatial resolution.
- **Speckle density**: the speckle density is determined by the size of the speckles and the number of speckles per subset. The accuracy of the measurement increases both when the speckle size increases and the number of speckles per subset increases. For a fixed subset size, these two parameters limit each other, leading to a trade-off between the two parameters.
- **Speckle edge sharpness**: the gradient of contrast at the edge of the speckle should be low enough, such that aliasing and measurement bias are avoided.
- **Image contrast**: the difference in grey value between the background and the speckled should be high enough, such that there is less uncertainty in the matching of subsets. This can be achieved through the correct choice of paint for the speckles and illumination during the data acquisition.

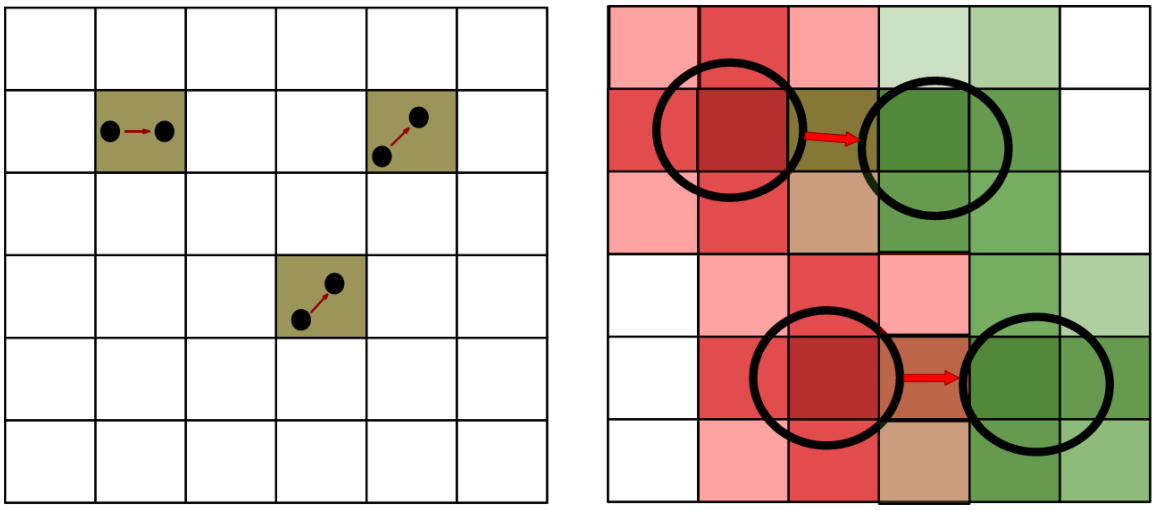

(a) Under-resolved particles.

(b) Well-resolved particles.

Figure 3.20: Subset schematics with displaced markers of a different size, wherein a) the markers are under-resolved, leading to peak-locking, and b) the markers are well-resolved (Kislaya, 2016).

Another important factor for the accuracy of the results is the choice of the subset size. Pan et al. (2008) have shown that an increasing subset size decreases the standard deviation of the in-plane displacement measurements. However, this comes at the cost of a lower spatial resolution. Other considerations to be made are the illumination and the position of the cameras. Reu (2013 argues that for DIC the light source should be ”flat, uniform, and of adequate intensity”. In practice, LEDs provide the best lighting for DIC experiments because they can provide a lot of light without producing too much heat. On the recording side, to measure not only in-lane displacements but also out-of-plane displacements, it is required that the cameras are positioned in a stereographic configuration (Schreier et al., 2009). A similar consideration is also valid for PIV, where one would need two cameras in a stereographic configuration to measure all three velocity components of the flow. For PIV it is preferred to have an angle of 90 ° between the two cameras, while for DIC an angle of 45 ° is the best for reducing the uncertainty for out-of-plane measurements (Schreier et al., 2009).

DIC Setup in ST-15

For the recording of the DIC images, a stereographic configuration was used, utilising the optical access to the wind tunnel at one of its sides. For this, two Photron FASTCAM Mini AX100 were used, which were placed at an angle of approximately 45° on top of an X-95 beam structure; this angle is equal to the optimum angle for DIC as suggested by Schreier et al. (2009) for the measurement of out-of-plane panel displacements. Additionally, a white LED-Flashlight 300 was placed in between the two cameras, acting as a strong light source to illuminate the speckle pattern on the panel. The placement of these components around the wind tunnel is shown schematically in Figure 3.21.

All of this equipment was connected together to a programmable timing unit (PTU), allowing for a synchronised trigger of the cameras and the LED. The setup as described above is shown in Figure 3.22. From this figure it becomes evident that there are a lot of connections between the different components. The Ethernet cables are needed such that the computer can find the cameras, add them to the DaVis software and visualise what the cameras see. Similarly, the PTU is connected to the computer by means of an USB cable. The connections between cameras, LED and PTU is done by means of BNC cables, such that trigger signals can be sent by the PTU to the components. Figure 3.22 shows in detail how these cables should be connected.

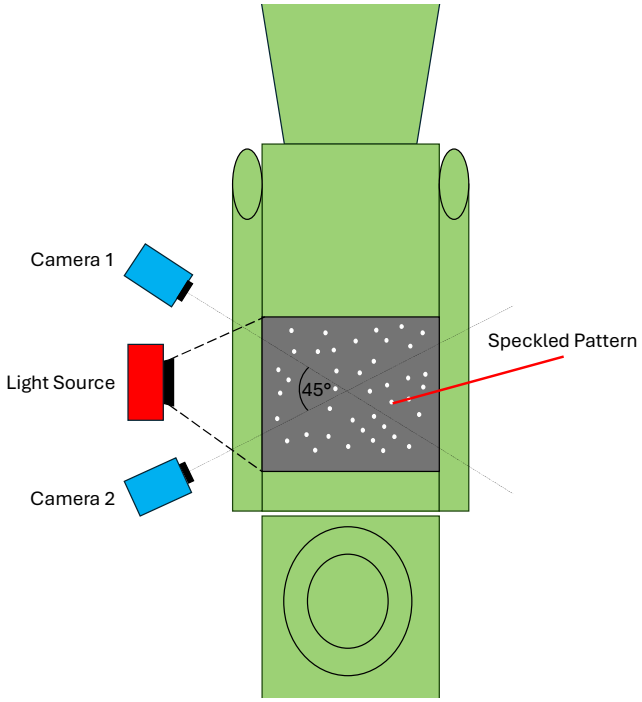

Figure 3.21: Schematic representation of DIC setup from top view.

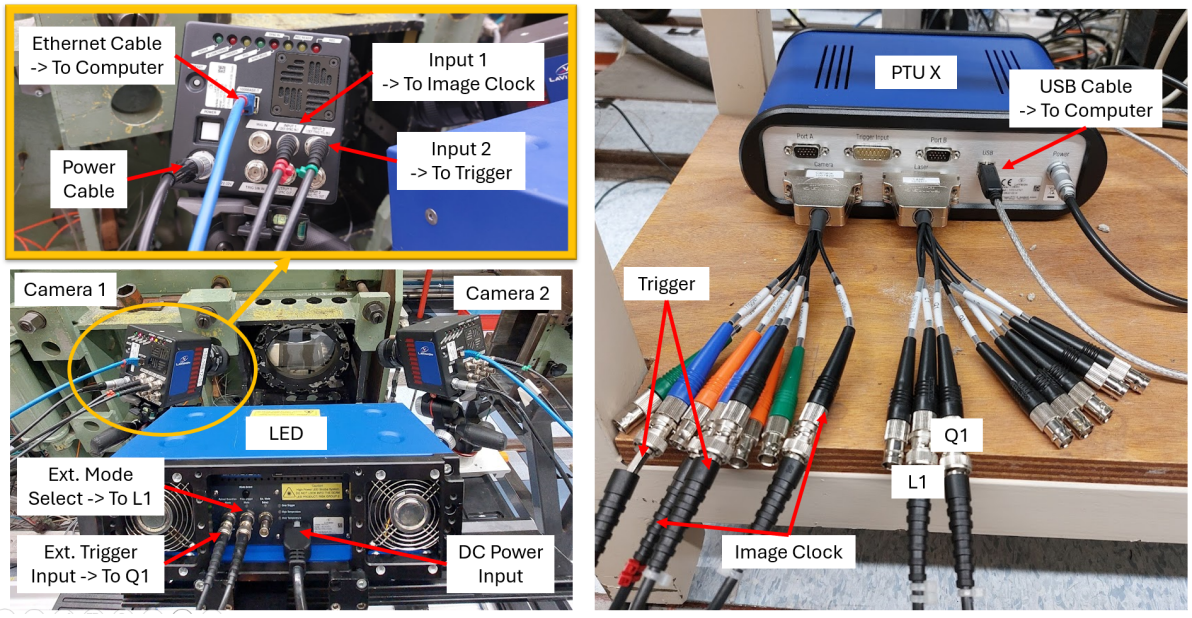

Figure 3.22: DIC setup showing the connection between cameras, LED and PTU.

To provide the proper field of view (FOV) and good image quality, particular care should be given to the set-up of the cameras. Both cameras used a lens with a focal length of 460mm to allow for the capturing of the entire thin portion of the panel. To achieve the same acquisition frequency of the cameras as Allerhand (2020) and Aditya (2022), the full resolution of 1024x1024 pixels had to be cropped to a resolution of 1024x860 because of the memory storage capacity of the cameras. Scheimpflug adaptors were fitted between the camera and the lenses, for the cameras are at an angle with respect to the horizontal plane of the panel. This adaptor corrects for this angle and ensures that the focal plane

is parallel to the panel surface. This plane, which represent the depth-of-field (DOF) of the camera, should be wide enough, such that the entirety of the speckle pattern is in focus during its fluttering motion. The DOF depends on the $f_\#$ of the lens, which was set to 11, similar to Allerhand (2020). This $f_\#$ also provided enough light into the camera for proper contrast between the panel background and the speckle pattern. An overview of the equipment specifications is given in Table 3.5.

Table 3.5: Measurement parameters used during the DIC test campaign

Parameter	Value
Camera	2 × Photron FASTCAM Mini AX100
Stereo-angle	45 °
Resolution (full)	1024 × 1024
Resolution (used)	1024 × 860
Pixel size	20 μm × 20 μm
Acquisition frequency	5000 Hz
Acquisition time	2 s
Lens	Nikon 60 mm
$f_\#$	11
Magnification factor	0.1024
Spatial resolution	5.1 px/mm
Illumination	LaVision LED-Flashlight 300 (White)
LED pulse duration	20 μs

A good contrast between the panel background and the speckle pattern was achieved by first painting the panel with two layers of black, matte paint, followed by the appliance of a white pattern. In contrast to previous experiments, instead of using an air brush because of its unavailability, the pattern was applied directly with a spray can. This led to a bigger variety of speckle size of approximately 3 to 11 pixels in diameter, as well as a less controlled speckle density. The use of a proper nozzle is recommended to prevent accidental, large splashes of paint on the panel. Nevertheless, a good isotropic and random pattern was achieved, minimising directional bias and misregistration problems (Schreier et al., 2009). An example of a used speckle pattern on a plate is shown in Figure 3.23.

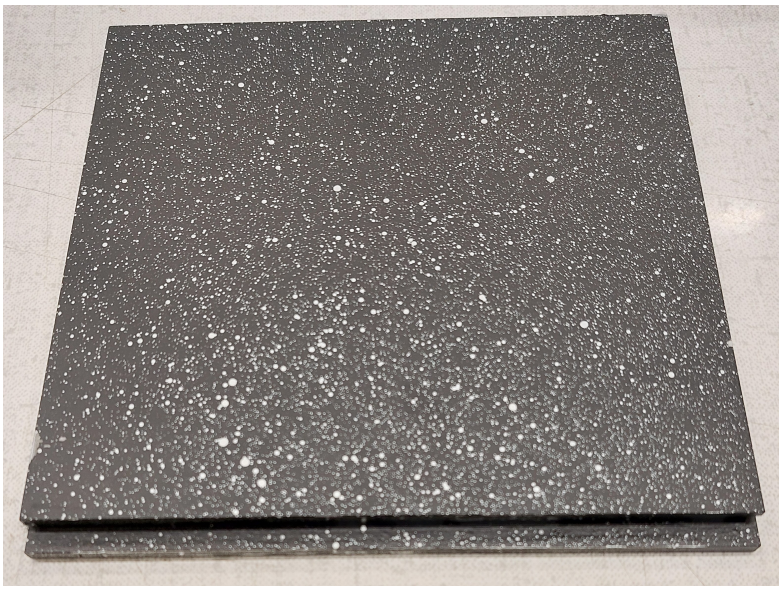

Figure 3.23: Example of applied speckle pattern on rigid plate.

3.8 Particle Image Velocimetry

The other part needed to analyse the fluid-structure interaction for a fluttering thin plate is the understanding of the flow going over it. Similar to DIC, it is possible to artificially introduce particles that are captured by cameras for the reconstruction of the velocity field. This technique is called particle image velocimetry (PIV). Over the past decades, PIV has become very popular and successful as it allows for the measurement of the instantaneous velocity field within a plane or even within a three-dimensional volume. In this section, the working principle of PIV is explained, as well as the setup in the ST-15 wind tunnel.

Working Principle

Similar to DIC, discussed in section 3.7, the principle of PIV is based on measuring the displacement of small illuminated particles that follow the fluid over a short time. The tracer particles need to be chosen accordingly, such that they follow the local fluid velocity with acceptable fidelity. This criterion is quantified using Stokes' number, given as:

$$S_k = \frac{\tau_p}{\tau_f}, \tag{3.10}$$

where τ_p is the response time of the particle and τ_f is the characteristic time scale of the flow. The latter can be estimated by dimensional analysis as the ratio between the flow length scale, L_f and the characteristic velocity of the flow. The particle response time can be estimated using:

$$\tau_p = d_p^2 \frac{\rho_p}{18\mu}, \tag{3.11}$$

where d_p is the particle diameter, ρ_p the particle density and μ the dynamic viscosity of the fluid. As a rule of thumb, the flow tracing by the particles is considered good enough for $S_k < 0.1$. Once the particle is chosen, the flow is seeded with a particular concentration with a seeding machine. The particles are illuminated by a thin laser sheet, of which the light is scattered upon interaction with the particles. This light scatter needs to be large enough for the camera(s) to detect the particles. Thus, a trade-off in particle diameter is required, such that enough light is scattered upon interaction with the laser sheet, while still having an acceptable response time. The tracer particles are illuminated twice within a short time interval, the pulse separation time, Δt, such that two images are obtained in which the particles have moved little. Each image pair is divided into *interrogation windows* of $M \times N$ pixels. In a similar fashion as DIC, in every interrogation window, the cross-correlation map is computed, indicating for which shift in pixels the two windows match the most, as shown with an example in Figure 3.19. In other words: the cross-correlation operation gives an estimate of the average particle image displacement. As the time between the two images, Δt, is known, it is possible to determine the average velocity of the particles in each interrogation window. Doing this for all interrogation windows results in the velocity field in the entire image. A schematic of a typical setup is shown in Figure 3.24, which visualises how the elements discussed come together.

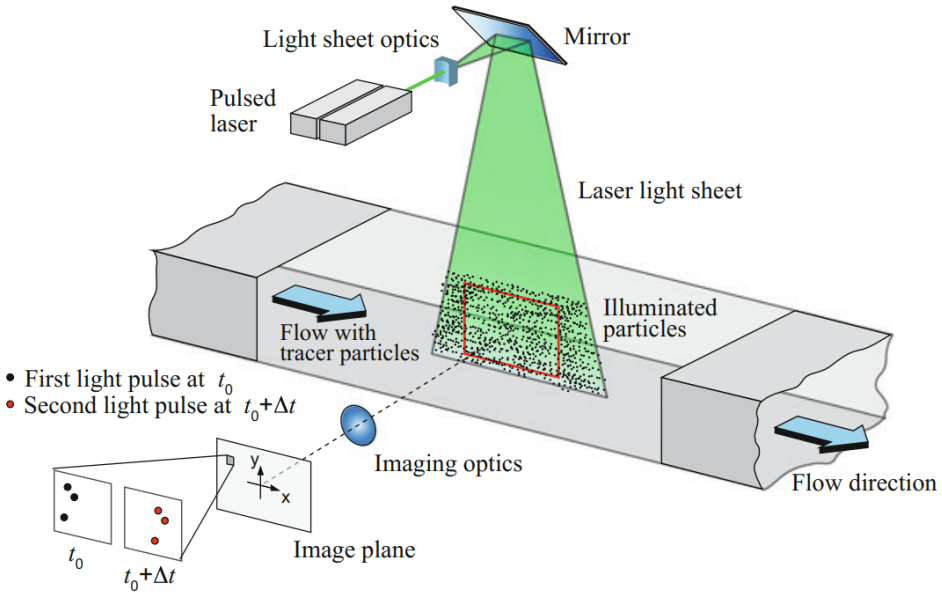

Figure 3.24: Experimental arrangement for planar 2C-2D PIV in a wind tunnel (Raffel et al., 2018).

High-Speed PIV Setup in ST-15

Rather than using a stereographic configuration as with DIC, the used PIV configuration is a planar configuration, using only a single camera perpendicular to the sheet of illuminated particles. As in DIC, a Photron FASTCAM Mini AX100 was used for the recording of the images. Instead of a LED, a green high-power laser, the Quantronix Darwin-Duo 527-80-M, was used to illuminate the particles. This laser is controlled by a control unit as shown in Figure 3.25, which is triggered by signals coming from the PTU. The control unit forwards these signals to the laser itself, firing the two separate pulses the laser contains. The pulses are then deflected by means of two mirrors into a probe, containing several lenses that are used to form the required laser sheet. Inside the tunnel, downstream of the test section, another mirror is present deflecting the formed streamwise sheet towards the test section.

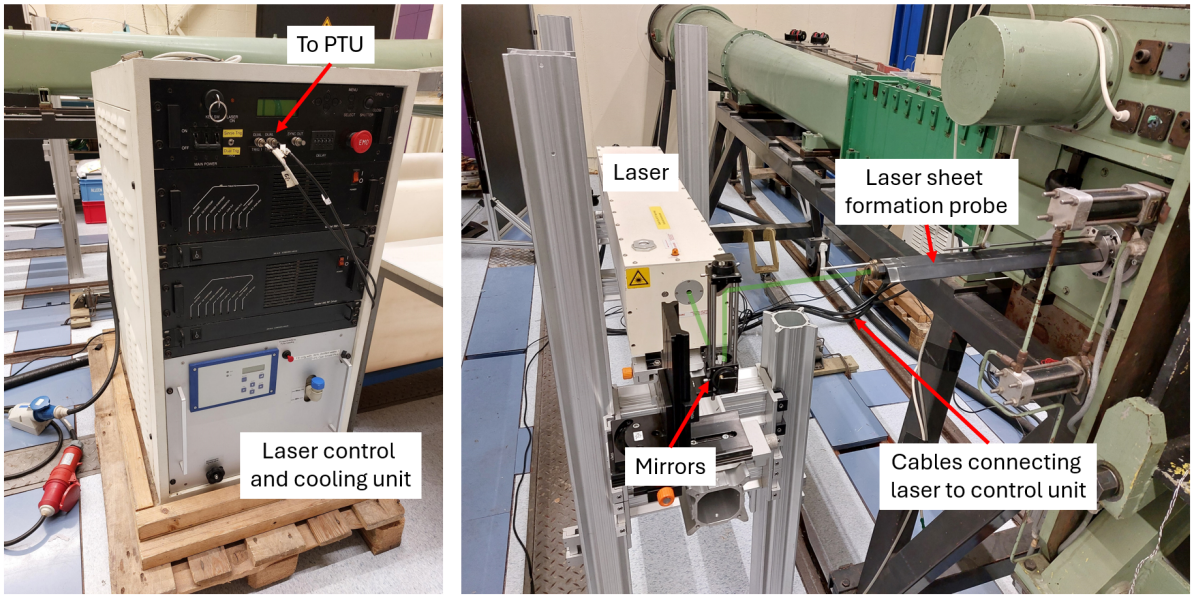

Figure 3.25: Laser sheet setup containing laser control unit (left), laser (right) and laser sheet formation probe (right).

The camera position, relative to the test section, is shown in Figure 3.26. Similar to the DIC setup (see Figure 3.22), the camera is connected to the PTU through BNC cables and to the computer through an Ethernet cable. Furthermore, the camera is again mounted with a 60 mm lens. To receive enough light during exposure, the acquisition frequency was also lowered, as compared to DIC, to 4000 Hz. This allowed for the recording of around 11,600 images, which corresponds to an acquisition time of 2.9 s. In order for all the particles, which are illuminated by the laser sheet with a thickness of 1.5 mm, to be in focus, a proper $f_\#$ needed to be chosen to ensure that the DOF was larger than the laser sheet thickness. The DOF and the $f_\#$ are connect through the following relation:

$$\delta_z = 4.88\lambda f_\#^2 \left(\frac{M+1}{M}\right)^2, \tag{3.12}$$

where δ_z is the DOF, λ the wavelength of the laser sheet and M the magnification factor of the resulting image. This magnification factor is the ratio between the size of the magnified image of an object on the camera sensor and the size of the object itself. This, in turn, can be written as:

$$M = \frac{\text{pixel size} \cdot \text{N pixels sensor}}{\text{FOV}}. \tag{3.13}$$

The relevant FOV was chosen to be 108 mm, which using Equation 3.13 results in a magnification factor of $M = 0.19$. Combining this with a $f_\#$ of 5.6, the DOF is computed to be $\delta_z = 3.16$ mm. As this value is larger than the laser sheet thickness, it means that all the illuminated particles within the laser sheet can be put into focus by the lens.

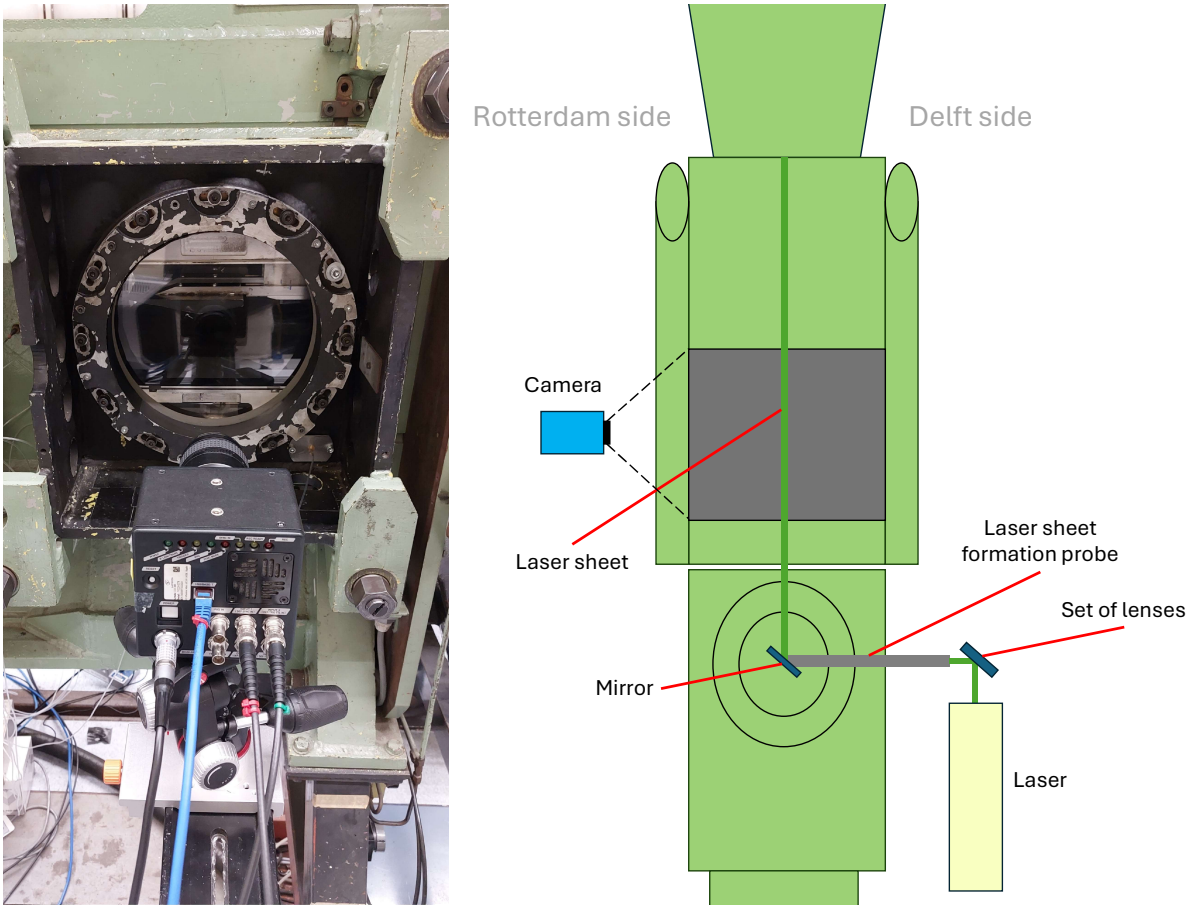

Figure 3.26: Camera setup for PIV experiment, together with schematic TOP view representation of the setup.

The seeding used during the PIV experiment was made out of di-ethyl-hexyl-sebacate (DEHS) droplets for their proven time response and light scattering properties in the ST-15 environment (Ragni et al., 2011). The readily available PIVTEC Aerosol Generator PivPart 45 was used for introducing the droplets into the wind tunnel, in combination with a remote control panel, making it possible to operate the seeding generator during the test from the control room. Test runs showed that with all seeding nozzles active, it was difficult to distinguish the single particles, making it hard to perform cross-correlations. In addition to this, too much seeding would also lead to accumulation of seeding onto the mirror leading the laser sheet into the wind tunnel environment. This possibly leads to the defocusing of the laser during the run (Allerhand, 2020). That is why the number of active nozzles was decreases during the runs, similar to what was done by Allerhand (2020). Nonetheless, the mirror had to be cleaned between every run to ensure the maximum laser quality. During the runs themselves, irregular seeding was observed, which was also noticed by Allerhand (2020) and attributed to a combination of the "intermittent operation" of the nozzles, the unsteadiness of the SWBLI flow structure and the strong inertial forces because of the high flow velocities.

The laser position was positioned in the middle of the wind tunnel, allowing for measurements at the mid-span location on the panel, as DIC measurements confirmed that at this location the deformations are the greatest. The FOV in the horizontal direction spans from $x/a = 0.1$ to $x/a = 0.85$, enabling the capturing of the main SWBLI features. To minimise the laser reflections, the panels were painted completely black. Moreover, the window on the opposite side and parts of the lower Mach block just up- and downstream of the panel were covered with a black adhesive film, minimising reflections from other parts of the wind tunnel environment. A summary of all the chosen PIV parameters, as discussed above, is shown in Table 3.6.

Table 3.6: Measurement parameters used during the DIC test campaign

Parameters	**Value**
Camera	Photron FASTCAM Mini AX100
Resolution (full)	1024×1024
Resolution (used)	1024×480
Pixel size	$20\,\mu$m $\times$ $20\,\mu$m
Acquisition frequency	4000 Hz
Acquisition time	2.9 s
Lens	Nikon 60 mm
$f_\#$	5.6
Magnification factor	0.19
Spatial resolution	9.50 px/mm
Depth of field	3.16 mm
Laser model	Quantronix Darwin-Duo 527-80-M
Laser wavelength	527 nm
Laser thickness	1.5 mm
Pulse separation	$2.85\,\mu$s
Laser current high-power mode	26.0 A
Seeding generator	PIVTEC Aerosol Generator PivPart 45
Seeding nozzles used	36
Particle type	Di-Ethyl-Hexyl-Sebacat (DEHS)

3.9 Uncertainty Analysis

Measurement through experimental techniques always come with a certain degree of imprecision and uncertainty. The aim of this section is therefore to perform an uncertainty analysis on the DIC and PIV measurements, as these are the main quantitative experimental techniques used in the current study.

The first type of uncertainty is the one related to random fluctuations present in the measurement environment. This can extend from the measurement system itself to other sources around the system. These random variations can easily be filtered out by taking a large sample size. Hence, this statistical uncertainty is related to the mean measured quantities, such as the mean surface displacement for DIC and the mean flow velocity components for PIV. This uncertainty can be calculated as

$$\epsilon = \frac{\sigma}{\sqrt{N}}, \tag{3.14}$$

where σ is the standard deviation of the measurement and N the number of uncorrelated samples. Thus, the higher the number of samples, the lower the statistical uncertainty becomes. For the DIC experiments, $N_{DIC} = 10{,}000$, while for PIV the used number of samples for analysis is $N_{PIV} = 8{,}000$. The statistical uncertainty for both experiments can be found in Table 3.7 at the end of this section. Note that the value presented here is taken in the region upstream of the SWBLI, where the flow can be assumed to be steady, such that the statistical error can be related as much as possible to the accuracy of the measurement system and the wind tunnel noise. In addition to this, Equation 3.14 provides an underestimation of the actual statistical uncertainty as the N images are not all uncorrelated.

Another source of uncertainty is the one related to the cross-correlation operation. For planar PIV, this has been found to be around $\epsilon_{corr} = 0.1$ px (Raffel et al., 2018) and can be calculated as (Humble et al., 2009):

$$\epsilon_{cc} = \frac{\epsilon_{corr}}{k\delta_t}, \tag{3.15}$$

where k is the spatial resolution of the image and δ_t the pulse separation time of the laser. These quantities for all PIV experiments are given in Table 3.6, while the uncertainty due to the cross-correlation operation for planar PIV can be found in Table 3.7.

As introduced in the working principle for PIV in section 3.8, PIV is based on particles following the flow well enough, such that the illuminated particles can be used as a measure for the flow field. However, especially for high speed flows, the response time of the particles can be quite different from the characteristic time scale of the flow. The slip velocity that results from this difference is an additional source of uncertainty, which can be estimated through (Melling, 1997):

$$\epsilon_{slip} = \vec{U}_{slip} \approx \tau_p \cdot \vec{a}_p, \tag{3.16}$$

where τ_p is the particle response time of the DEHS particles, estimated by Ragni et al. (2011) to be around $\tau_p = 2$ μs, and $\vec{a}_p$ the particle acceleration. Assuming the flow to be steady, this acceleration can be estimated through (Sun, 2014):

$$\vec{a}_p = \vec{U} \cdot \nabla \vec{U}. \tag{3.17}$$

Combining both Equation 3.16 and Equation 3.17 results in the following expression for a two-dimensional flow field:

$$\epsilon_{slip} = \vec{U}_{slip} \approx \tau_p \vec{U} \left(\frac{\partial u}{\partial x} + \frac{\partial v}{\partial y} \right). \tag{3.18}$$

From Equation 3.18 it can be predicted that the slip velocity would be the highest through shock waves, as there the velocity gradients are the strongest (Ragni et al., 2011). The value for this slip velocity uncertainty is given in Table 3.7.

Finally, for the DIC, there is another source of error introduces within the measurement system, which is a systematic error. This error is introduced both by possible imprecision in the calibration procedure, as well as due to the aberration effect as a consequence of the shock waves present in the flow, causing large density gradients. This error is identified through the visualisation of the mean rigid plate deformation. As this panel should not show any deformations, any identified deformation is assumed to be a source of error, also present in other measurements. This mean deformation of the rigid panel is shown in Figure 3.27.

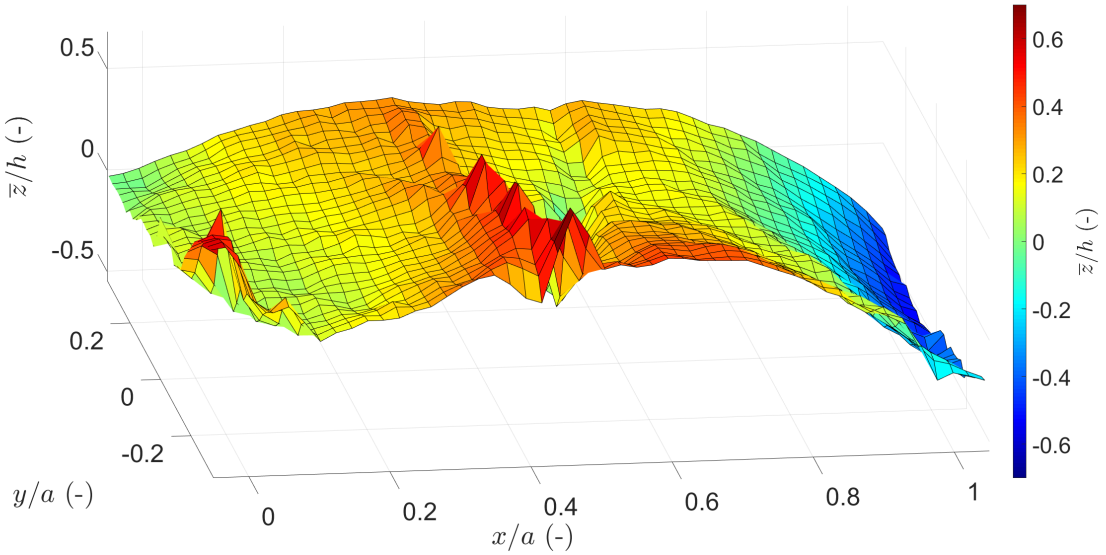

Figure 3.27: Mean surface deformation of rigid panel.

Note how towards the trailing edge, the deformation is mainly downward. As the location from which this deformations starts corresponds to the SWBLI structure, this is mainly attributed to the change in density through the test section, and thus also captured in this way by the cameras. Again, as this error is assumed to be present in all DIC measurements, it is believed that the overall error in the measurements is reduced by subtracted the mean of the rigid deformation.

Table 3.7: Summary of uncertainty values from different sources for DIC and PIV experiments.

Uncertainty Source	Rigid	Open	Ventilated	Closed	RD
Statistical ϵ_u (PIV)	$< 0.10\,\mathrm{m/s}$	$< 0.13\,\mathrm{m/s}$	$< 0.16\,\mathrm{m/s}$	$< 0.07\,\mathrm{m/s}$	$< 0.09\,\mathrm{m/s}$
Statistical ϵ_v (PIV)	$< 0.07\,\mathrm{m/s}$	$< 0.09\,\mathrm{m/s}$	$< 0.13\,\mathrm{m/s}$	$< 0.08\,\mathrm{m/s}$	$< 0.08\,\mathrm{m/s}$
Statistical ϵ_z (DIC)	$< 3.5 \times 10^{-10}\,\mathrm{mm}$	-			
Cross-correlation ϵ_{cc} (PIV)	$< 3.69\,\mathrm{m/s}$				
Particle slip ϵ_{slip} (PIV)	$< 64\,\mathrm{m/s}$	$< 54\,\mathrm{m/s}$	$< 88\,\mathrm{m/s}$	$< 71\,\mathrm{m/s}$	$< 66\,\mathrm{m/s}$
Resolution subset (DIC)	$< 5.69\,\mathrm{m/s}$				-
Resolution interrogation window (PIV)	$< 2.52\,\mathrm{m/s}$				

4

Processing Techniques

In order to extract information from experimental data, it is often not enough to only use the raw data; some processing is needed to extract the specific information needed for the research objective. The aim of this chapter is to present the different processing techniques used in the current research. These techniques are divided in three different categories: First of all, some pre-processing techniques are discussed in section 4.1, needed to prepare the data for the actual processing. The processing techniques used to extract the structural and flow field information from raw measurement images is then explained in section 4.2. Finally, the post-processing techniques implemented to extract relevant properties from the measured quantities are presented in section 4.3.

4.1 Pre-Processing

Before applying any processing procedure, it is sometimes needed to process the data beforehand. The aim of this section is to present these pre-processing techniques, relevant to specific data from particular measurement techniques. The pre-processing procedures for the DIC and PIV images are presented in subsection 4.1.1, while the ones for infrared imaging data is presented in subsection 4.1.2.

4.1.1 DIC and PIV Image Pre-Processing

Once the raw images are obtained, some pre-processing is needed before the displacement or velocity fields can be computed. For the PIV images, this is mainly needed to reduce the effect of the laser reflections on the surface and other parts inside the wind tunnel. To prevent these reflections as much as possible in the first place, the panel surfaces were sprayed with black paint and the opposite wind tunnel window was covered with black tape. The operation used inside the software to reduce the reflections is a minimum time filter subtraction with a specific filter length. This filter length was specified to be 11 images. The effect of this time filter on raw PIV images is shown in Figure 4.1.

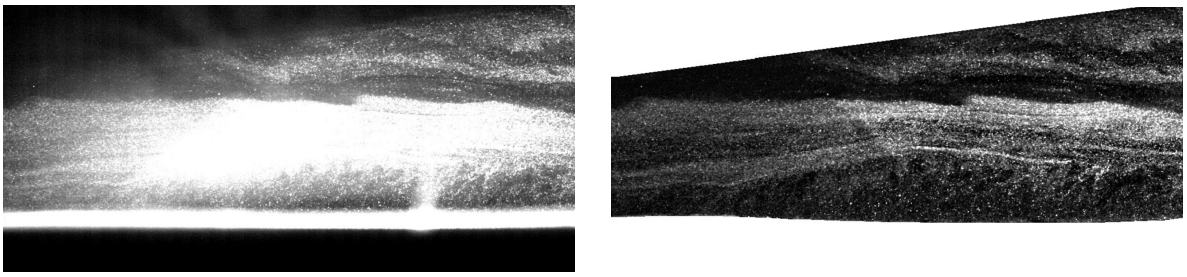

(a) Raw PIV image

(b) Pre-processed image

Figure 4.1: PIV pre-processing of raw image with time filter subtraction and mask operations.

Note how in Figure 4.1 not only the reflection of the laser has reduced significantly, but also that part of the image is cut away. This mask operation is needed as not all parts of the image are (well) illuminated by the laser sheet or seeded with particles. Eliminating these parts before the computation of the displacement or velocity field prevents obtaining parts were the computation of these fields would

fail. This is especially important for parts close to the FOV of interest, as those could be affected by the failing image processing procedures. While this masking operation is more trivial for the DIC images, another step is needed for the PIV images. This is because of the up-and-down movement of the panel, and therefore also of the laser reflection. Hence, first the maximum filter was used to estimate the highest panel position over the whole acquisition time. The mask is then taken from this position such that the masked FOV never contains part of the panel, thus preventing any failing cross-correlations.

4.1.2 Image Intensity to Temperature Mapping

The infrared images are recorded using the Optris imager software. From this program, the temperature can not be exported directly. Therefore, a particular procedure had to be employed to extract the temperature from the RAVI files created by the Optris software. From these files, the pixel intensity is obtained for every frame. It is, however, possible to export another separate file from the software containing the minimum and maximum temperature in each frame. With this information, the pixel with the lowest intensity in each frame can be related to the lowest temperature in the frame, and in the same way the pixel with the highest intensity to the highest temperature. Subsequently, the intensities with values in between the minimum and maximum can be related to a physical temperature by means of linear interpolation.

As the images are taken at an angle with respect to the surface, a perspective transform is employed to visualise the images as if they were taken directly above the panel. Although this procedure introduces some stretching, the qualitative information is deemed sufficient enough for the purpose in the current research. In *Python*, the transformation matrix can be computed using *getPerspectiveTransform* from the *cv2* library. To compute this matrix, the function needs some coordinates from the original image and coordinates in the new transformed space. With both procedures above, temperature data can be extracted from each frame at physical panel locations.

4.2 Image Data Processing

For the recording and computation of the out-of-plane displacement field and the flow field, the software DaVis of LaVision was used. In this section, details are given on the parameters used as an input to the computation algorithms. A brief explanation of these algorithms is given for both DIC and PIV, in subsection 4.2.1 and subsection 4.2.2 respectively.

4.2.1 DIC Least-Squares Method

For the DIC data, an in-built least-squares method (LSM) is used to find a correspondence between the images from the two cameras. So-called 'seeding points' are defined in the first frame, after which, based on the calibration, the software tries to fit a least-square solution in the second frame, within a certain threshold for the correlation value. From these seeding points, the program grows the computation of the displacement field over the whole masked FOV. However, the way the program accepts correct seeding points seems a bit arbitrary, thus these seeding points need to be found by trial-and-error. Using the 'user defined' calculation mode, the threshold for the correlation value can be relaxed, making it easier for the program to find a correspondence or making the program search for correspondence in a larger area.

The subset size for the computation of the displacement field was chosen to be 29x29 px, with a step size of 17 px (overlap of $\approx 41\%$). The correlation method was based on the 'relative to first' method, which tries to find a match between the instantaneous image and the first image in the set. This first image was set to be the average of 100 images taken at 'wind-off' conditions. Points in the filed which contain less than 75% (by default) of valid vectors were automatically discarded by the program.

4.2.2 PIV Cross-Correlation

For the PIV data, the in-built PIV processing method in DaVis is used. Similar to DIC, a cross-correlation value is computed between two frames within a certain area to find the value of the velocity vector in that area; these areas are called interrogation windows (rather than subsets, used in DIC). A multipass algorithm was used, which starts with a large square window in which an initial estimate for the velocity vector is computed. Using a larger window for the initial passes allows for correctly resolving particles with large pixel displacements. In the subsequent passes, the windows are shifted by the displacement obtained in the previous pass, after which the cross-correlation is computed again. After a particular number of passes, the algorithm switches for smaller, circular windows for higher accuracy and spatial resolution. The first passes are computed using a 96x96 px interrogation window, after which three to four final passes are done with a circular window of 32x32 px. For all passes, an overlap of 75% was used. In addition to this, in the ”Image preprocessing” settings, the ”Subtract sld. background” length is set to 40, while the ”Min/max filter” length is set to 5. No outlier detection method was used during the process itself. Only after obtaining the computed fields, an attempt was made to remove outliers using available *MATLAB* codes. This method is explained in subsection 4.3.1. A concise summary of the used settings for both PIV and DIC is shown in Table 4.1.

Table 4.1: Processing paramaters for DIC and PIV

Parameter	DIC	PIV
Window size	29x29 px	96x96 px -> 32x32 px
Overlap	41%	75%
Image pre-processing	Mask	Mask + Time filter subtraction (11 images)

4.3 Post-Processing

After the data is pre-processed and then processed, sometimes it is still difficult to extract relevant information from the data which can reveal interesting properties of the structure or the flow. That is why some post-processing techniques can be used to reveal those properties. The aim of this section is to introduce the ones used in this study. Before any processing, an outlier detection is employed for the PIV images, which is briefly explained in subsection 4.3.1. In subsection 4.3.2, the spectral analysis method is introduced, where it is shown how the power spectral density of a signal in time can be computed. After that, subsection 4.3.3 shows the concept of phase averaging, while subsection 4.3.4 continues with explaining the proper orthogonal decomposition, and in particular the method of snapshots. Finally, the algorithm to detect the reflected shock wave, how it is projected onto the surface and how to extract a measure of its motion is described in subsection 4.3.5.

4.3.1 Outlier Detection

When doing data analysis, it is undesirable to have too many outliers in the data, as this increases the noise in the data and makes it harder for particular techniques to obtain reliable data. That is why a first step in the post-processing is to correct or eliminate as many outliers as possible. The implemented procedure mostly relies on discarding vectors of which the values do not lie within ± 3 standard deviations with respect to the average velocity value of the components. The outliers are then substituted with an interpolated value of neighbouring values (D'Aguanno, 2023). Once this outlier detection has been implemented, the data is ready to be used for other data analysis procedures.

Another way in which an outlier detection method is used, is when computing the statistical quantities of the flow fields. This is done in an iterative way where first for every frame, it is checked whether each vector is valid or not, based on a certain threshold. Similar to what is described above, this criterion is based on whether or not the vector value lies within ± 3 standard deviations with respect to the average

value of that vector in time. Note that this average value is updated during the iterative process, together with the values for the standard deviations. Once the solution is converged, the statistical quantities are saved and can be presented or used for other computations.

4.3.2 Signal Spectral Analysis

In the current study, spectral analysis is applied on several sort of signals to describe differences in unsteady phenomena between different cases. In particular, it helps to characterise the (dominant) frequencies that make up these phenomena and how they differ from case to case. To transform a time signal to the frequency domain, the Fourier transform can be used to decompose the time signal as a sum of weighted sinusoidal waves in the frequency domain. This transform is given as

$$X(f) = \int_{-\infty}^{\infty} x_n(t) e^{-i2\pi ft} dt, \tag{4.1}$$

where x_n is the time signal to be transformed to the frequency domain. However, as the data is not a continuous function of time, but rather, due to the acquisition of N samples, a discrete one. Therefore, Equation 4.1 can be written in a discrete form as

$$X_k = \sum_{n=0}^{N=1} x_n e^{\frac{-i2\pi kn}{N}}, \tag{4.2}$$

where N is the number of acquired discrete samples at a constant rate. Because of the noise and random effects contained within the signal, the discrete Fourier transform (DFT) does not suffice, but rather the power spectral density (PSD) of the signal can be computed. The PSD is a representation of how the total power of the signal is distributed across the frequencies. The PSD for a finite number of samples can be represented as follows using a periodogram function (Solomon Jr, 1991):

$$P(f) = \frac{1}{N} \left| \sum_{n-1}^{N} x_w(n) e^{-i2\pi fn} \right|^2, \tag{4.3}$$

where $x_w(n) = w(n)x(n)$ represents the windowed sample $x(n)$ with a certain window function $w(n)$. In the current study, the periodogram is computed using Welch's method (Welch, 1967), which is a method that can be used to reduce the effect of noise in a signal. However, it comes at the cost of frequency resolution in spectral space. The way Welch's method works is by dividing the original signal in L overlapping segments, which are each windowed in the time domain. A Fast Fourier Transform is then computed on each of these segments separately, after which the square of the amplitude is taken, such that the periodogram $P_j(f)$ of each segment is contained. The final PSD by Welch's method is then computed by taking the average of all the individually computed periodograms as:

$$P(f) = \frac{1}{L} \sum_{j=1}^{L} P_j(f). \tag{4.4}$$

In practice, the PSD is computed using the *MATLAB* function *pwelch*, which uses 8 segments of equal length with an overlap of 50%. By pre-multiplying the PSD with the frequency, an estimate of the proportional energy at each frequency value is provided of the signal.

4.3.3 Phase Averaging

When performing averages over time of either structural or fluid motion, the dynamic behaviour of these elements in time is lost. In particular if a motion is periodic, the particular phases of the motion might be of interest. With the phase-averaging procedure it is possible to retrieve the average periodic motion with respect to the mean by dividing the motion into a particular number of phases. In the case

of shock-induced panel flutter, four distinct phases are recognised for the panel motion, where phase 1 is the point when the panel is at its maximum position and phase 3 the point when it is at its minimum. Phase 2 and 4 are those in between the aforementioned phases.

In the current study, the algorithm used to identify the different phase of the panel motion makes use of the *MATLAB* function *findpeaks*, where either a minimum or maximum is found. If the frequency of the periodic motion is known, the program can be told to find the next minimum or maximum only after a certain number of samples. This is especially needed when the motion contains strong higher frequency contributions. Outlier detection procedures are then used to identify whether points are identified to be in the correct phase. Once all the points are divided among the four phases, the average of all the points in each phase can be computed, with the number of points in each phase respectively. With this, a phase-averaged representation of a motion of interest is obtained.

4.3.4 POD Analysis

Another way to represent motion dynamics in time is using proper orthogonal decomposition (POD), which extracts the most energetic modes of the motion and orders them in that way. This way, the displacement or flow field can be represented by a number of modes which contain sufficient energy, such that the order is reduced. In other words, it can be used as a form of data compression. For this study however, it is of interest to extract the most energetic modes from the POD, such that characteristic structures can be identified. Considering the out-of-plane displacement of the panel $z(\vec{x}, t)$ as a function of space and time, it can be decomposed as

$$z(\vec{x}, t) = z_{avg}(\vec{x}) + z'(\vec{x}, t) = z_{avg}(\vec{x}) + \sum_{j=1}^{M} a_j(t)\phi_j(\vec{x}), \tag{4.5}$$

where $a_j(t)$ and $\phi_j(\vec{x})$ are the temporal and spatial POD modes respectively and M the total number of modes. Thus, the fluctuations of the displacements are decomposed as separate functions of space and time. As M approaches the total number of frames, Equation 4.5 approaches the exact solution. The current study makes use of the "Method of Snapshots" (Sirovich, 1967), where the data is collected inside a $N_x \times N_t$ matrix, where N_x and N_t are the number of points in space and instances in time respectively. With this snapshots matrix U, the time coefficient matrix C can be constructed as

$$C = \frac{1}{N_t} U U^T. \tag{4.6}$$

Solving the eigenvalue problem of this matrix results in finding the orthogonal decomposition of U, while also extracting the energetic modes (Aranyi et al., 2013). In other words: solving the eigenvalue problem of C results in finding the time coefficients matrix A and the eigenvalues λ_j, ordered by their energy, and thus also the spatial functions, ϕ. The spatial functions are computed as:

$$\phi = U^T A, \tag{4.7}$$

With these spatial functions, the spatial modes can be computed as:

$$U_{mode}(j) = \sqrt{\lambda(j)} \cdot \phi_j(\vec{x}), \tag{4.8}$$

where, as expected, the modes in U_{mode} are orthogonal to one another. As the spatial do not change in time, the reduced order reconstruction of the panel motion in time is driven by the temporal mode functions. Combining the procedure above, Equation 4.5 can be rewritten as:

$$z(\vec{x}, t) = z_{avg}(\vec{x}) + \sqrt{N_t} \sum_{j=1}^{M} \sqrt{\lambda_j} \cdot a_j(t) \cdot \phi_j(\vec{x}) \tag{4.9}$$

4.3.5 Shock Projection and Motion

Past studies have shown that the location and motion of the reflected shock wave are out of great interest to get a fundamental understanding of the underlying mechanism of the SWBLI. That is why in the post-processing of the PIV data, attention is given to shock tracking operations. A method to detect the reflect shock wave is by taking the derivative of the vertical velocity in the x-direction, $\frac{dv}{dy}$, as its change is larger through the shock wave than the jump in horizontal velocity. At a particular vertical location, the highest value for $\frac{dv}{dy}$ then is taken as the instantaneous location of the reflected shock. This can also be done on the computed average flow field, such that the average shock location is found directly from this. If this procedure is repeated for several z-locations in the average or instantaneous flow field, a linear regression fit can be used to project the reflected shock onto the surface, such that a location of the shock foot is computed. In *MATLAB*, this is done through the function *polyfit*. For the average flow field, this is rather trivial and the projected shock foot can be found easily. This is shown in Figure 4.2. However, for the instantaneous images, the resulting signal in time is found to be rather noisy, thus being impractical for a proper spectral signal analysis.

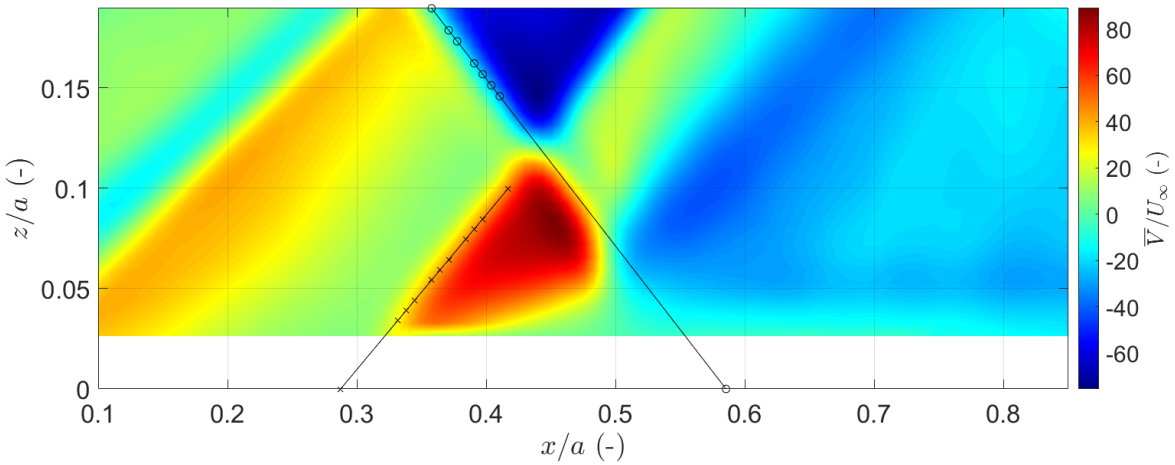

Figure 4.2: Impinging and reflected shock wave projection onto the panel surface at $z = 0$.

For performing a spectral analysis on the reflected shock motion, the same principle is used, where the highest value for $\frac{dv}{dy}$ is taken as the reflected shock position, with the difference that for the tracking in time, instantaneous flow fields are used instead of the average one.

5

Wind Tunnel Boundary Conditions Effects on Panel Deformation

The aim of this chapter is to dive into the dynamics of the (thin) panel oscillations, and simultaneously gain a deeper understanding of the wind tunnel boundary conditions. This is done by firstly analyse how the confined wind tunnel test section may influence the flow over the panel (see section 5.1). After that, in section 5.2 the cavity closure condition is addressed, while at the same time diving deeper into the different aspects of the panel motion. Finally, in section 5.3 the temperature development of the panel is documented and its impact on the panel motion is discussed.

5.1 Wind Tunnel Confinement Effect

One of the limitations of wind tunnel testing is the presence of walls, confining the air to flow within set solid boundaries. In Figure 2.5 it was shown that not only the walls have an effect, but also the presence of a shock generator, and in particular the gap between it and the walls, results in a three-dimensional effect. This section aims to address the resulting confinement effects as a consequence of testing in a bounded environment. Firstly, subsection 5.1.1 looks at these effects in the absence of a shock generator, and, therefore, in the absence of shock waves. Then, subsection 5.1.2 analyses the effect after including the shock generator.

5.1.1 No Shock Generator

In this subsection, the case without a shock generator is considered, making it possible to isolate the effect of the shock generator and the impinging shock from the interaction the flow has by itself with the bounded environment. To achieve this, OFV is used, which allows for the qualitative study of these effects across the entire surface of the panel. The results of the OFV experiments are presented in Figure 5.1 for a rigid and thin, flexible panel. On the right of Figure 5.1, some relevant conditions are represented to aid in the analysis of the results. This includes whether the cavity was closed or not, and consequently what the cavity pressure was. Furthermore, by inspection of the video made during the experiments, an approximate representation of the mean deformation of the panel is included.

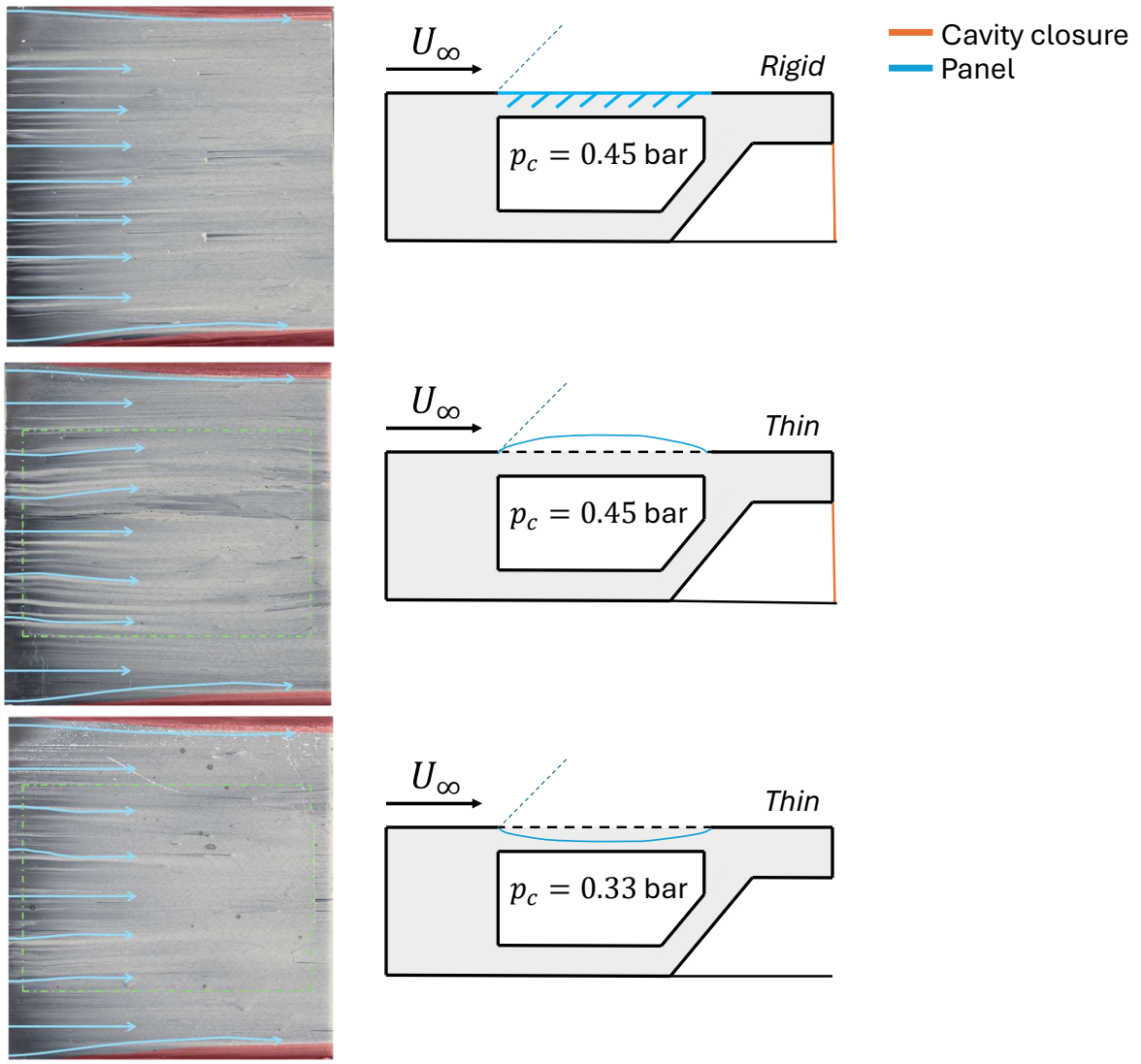

Figure 5.1: Oil flow visualisation on a rigid (upper case) and thin, flexible panel (centre and lower cases) without a shock generator, together with a schematic representation of the wind tunnel and panel conditions during the run.

A direct effect of the wind tunnel confinement can be observed in the upper case (rigid plate) shown in Figure 5.1: at the edges of the panel (i.e. at the wall), some corner separation flow seems to develop. As there is no shock generator present, this is not due to the interaction between the impinging or reflected shock and the wall. Instead, as it starts at the leading edge of the panel, this might be due to the interaction between the wall and Mach waves created by the small step between the clamping piece and the panel. This flow near the wall, however, has a negligible effect on the middle part of the panel, which corresponds to the portion that is made thin in the case of the thin panel. Rather, by inspection of the OFV results of this latter panel, the streamlines at the surface seem to be curved as a consequence of the deformation of the panel, and not because of any confinement effects; due to a deflection upwards, the streamlines are diverted outwards, while a downwards deflection acts as a sort of ”sink” and diverts the streamlines inwards. The cause of the different deformations is the difference in cavity pressure. The explanation of this is out of the scope of the current section and is treated in more detail in section 5.2. Nevertheless, it is noted that for the rigid panel, the cavity pressure has no effect, as it does not deform at all. The case where the cavity was left open is not included in Figure 5.1 but results in the exact same flow pattern as shown for the rigid case shown in the figure.

5.1.2 With Shock Generator

The previous subsection showed that rather than the presence of the walls, it is the deformation of the plate that seems to have the greatest impact on the streamline pattern at its surface. This changes when a shock generator is placed inside the wind tunnel, and, as a consequence, the SWBLI structure with shock and expansion waves start to form. As these are strong flow phenomena, the interaction between these waves and the wall is also stronger compared to the case without a shock generator. The effect this has on the flow pattern at the surface of the panel is shown in Figure 5.2.

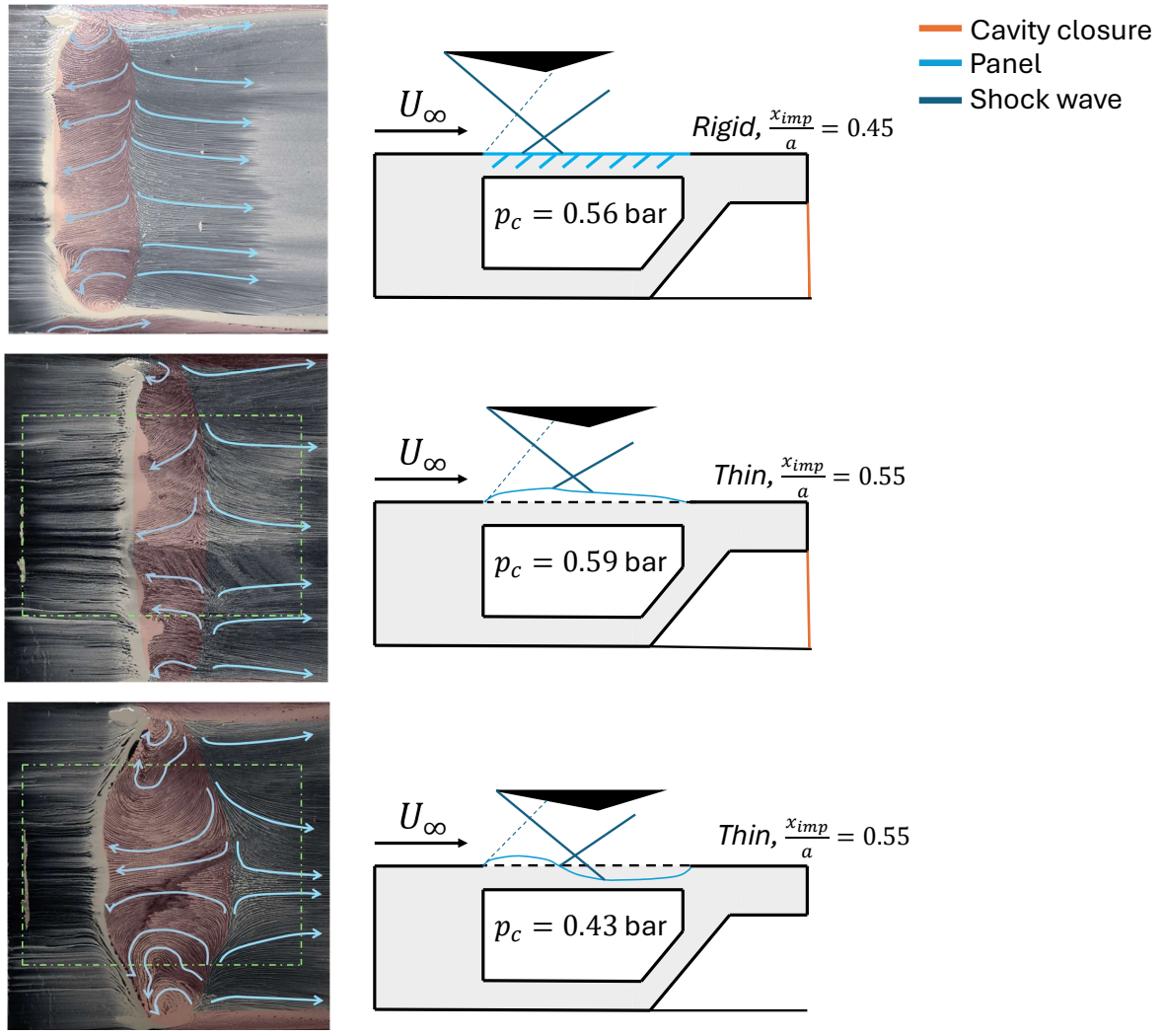

Figure 5.2: Oil flow visualisation on a rigid (upper case) and thin, flexible panel (centre and lower cases) with a 12° shock generator, together with a schematic representation of the wind tunnel and panel conditions during the run.

Firstly, note that the rigid plate OFV experiment has been done at an impingement location $\frac{x_{imp}}{a} = 0.45$, compared to the thin panels which have been tested with $\frac{x_{imp}}{a} = 0.55$. This however has no effect on the comparison between the cases, as for a rigid flat plate it does not matter where the inviscid impingement location is located; the SWBLI will look the same, but simply shifted. This shift can be observed by the location of the separation region, which can be identified by the direction of the streaklines: in the separation region, reverse flow is present, causing the lines to go the opposite way with respect to the main flow. For clarification, the direction of the flow has been visualised with arrows. Keeping the focus on the rigid case, it can be observed that along the span of the plate, the separation region is of varying length. This is, as mentioned before, due to the interaction between the shock waves and

the wall. The surface pattern due to the SWBLI structure is as expected from the discussion in subsection 2.1.1. Firstly, this can be seen from the corner separation at the wall. Secondly, distinct ”foci” can be observed at the edges of the separation region, near the wall. These foci are characterised by spiralling flow due to the back-flow inside the bubble interacting with the flow upstream of the separation region at its edge (Xiang & Babinsky, 2019). The corner vortex that forms can also be observed by inspection of the wind tunnel windows at the end of the run.

Similar to the discussion without a shock generator, experiments performed with a thin panel are presented; an experiment was done with the cavity closed (centre) and another one with the cavity opened (bottom). By a first comparison between these two cases, it becomes quickly evident that the separation length is significantly different, as well as different to the rigid panel case. Tripathi et al. (2021) explains that the mechanism behind these differences is associated with the difference in surface curvature: the curvature induces a pressure gradient and therefore can either reduce or increase separation. It was found that a positive curvature (i.e. into the flow) reduced separation, and a negative curvature increases it. The results in Figure 5.2 are in agreement with this as for the centre case, the upward curvature results in a decreased separation length with respect to the rigid case. Similarly, a (largely) downward deflection, as shown in the bottom case, results in an increased separation length. Again, a discussion on the deformation shapes, shown schematically, as a result of the cavity pressure is left for further discussion in section 5.2.

The results presented in Figure 5.2 show that the obtained results are in agreement with literature, and that in the presence of a shock wave the confinement effects due to testing inside a wind tunnel can cause the SBWLI structure to become three-dimensional across the span of the panel. This is due to the shock waves interacting with the sidewalls. Furthermore, it has been confirmed that the deformation shape of the panel also plays a significant role into the size of the separation region.

5.2 Cavity Closure Effect

One of the drivers behind the current study is the understanding of the cavity condition. As already hinted towards in section 5.1, the cavity closure has a significant effect on the panel deformation, and possibly on other aspects of the panel behaviour. This section aims to address these different aspects and develop a greater understanding of the cavity closure effect on the deformation and oscillation of the panel.

5.2.1 Cavity Pressure and Deformation

As was shown already in Figure 3.4, in the open-cavity case, downstream of the test section, the flow is able to flow back, into the cavity. Schlieren experiments also confirmed this and clearly shows the presence of (strong) pressure waves flowing into the cavity. These waves were also detected by Aditya (2022), who established that the frequency of these waves was inherent to the waves themselves inside the open cavity rather than the flutter of the flexible panel. Furthermore, the flutter frequency seemed to exhibit resonance with respect to the cavity waves. That is why, in an attempt to eliminate the resonance, the cavity was closed as shown in Figure 3.5. An example of an instantaneous schlieren image is shown in Figure 5.3. This image also contains the location of a digital probe; this probe is used to analyse the spectral content of the waves entering the cavity.

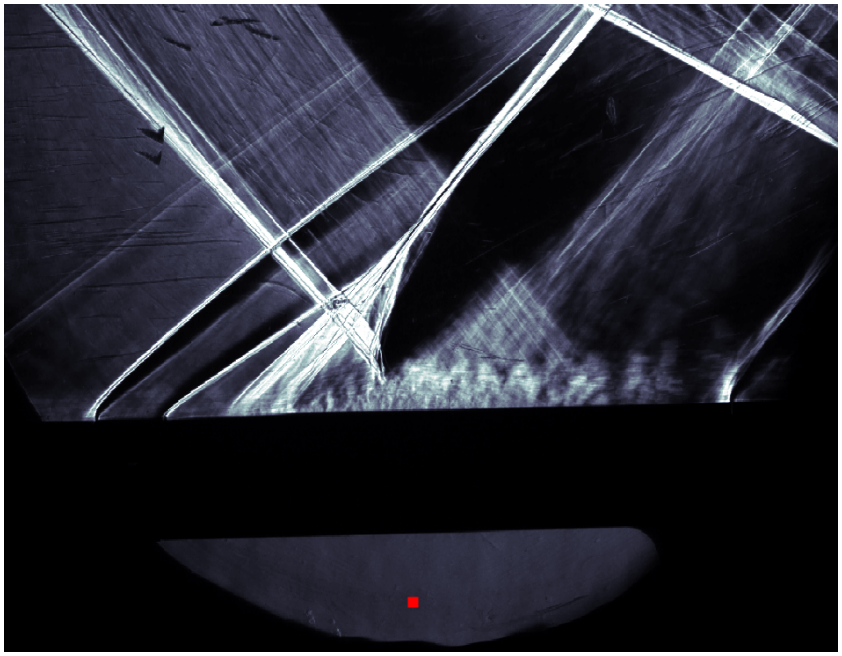

Figure 5.3: Schlieren image for the open-cavity case with the location of digital probe for computation of the PSD of cavity pressure waves.

In Figure 5.4 the PSD of a digital probe inside the cavity is presented, obtained from schlieren imaging, showing the difference in energy between waves present in the open- and closed-cavity case at different frequencies.

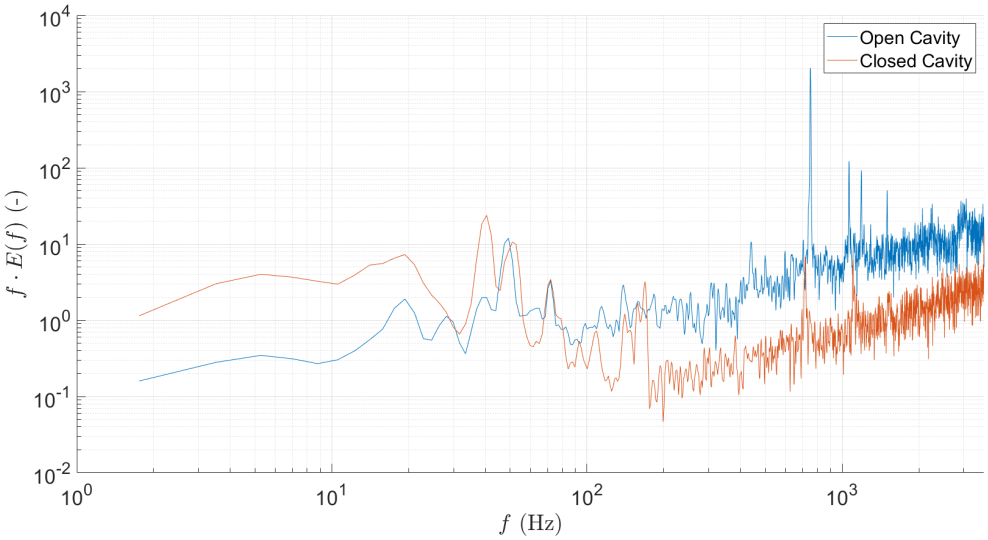

Figure 5.4: Pre-multiplied PSD of signal obtained from digital schlieren probe inside the cavity.

Figure 5.4 shows that when the cavity is open, there is a dominant frequency at $f \approx 750\,\text{Hz}$. In contrast, closing off the cavity lowers the energy at these frequencies drastically. An intermediate cavity closure case was chosen, as shown in the centre of Figure 3.5, where the cavity would not allow for these strong waves to enter the cavity, but where the small holes would pressurise the cavity in the same way as the open-cavity case. Although no schlieren experiments were done for this case, it is expected that, similar to the closed-cavity case, there are no dominant high-energy frequencies present inside the cavity.

During all the experiment, pressure data was collected from inside the cavity. As seen already in section 5.1, the cavity pressure has a large influence on the deformation of the panel. This is in accordance with the literature, as presented in subsection 2.2.4. When the cavity is closed, the pressure inside it remains higher (closer to atmospheric pressure) with respect to the open cavity case. In the latter case, the pressure equalises itself to the flow pressure downstream of the test section. This argument also holds for the closed-open case, where the air in the cavity is still connected with the flow downstream of the test section because of the nine holes in the cavity plate. The difference in cavity pressure leads to a difference in loads across the panel, thus resulting in a different mean deformation, as shown in Figure 5.5.

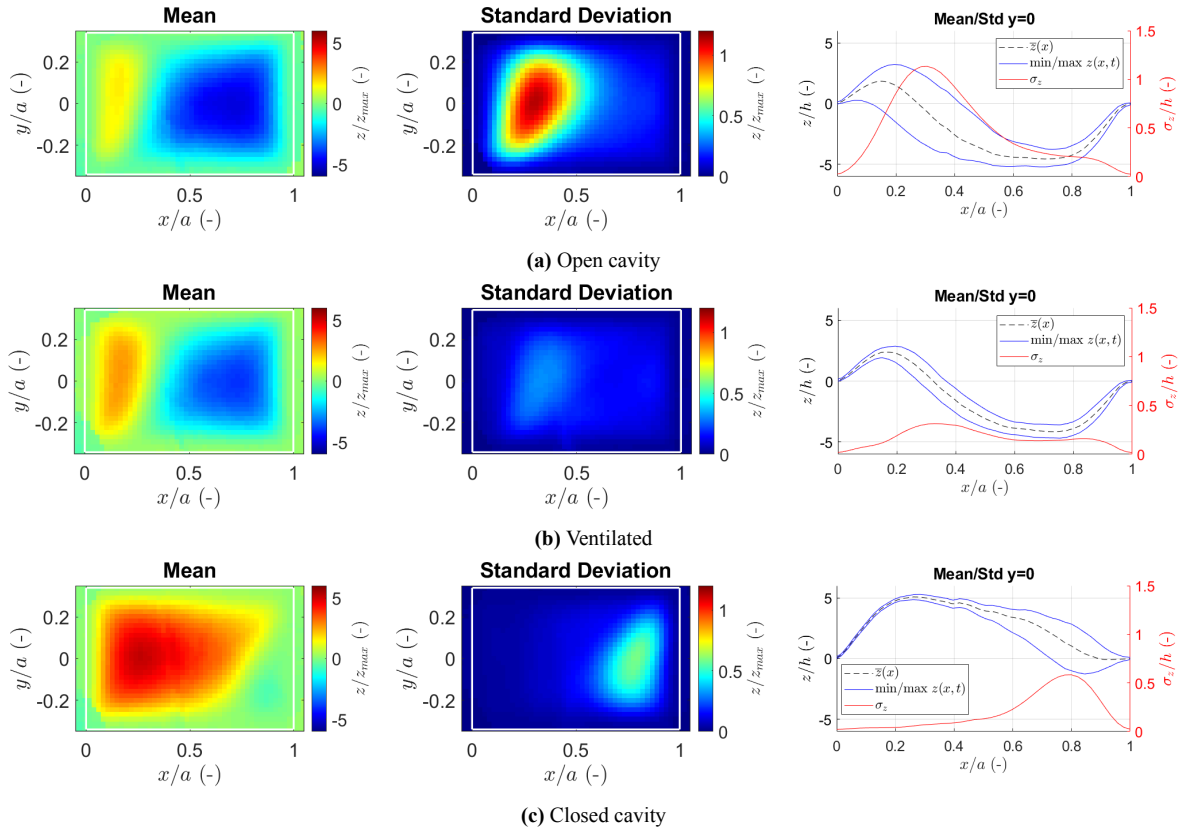

(a) Open cavity

(b) Ventilated

(c) Closed cavity

Figure 5.5: Mean (left) and standard deviation (centre) of panel oscillations over its full thin portion and along the centre-line (right) at $y/a = 0$.

The open-cavity case, as seen in Figure 5.5a, starts with a positive deformation, as the cavity pressure is higher than the freestream pressure. Once the flow has passed the shock, where the pressure is increased, the pressure on top of the panel is higher than the cavity pressure, resulting in a downward deformation. A similar behaviour is observed for the closed-open-cavity case, as p_c is very similar to the open-cavity case. In contrast to this, the closed-cavity case exhibits a fully upward deformation, as the cavity pressure is always higher than the flow pressure on top of the panel. A direct comparison of only the mean deformation of the three cases is provided in Figure 5.6, where the mentioned cavity pressure influence is clearly visible. These deformation shapes, in combination with the differences in cavity pressure, are in accordance with literature, such as the numerical simulations performed by Visbal (2014), which show the changes in deformation shapes as a function of cavity pressure (see Figure 2.17)

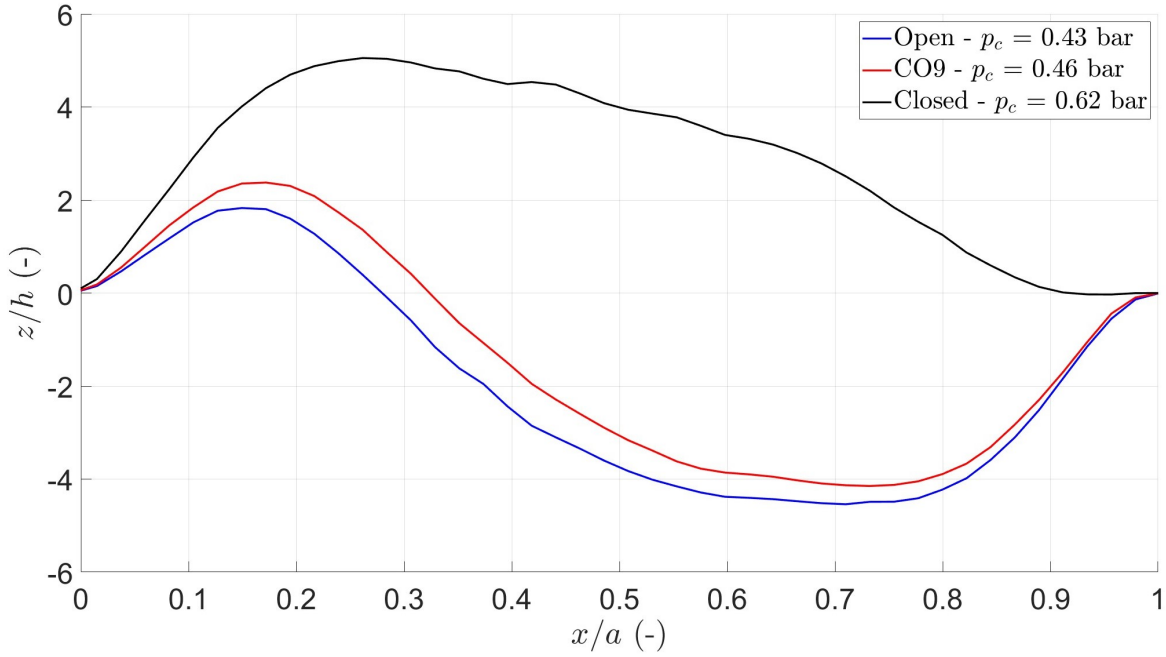

Figure 5.6: Comparison in mean deformation taken at the spanwise location with the highest standard deviation between panels with a different cavity pressure.

Also shown in Figure 5.5 is the standard deviation of the fluctuations across the entire panel. Compared to the plots on the right of the figure, the standard deviation can be seen as a measure of how wide the envelope of the oscillation is. In other words: the higher the standard deviation, the larger the oscillation amplitude is in that particular point. For the open- and closed-open-cavity cases, the standard deviation can be found in the first half of the panel, which also corresponds to where the oscillation of the separation shock foot can be found. However, for the closed-open case, the standard deviation is significantly lower. This is partially due to the fact that there are no waves coming into the cavity, which drive the panel motion, as hypothesised by previous research (Aditya, 2022; Allerhand, 2020; Mathijssen, 2022). In addition to this, without waves driving the motion and assuming the motion now exhibits free flutter, the ratio of freestream and cavity pressure is not high enough for the panel to exceed the flutter limit ($z'/h > 1$), as can be seen from Figure 5.7. An attempt was made to higher the total pressure of the flow, but as the cavity pressure rises with it, wanting to create an equilibrium out of itself, the flutter boundary cannot be fully reached. Nonetheless, as will be analysed in the next subsections, the panel exhibits interesting oscillatory behaviour. Finally, in the closed-cavity case, the standard deviation reaches its peak more towards the TE of the panel. In the first half, the cavity pressure is much larger than the freestream pressure, and therefore it is as the panel is stiffened by the load difference. However, at the aft part of the panel, this pressure difference is not as large anymore, such that the flutter boundary is exceeded and the panel displays some oscillatory behaviour there. The value and location of the the maximum standard deviation of the oscillation for each panel is summarised in Table 5.1 at the end of this subsection. From this table it can be seen that the y-location of the point of maximum standard deviation is at the mid-span or very close to the mid-span location along the panel. Hence, in subsequent discussion, the mid-span location is considered to also represent the location with the largest oscillations.

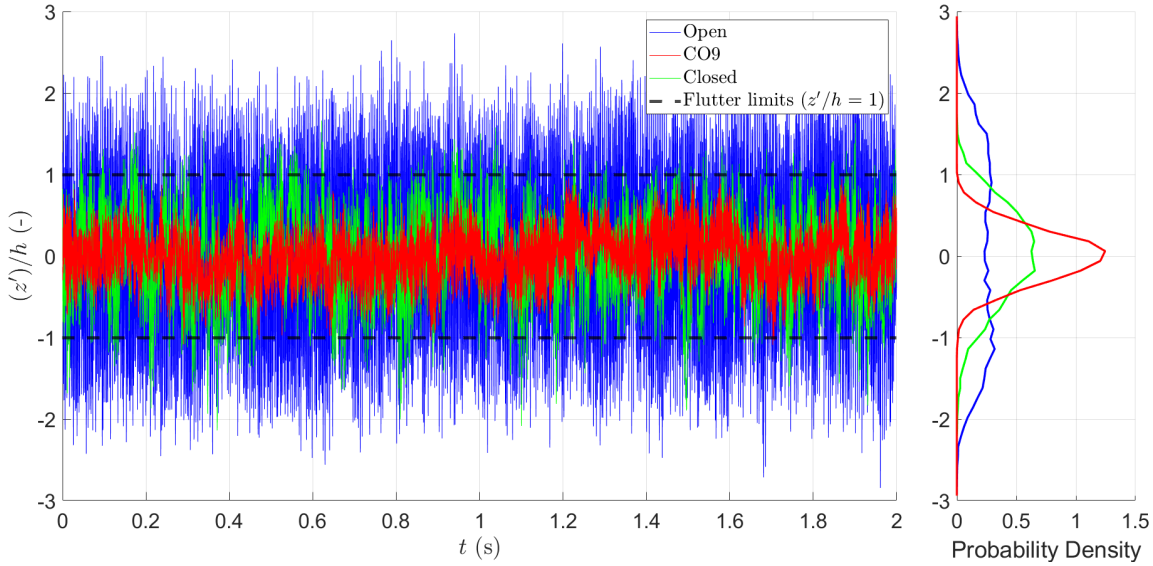

Figure 5.7: Comparison of panel fluctuations around the mean (left) for different cavity closure conditions and their probability density function (right).

Figure 5.7 not only shows the fluctuations around the mean at the point of highest maximum deviation; it also shows the probability density function (PDF) of this oscillating signal, which illustrates the probability of finding the signal to have a particular value. By observation, all the signals are symmetric around the mean, thus, there is no particular bias toward an upper or lower deformation. Furthermore, it can also be seen that the larger the amplitude of oscillation, the more spread out and smaller the peak is in the PDF. This is no surprise, as the larger the amplitude, the more likely it is to find points away from the mean. The opposite is also true: the smaller the amplitude, the less spread out the signal is, thus it is more likely to find most of the samples around the mean.

Table 5.1: Location and value of maximum standard deviation for investigated cases.

Case	x/a max. std.	y/a max. std.	Value max. std.
Open	0.31	0.02	1.134
Ventilated	0.33	0	0.314
Closed	0.80	0.02	0.583

5.2.2 Panel Motion Spectral Analysis

When taking the out-of-plane displacement of the panel at any location over time, it is possible to extract frequency information of its oscillatory motion. The current section aims to obtain a deeper understanding of how the spectral and modal content of the panel oscillations change with different cavity closure condition.

One of the techniques that can be used to extract the spectral content of a signal, is the computation of the power spectral density (PSD), as explained in detail in subsection 4.3.2. The PSD gives an indication of the amount of energy that is contained within each frequency. A comparison is made in Figure 5.8 between the three cases considered. Note that all the PSDs are normalised with respect to their peak value, such that each case has its peak frequency at 1. This way, however, does not allow for a relative comparison in the amount of energy contained in each case, but rather shows for each case where the dominant frequencies are and how the spectral content compares in energy within each case.

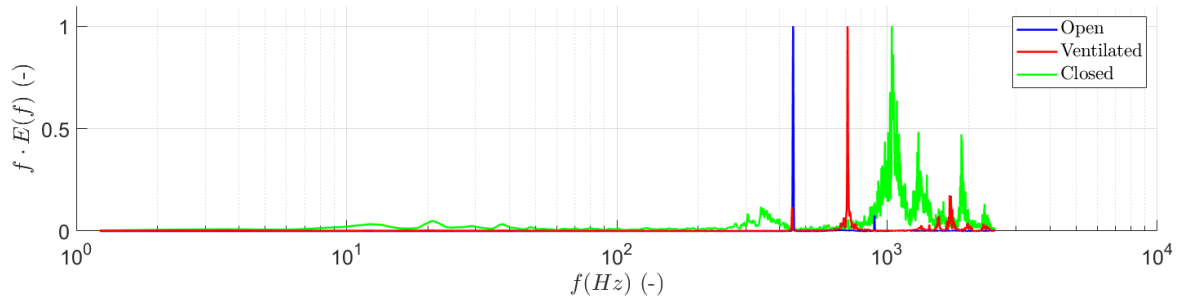

Figure 5.8: PSD of panel motion at its centre ($x = 0.5$, $y = 0$) for cavity conditions considered, all normalised with their peak value.

From Figure 5.8 it becomes evident that the spectral content of the panel oscillations changes significantly. For the closed-cavity case, this is no surprise, as the deformation and the location of maximum displacement differs drastically from the other two cases. Additionally, between the open and ventilated cases, which have similar mean shapes, there is also a significant difference in which frequency dominates the panel motion. For the open-cavity case, the panel response is clearly dominated by a single low frequency around 456 Hz. In contrast, for the ventilated case, the panel exhibits multiple frequency responses: one at a lower frequency, and several at higher frequencies. This reinforces the idea that for the open-cavity case, it is the flow coming into the cavity forcing the panel behaviour, while closing the cavity allows the panel to exhibit a ”free” oscillatory behaviour. Furthermore, when comparing these two cases, it can be seen that for the ventilated cavity, there is still a reminiscent component at 456 Hz from the open-cavity case. This is due to the nine holes present through which air can flow. It is therefore plausible that some pressure waves still enter the cavity, but of much less strength. Thus, it seems that the panel is not forced by the flow inside the cavity anymore.

When computing the PSD at various locations along a line, it is possible to construct a so-called spectogram. Such a spectogram, where the pre-multiplied PSD is computed along the chord of the panel at the mid-span location, is shown in Figure 5.9 for the three cases considered. It is important to note that an upper limit is set for the colormaps, such that contributions with a (much) lower energy content with respect to the peak would also become visible. This results in the higher peaks being completely saturated.

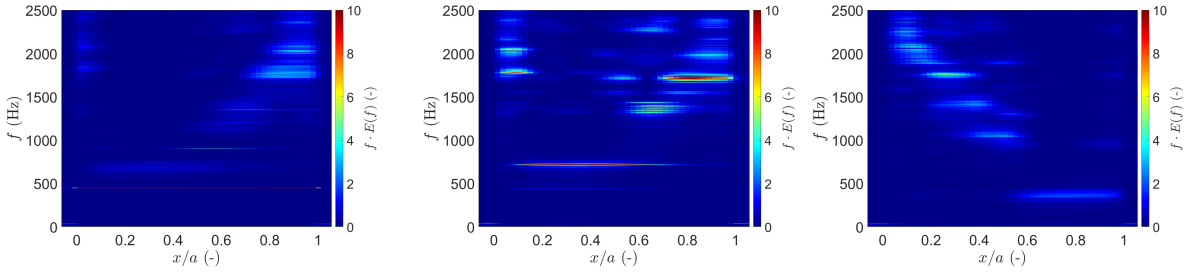

(a) Open cavity **(b)** Ventilated **(c)** Closed cavity

Figure 5.9: Pre-multiplied spectogram of panel oscillations along the chord at the spanwise location $y/a = 0$ for different cavity closure conditions.

Figure 5.9 reveals that the spectral content of the panel motion changes for every location across the panel. This is probably due to different bending motions having a contribution at different locations. For the open and ventilated cases, it is clear that a first bending mode has a large contribution, spread across the entire panel. For the closed-cavity case, this is only limited to the part of the panel towards the trailing edge. As discussed before, this is probably because a stiffening effect before the shock wave

prevents the panel to move, while after the shock, the pressure difference between flow and cavity is alleviated, allowing for the panel to oscillate. Because of this stiffening, the frequency of the oscillations is seen to shift to higher values in Figure 5.9c. For the same reason, the frequency shifts to higher values near the panel edges.

5.2.3 Proper Orthogonal Decomposition Panel Modes

By means of a POD analysis, it is possible to order the spatial modes of the panels by the energy they contain. A spectral analysis of the POD time coefficients reveals which frequencies are contained within each mode. The results of the POD method of snapshots (see subsection 4.3.4) for all three cavity conditions considered are presented and discussed in this section.

Open Cavity

The first three POD modes and their spectral content for the open cavity case, together with the relative energy content of the first ten modes, are presented in Figure 5.10. Note that as it is the shape of the mode and not the absolute values of the modes that is of interest, all the modes are normalised with the highest absolute value of the mode deformation.

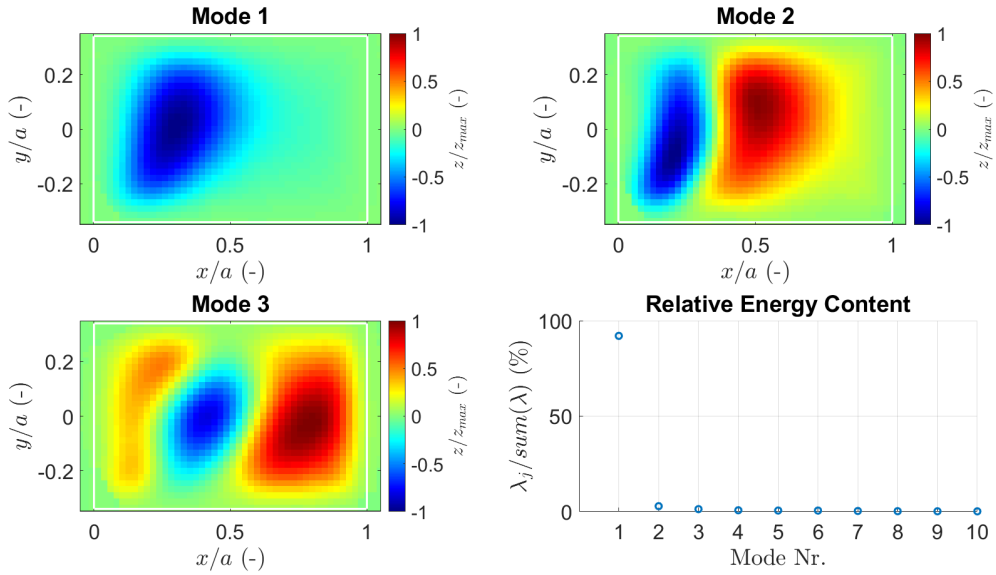

(a) POD modes and relative energy content

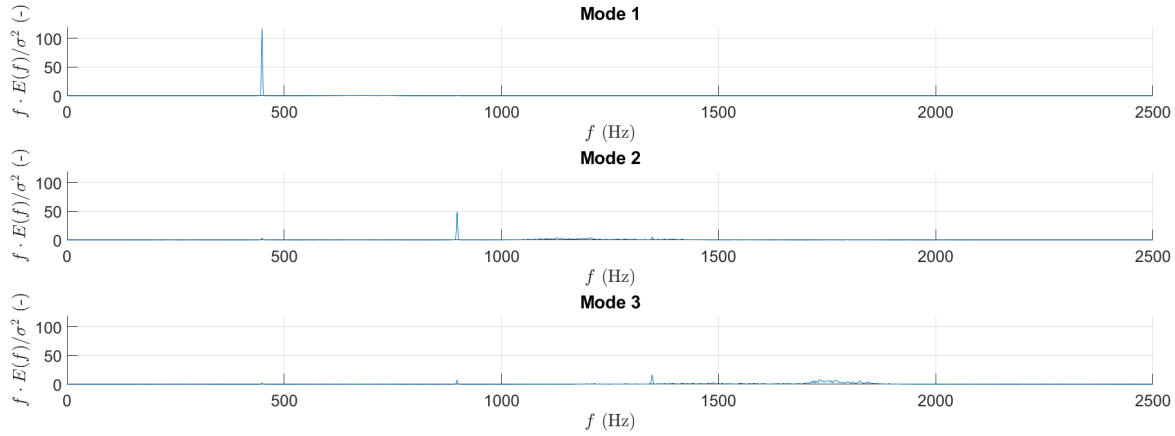

(b) POD mode frequencies

Figure 5.10: First three POD modes, their relative energy content and frequencies for the open-cavity case.

Remarkably, the first mode, which is a typical first-bending mode that as a ”trampoline-like” behaviour, contains 92% of all the energy contained within the panel oscillations. The frequency of this first mode is around 489 Hz, and its first two harmonics, 898 Hz and 1347 Hz, are exactly the dominant frequencies of the second and third mode. Such behaviour is typical for resonance and once again confirms the hypothesis that when the cavity is open, the pressure waves going inside drive the panel into resonance with tunnel vibrations. This behaviour, in combination with cavity resonance, was also observed by Varigonda and Narayanaswamy (2023). From the current study, it is uncertain whether the panel resonates with the waves, as schlieren experiments (see Figure 5.4) found the frequency of these waves to be around 750 Hz. Furthermore, the frequencies of the tunnel vibrations and pressure waves have been found to vary when comparing past studies (Aditya, 2022; Allerhand, 2020; Mathijssen, 2022) and depend on multiple parameters. However, also by D'Aguanno et al. (2023) and Aditya (2022) harmonics of the first mode where found, suggesting resonance is taking place. Therefore, it is plausible that the high energy of these waves force the panel to resonate with whatever vibrations are present during the run, and not specifically to the frequency of the cavity pressure waves. By observation of the second and third mode, they resemble a second and third bending mode, respectively. As they exhibit mostly symmetrical behaviour in the spanwise direction, no significant torsional contribution seems to be present.

Ventilated Cavity

In a similar fashion as the open cavity case, the first three POD modes and their spectral content for the ventilated case is displayed in Figure 5.11, together with the relative energy content of the first 10 modes.

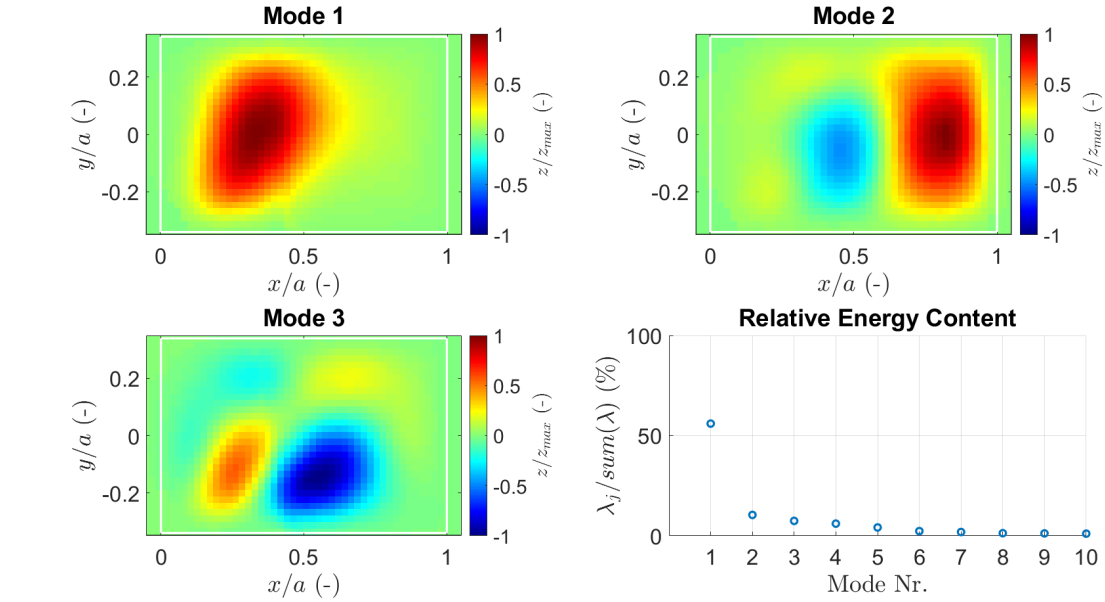

(a) POD modes and relative energy content

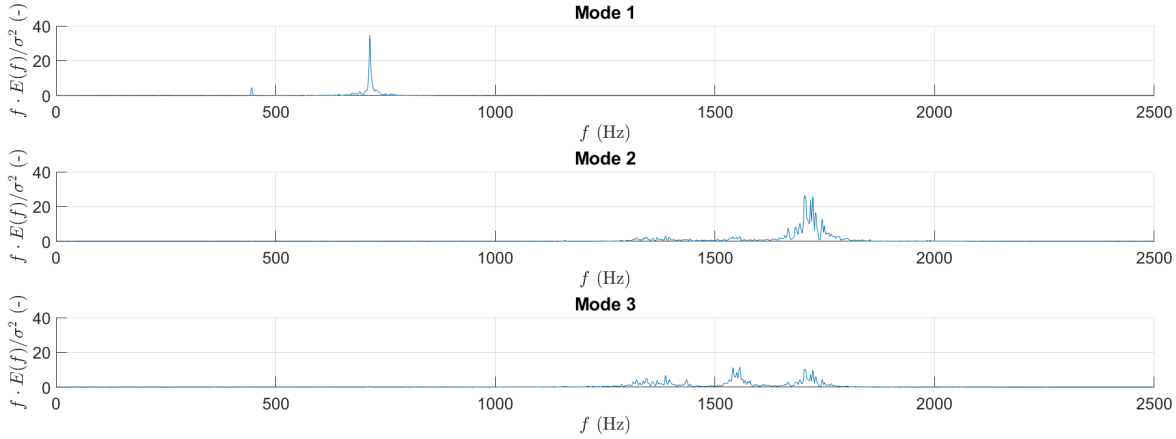

(b) POD mode frequencies

Figure 5.11: First three POD modes, their relative energy content and frequencies for the ventilated case.

By comparison of the open cavity case, it stands out that the first mode does not contribute as much to the overall energy content of the oscillation (56%) and that a more significant amount of energy is contained in the subsequent modes (10% and 7.5% for the second and third POD mode respectively). This shows that without the strong pressure waves entering the cavity, the panel is not forced by a single resonant frequency anymore, but rather exhibits its natural flutter modes for the specific conditions the panel was tested in. This is further reinforced by observing the spectral content of the modes, where the higher modes are not harmonics of the first mode anymore. Note, however, that in the first mode, a small contribution at 489 Hz is still present, as also observed in the spectral analysis in subsection 5.2.2. Similar to the discussion there, it seems that because of a decrease in strength of the waves entering the cavity, the panel is not forced into resonance anymore. It can also be observed how for the second and

third mode, the spectral content overlaps. This is due to the fact that the POD method does not seek modes with a specific frequency (such as *Dynamic Mode Decomposition*), but rather to decompose the field into orthogonal directions and order them by their relative energy content. That is why it is possible for the different modes to exhibit similar frequencies, but a different spatial mode, as two modes might have similar spectral behaviour but a different energetic contribution to the oscillation.
Lastly, similar to the open cavity case, the first POD mode is at the location of maximum standard deviation. This is no surprise as the location of maximum standard deviation is an indication for where the oscillations around the mean are the highest. The second mode exhibits a third bending mode, which is spanwise symmetric, while the third POD mode does not have this symmetry anymore. This could signify the presence of a minor torsional mode within the panel oscillation.

Closed Cavity

Finally, Figure 5.12 shows the first POD modes with their spectral content and relative energy content of the closed cavity case.

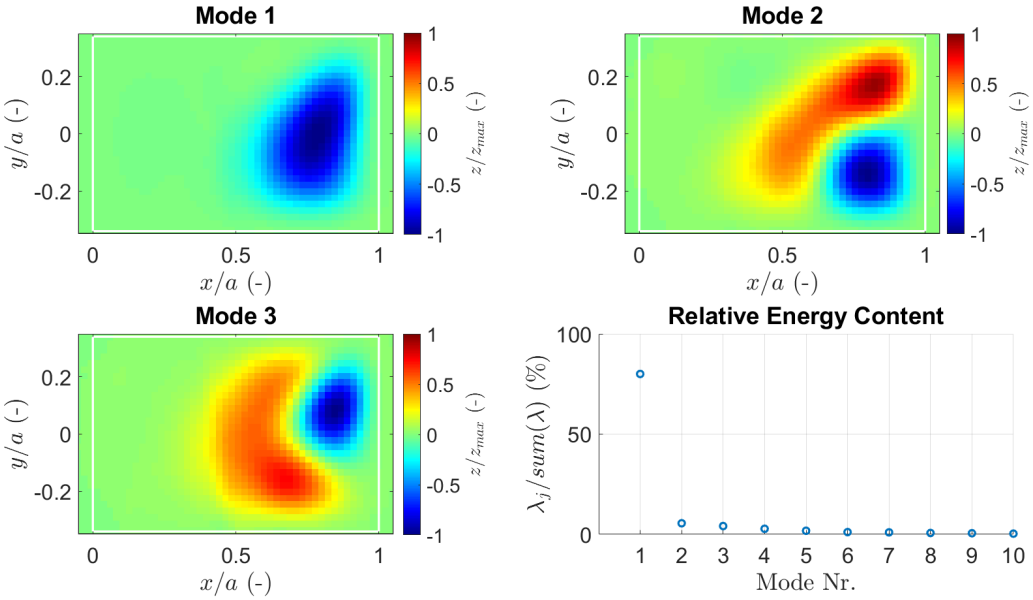

(a) POD modes and relative energy content

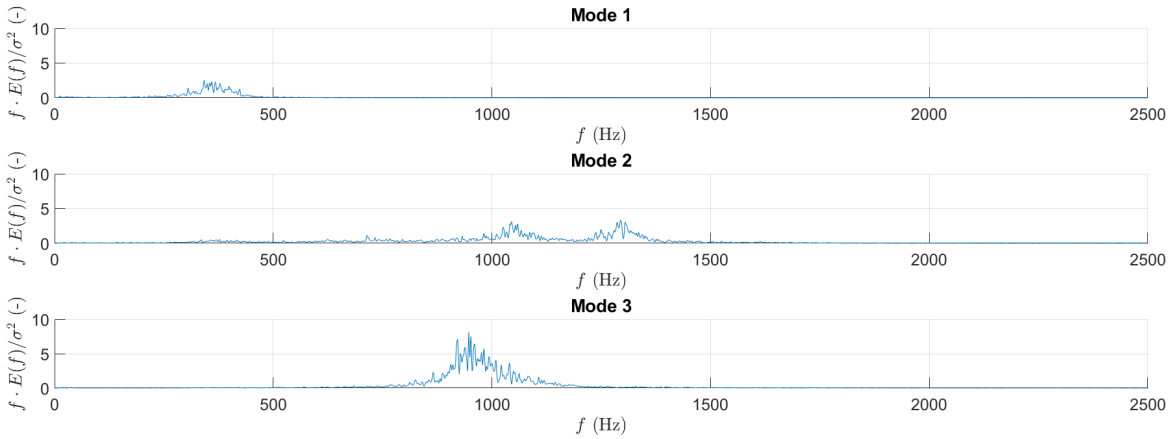

(b) POD mode frequencies

Figure 5.12: First three POD modes, their relative energy content and frequencies for the closed-cavity case.

At first sight, the POD modes look very different to the first two cases. As discussed by means of the location of higher standard deviation, this is because the closed cavity case exhibits a completely different flutter behaviour with respect to these other cases and another location of maximum oscillation. It is because of this different behaviour, due to the closed cavity environment, that it is difficult to explain why the first mode has such a high energy content (80%). Analogous, however, to these other cases is that the shape of the dominant first mode is similar to the shape of the standard deviation.
Another consideration is that most of the energy is contained in the second half of the panel. As discussed before, the high pressure difference in this case between cavity and main flow probably stiffens the panel in its first half, while after the shock, this pressure difference decreases, allowing for the panel to oscillate and, therefore, this location contains the highest energy. Looking at the frequency content of the first three POD modes in Figure 5.12b, the first mode is centred around a frequency of 367 Hz. The second (1046 Hz and 1296 Hz) and third mode (947 Hz) are not harmonics of the first, most dominant mode. Thus, resonance behaviour is likely to be absent in this case. In addition, note how the normalised, pre-multiplied PSD of the ventilated and closed cavity case is much lower with respect to the open cavity case, once more highlighting the effect of preventing the strong pressure waves inside the cavity underneath the panel.

At the end of this section, the POD results are all summarised in Table 5.2, which shows the frequency content and relative energy content of the first five POD modes of each case considered.

Table 5.2: Summary of POD analysis containing the dominant frequency of the first five POD modes and their respective relative energy contribution for different cavity closure conditions.

	Open		**Ventilated**		**Closed**	
	Dominant Frequency [Hz]	Relative Energy Contribution [%]	Dominant Frequency [Hz]	Relative Energy Contribution [%]	Dominant Frequency [Hz]	Relative Energy Contribution [%]
Mode 1	449	92.0	714	56.0	355 ± 50	80.0
Mode 2	898	2.86	1704 ± 40	10.44	1044 ± 60, 1287 ± 50	5.52
Mode 3	1346	1.31	1540 ± 20, 1704 ± 20	7.46	947 ± 70	4.14
Mode 4	1558, 1580	0.71	1555 ± 20	6.10	1304 ± 80	2.77
Mode 5	1346	0.57	1387 ± 30	4.19	1402 ± 50	1.78

5.2.4 Phase-Averaged Panel Displacements

As introduced in subsection 4.3.3, the large number of samples taken during the DIC experiments (N = 10000) and the periodicity of the signal allow for a phase average analysis. This method gives the opportunity to study the mean deformation of the panel in different instances with respect to a reference signal. In the current study, the reference signal is taken to be the mean deformation value over time at the point of maximum standard deviation for each individual case. This point might vary in the streamwise direction between the cases, but is around the mid-plane of the panel for the three cases considered. As the panel exhibits a periodic up-and-down motion, this motion is divided up in four phases, where phase 1 represents the most upward position of the panel and phase 3 the most downward; phase 2 and 4 are in between those two phases. An example of the phase division on the signal of the open cavity case is shown in Figure 5.13. It can be seen that the signal is indeed periodical and that, therefore, the tracking of the phases is successful.

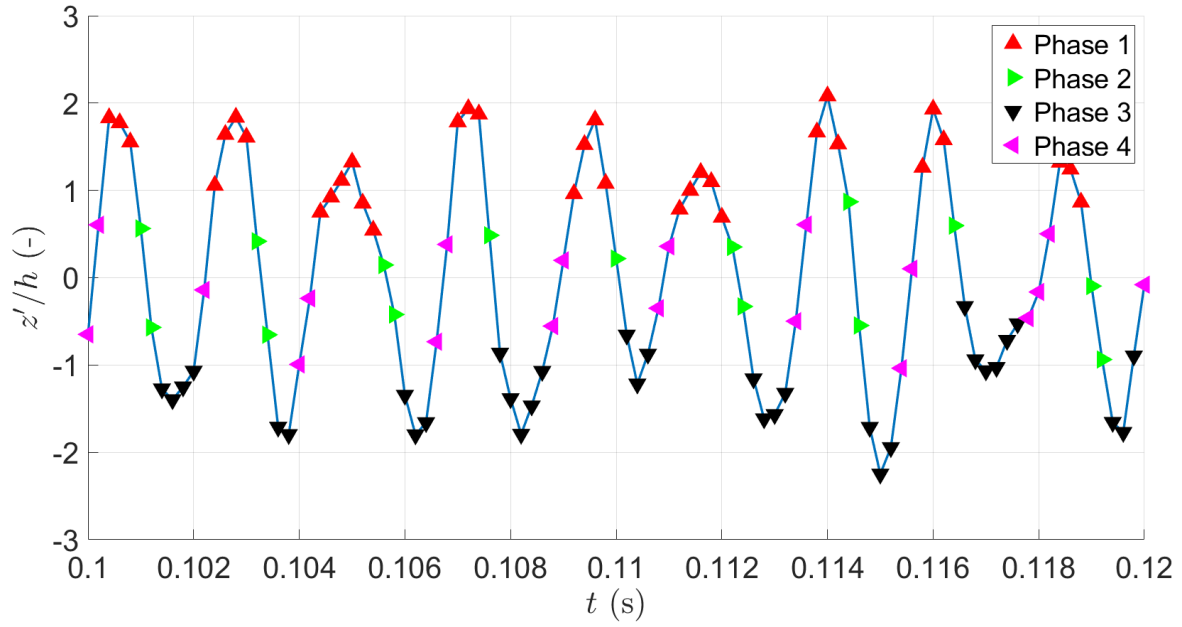

Figure 5.13: Example of phase-averaging procedure on panel fluctuations signal for the open-cavity case.

Once all the instantaneous deformation fields are divided among the four phases as shown in Figure 5.13, the phase averages can be taken with the number of images out of which each phase consists, respectively. The averaged deformation field of the four phases for the open-cavity case is shown in Figure 5.14

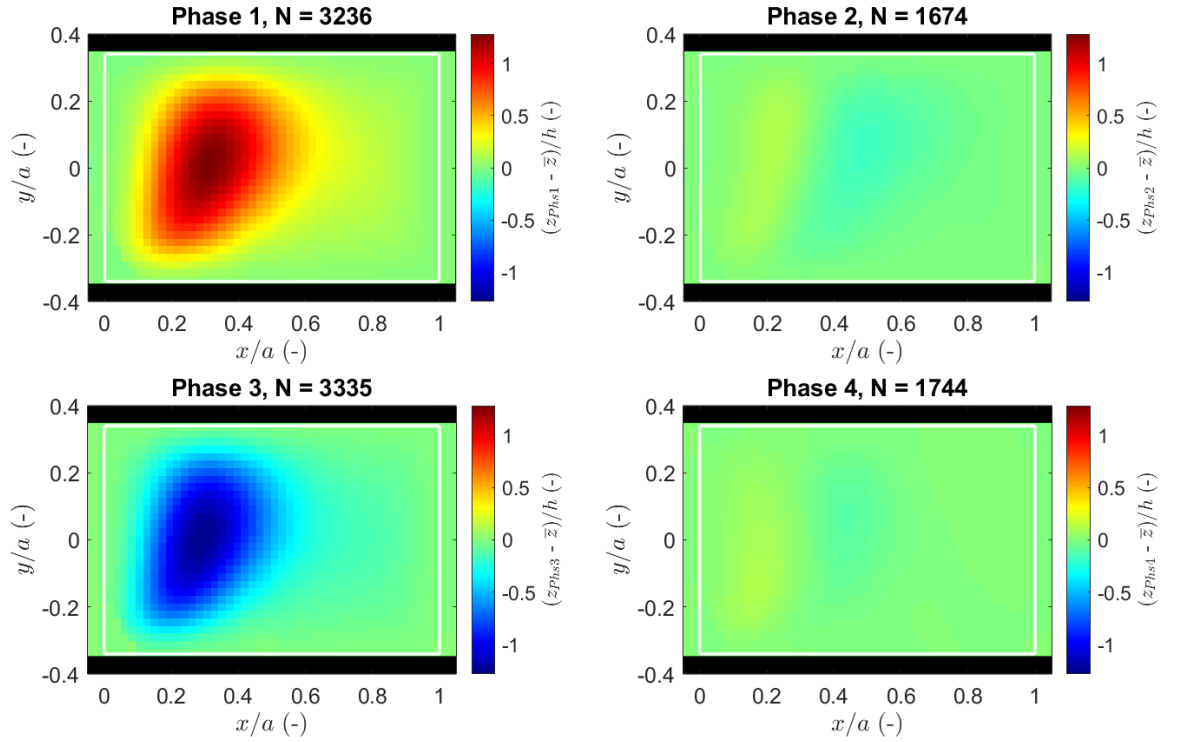

Figure 5.14: Mean-subtracted, phase-averaged panel displacements of a fluttering panel with the cavity open, using the displacement of the panel at the location of highest standard deviation.

From Figure 5.14 it is visible that phases 1 and 3 resemble the shape of the standard deviation of the deformation and the first POD mode. This is a result of this first POD mode being by far the most energetic mode and therefore contributing the most to the deformation shape in the different phases on average. Note however that in phase 2 and 4, where the dominant POD mode goes into its "equilibrium position", the presence of higher bending modes is slightly visible. Furthermore, it can be seen that the number of samples between phases 1 and 3 and phases 2 and 4 is very similar, showing the robustness and consistency of the used phase averaging algorithm.

The phase averaged deformation for the three cases considered is presented in Figure 5.15, where only the deformation at the mid-span plane ($y = 0$) is taken.

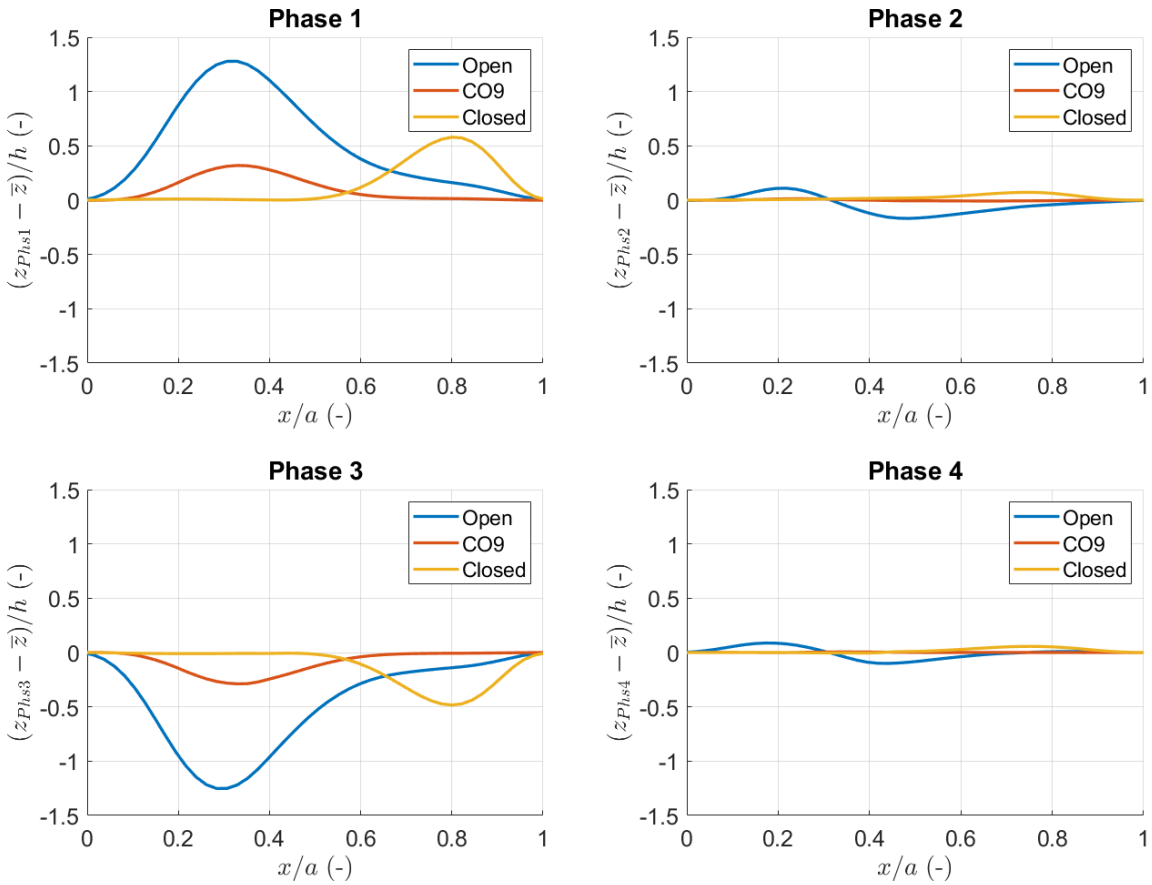

Figure 5.15: Mean-subtracted, phase-averaged panel displacements at $y/a = 0$ for different cavity closure conditions.

It is no surprise that as the most dominant mode is similar among the open-cavity and ventilated cases, the phase averaged shapes of these cases look similar. The difference is that the amplitude of the oscillation is lower since there is no forced flutter. This follows the results as shown in Figure 5.7. Similar to the discussion above, the closed case has its own deformation shape due to the different pressure-loading along the chord of the panel. Similar among all cases, however, is that the most energetic oscillation mode is mostly present in phase 1 and 3, while a small contribution of the other oscillation modes is visible in the other two phases, although this might not be directly visible from the chosen range in Figure 5.15.

5.3 Temperature Effect

From section 5.2 it becomes clear that in the ST-15 wind tunnel, the state of the cavity, specifically whether it is open or closed off, drives the dynamics of the panel deformation. One of the aspects that is not discussed yet is how the temperature distribution over the panel and the cavity temperature are affected by this. The aim of this section is, therefore, to discuss the impact of the cavity closure on these temperatures by means of thermocouple and infrared measurements. This discussion is divided, similar to the OFV experiments, between the case where no shock generator is present (see subsection 5.3.1) and the case where it is present (see subsection 5.3.2). Finally, an attempt is made to observe what effect the temperature has on the panel oscillations over time by performing a much longer experiment at a lower acquisition frequency. These results are presented in subsection 5.3.3.

5.3.1 No Shock Generator

As discussed before in subsection 5.1.1, there are no significant variations across the panel in the absence of a SWBLI structure. Therefore, it is no surprise that, as shown in Figure 5.16, the temperature across the thin or rigid portion of the plate is constant. Note that the comparison of absolute temperatures is not straightforward as the start of the measurements is not the same for the different cases with respect to the start of the wind tunnel.

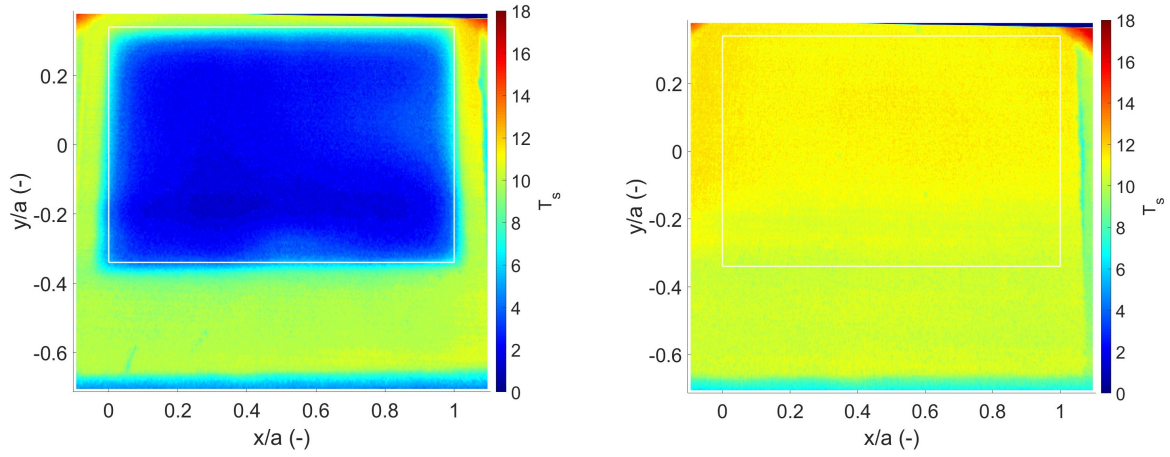

(a) Thin panel **(b)** Rigid panel

Figure 5.16: Infrared images of a thin (left) and rigid (right) panel without the presence of a shock generator.

Figure 5.16a shows that a large temperature gradient is present between the thin portion of the plate and the thicker frame of the plate. This is due to the difference in thermal inertia of the two parts with different thicknesses. In comparison, Figure 5.16b shows that the temperature is mostly uniform across the whole plate as the thickness and, therefore, the thermal inertia of the panel is the same everywhere. The slightly higher temperature at the edge of the plate might be due to reflections of the window at the opposite side of the wind tunnel[1]. Thus, for further discussion in this section, the results presented in Figure 5.16 allow for taking only a single point on the panel for comparisons of temperature evolution over time.

Four distinct cases can be considered by varying between the thin and rigid panel and by opening or closing the cavity. If a single point is taken at the side of the panel, it is possible to visualise the temporal

[1]As the IR-camera was placed at the Delft-side of the ST-15 wind tunnel, the obtained data was flipped such that the orientation would be consistent with other measurement obtained with cameras placed at the Rotterdam side. That is why for the IR-data, the camera is located at the upper side with respect to the used coordinate system.

variation of the temperature in that point. As Figure 5.16 showed equal temperature across the whole plate, it is assumed that the temperature in this point can also be considered the entire panel temperature. The temporal evolution of the temperature difference between this point and a point taken at the frame is shown in Figure 5.17.

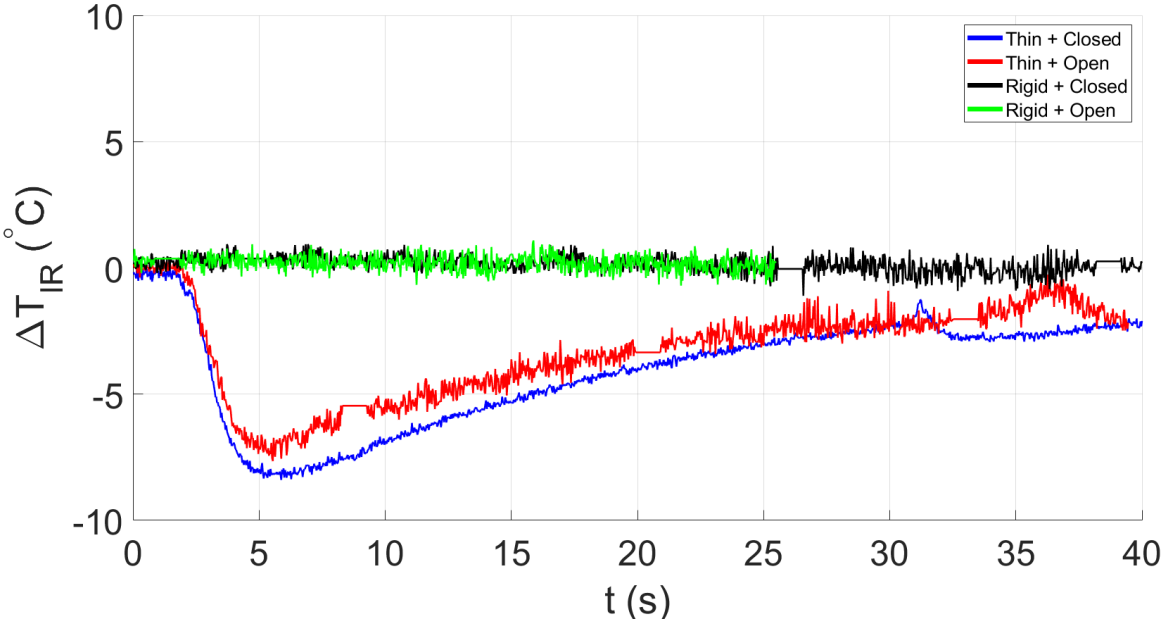

Figure 5.17: Temperature difference from infrared imaging between thin portion and frame of panel over time for combinations of cavity closure conditions and panel thickness. Shock generator is absent.

The presented ΔT value is used often in literature as it is also a measure for the thermal stresses present between the frame of the panel and its thin part. This ΔT is defined as:

$$\Delta T = T_p - T_f, \tag{5.1}$$

where T_p is the temperature of a point taken at the edge of the panel and T_f the temperature of the frame. Note that the presented data in Figure 5.17 is of varying length due to an inconsistent runtime of the experiment and the acquisition is stopped at different moments. Nevertheless, it is possible to observe some trends. Firstly, it can be seen that panels with the same thickness follow the same trend. This, again, is due to their difference in thermal inertia. In addition to this, it is because of the lower thermal inertia that the thin panels reach an equilibrium temperature shortly after the start of the wind tunnel. In Figure 5.17, this is visible as the point where the ΔT reaches a minimum. In contrast, the rigid plate does not reach an equilibrium. This is not directly visible from Figure 5.17, but as the ΔT for the rigid cases is zero, as a consequence it can be concluded that the frame temperature is also equal to the temperature of the rigid case (in absence of a shock). Thus, as the frame temperature does not reach an equilibrium, the same can be said about any point in the rigid plate case.

The thermocouple data obtained at the bottom side of the panel gives some other interesting insights into the temperature development at particular locations. Figure 5.18 shows the thermocouple measurements as obtained from the same experiments as Figure 5.17. Figure 5.18a shows the temperature difference between frame and panel, and Figure 5.18b the cavity temperature. Additionally, the absolute temperature at the edge of the panel is presented in Figure 5.18c.

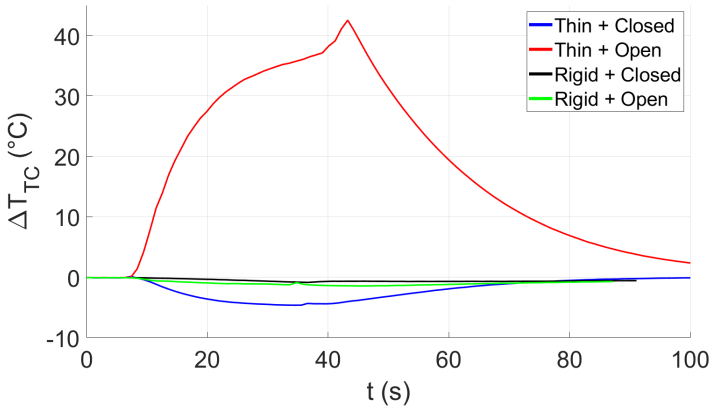

(a) ΔT panel edge and frame

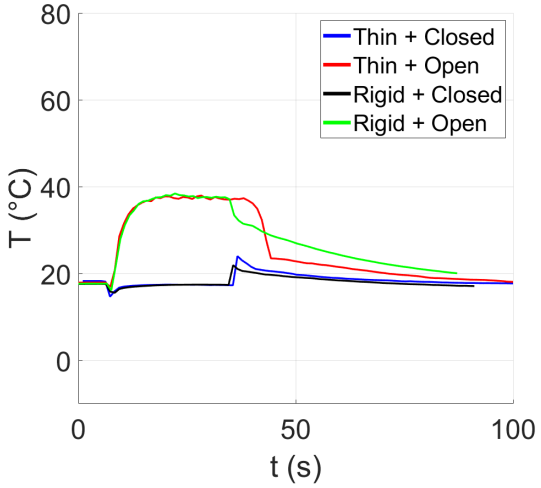

(b) Cavity temperature

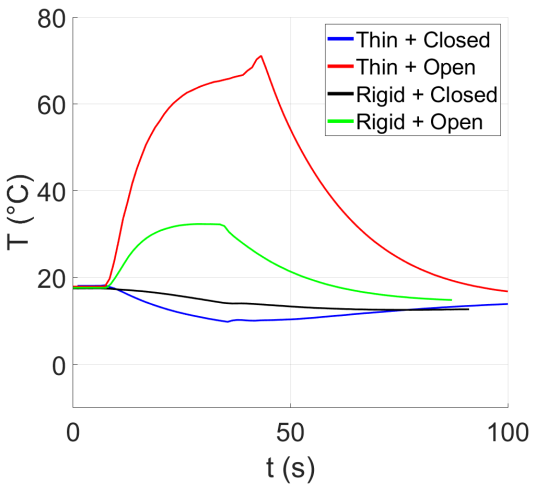

(c) Panel edge temperature

Figure 5.18: Temperature evolution over time taken from thermocouple data in the absence of a shock generator.

By a quick comparison with the infrared data, the thermocouple measurement look significantly different. Figure 5.18a reveals a different temperature response of the panel. As expected, the rigid cases show a δT that is near zero, as there is no difference between the frame and the panel: the plate has the same thickness everywhere. The significant difference appears for the thin panel where the cavity is left open. The panel seems to heat up and almost reach an equilibrium at a temperature near 70 °C, as shown in Figure 5.18c. In addition to this, Figure 5.18c reveals that also for the rigid case the panel temperature rises when the cavity is left open. In contrast, when the cavity is closed, the data shows more agreement with the IR data. A possible explanation of this rise in temperature can be found in Figure 5.18b, where it can be observed that the cavity temperature also rises when the cavity is open. Schlieren experiments have revealed that in those cases, strong waves enter the cavity, which by compression can increase the temperature. Therefore, it is as if the cavity is heating up the panel from below. However, this does not fully explain the great rise in temperature for the thin case above the cavity temperature. Data from multiple experiments confirm the repeatability of this measurement.

In the hypothetical case where the temperatures would be taken as physical, direct comparison between the IR and thermocouple (TC) data would result in a temperature difference between top and bottom of the thin panel of around 65 °C within 0.3 mm. For the rigid case, this would be around 20 °C. For a better understanding of the temperature conditions with an open cavity, further research is needed as detailed analysis of temperature effects was out of the scope of this research.

As the data with a closed cavity seemed to follow the expected temperature behaviour, a direct comparison is made between IR and TC data for those cases and presented in Figure 5.19.

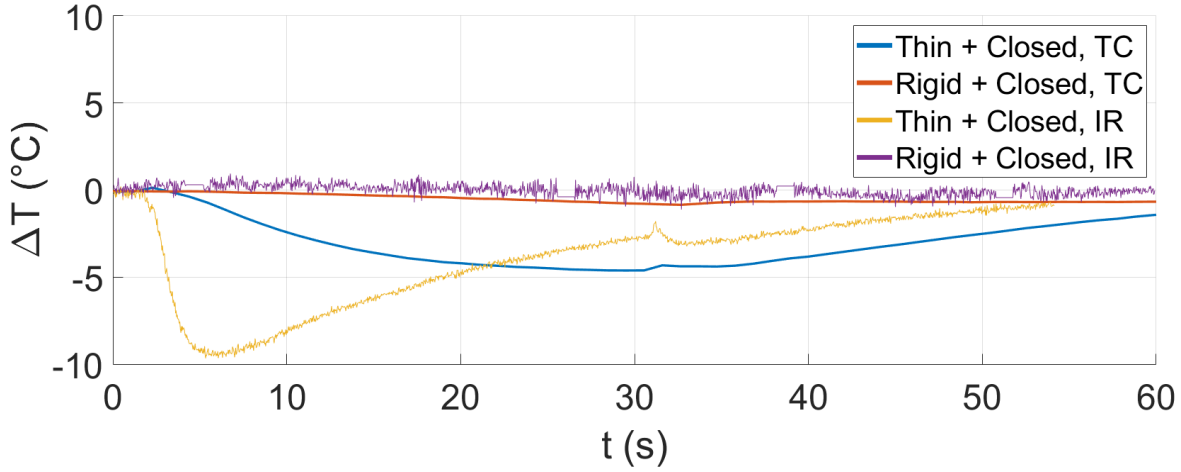

Figure 5.19: Comparison of infrared and thermocouple data for closed cavity cases.

Following the previously observed trend, the rigid panel cases have a near-zero ΔT, thus are in agreement with each other. However, even though both show a negative ΔT, the IR and TC data for the thin cases differ in a clear way: the TC data does not show an equilibrium situation within the runtime. This can be seen as there is no clear minimum present as in the IR data. This is probably due to the larger response time of the thermocouples to measure the correct temperature, making the curve decrease less strongly at the start. In other words: the thermocouple takes a longer time to measure the equilibrium temperature of the thin portion and, therefore, the difference ΔT remains smaller.

5.3.2 With Shock Generator

In a similar fashion as the previous subsection, it is possible to analyse the temperature variation over the panel, but in this subsection with the presence of a shock generator. In Figure 5.20, the contour maps are shown, revealing the spatial variation in temperature in the presence of a SWBLI structure, and temperature patterns over the plate.

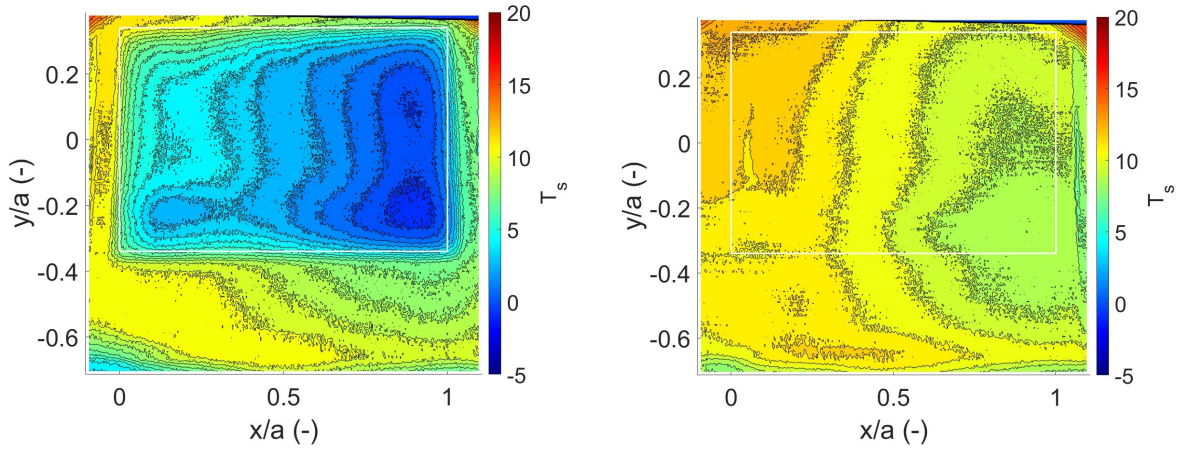

(a) Thin panel **(b)** Rigid panel

Figure 5.20: Infrared images of a thin (left) and rigid (right) panel in the presence of a shock generator.

Both thin and rigid panels reveal a bow-like temperature structure, which looks similar to the OFV structure discussed in subsection 5.1.2. Similar to the case without a shock generator, the temperature difference between the thin part and frame is larger for the thin panel with respect to the rigid panel, where the temperature distribution of the latter is continuous across the plate without showing sudden changes across the span. This observation is also confirmed by inspection of Figure 5.21, where the temperature difference between frame and panel is shown in time.

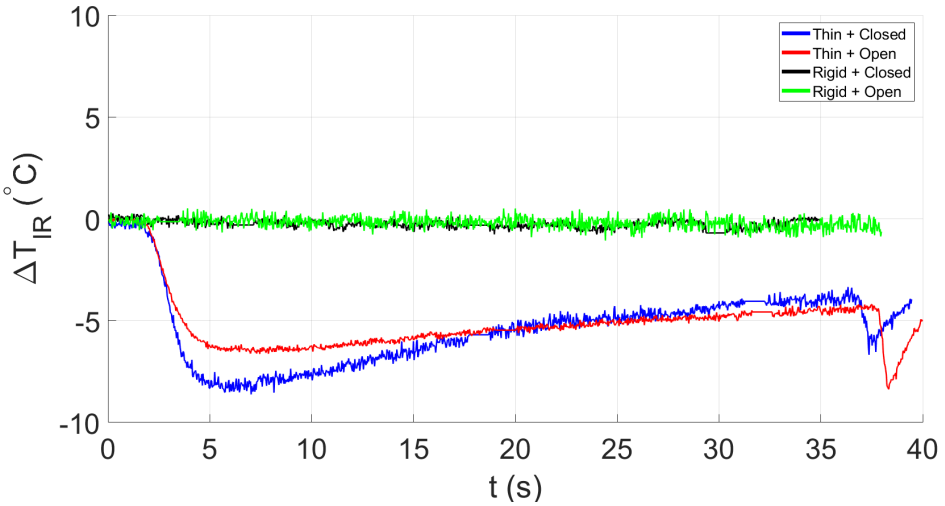

Figure 5.21: Temperature difference from infrared imaging between thin portion and frame of panel over time for combinations of cavity closure conditions and panel thickness. Shock generator is present.

For the rigid cases, the temperature difference is near zero, confirming that the temperature variation across the span is minimal. A similar trend as for the no-shock-generator case is found for the thin panel, which means that also in the presence of a SWBLI structure, the temperature of the thin portion decreases faster than the frame. However, here the minimum does not correspond to an equilibrium point for the point on the panel. This is shown in Figure 5.22, which presents the extracted absolute temperature from a point at the edge of the panel over time.

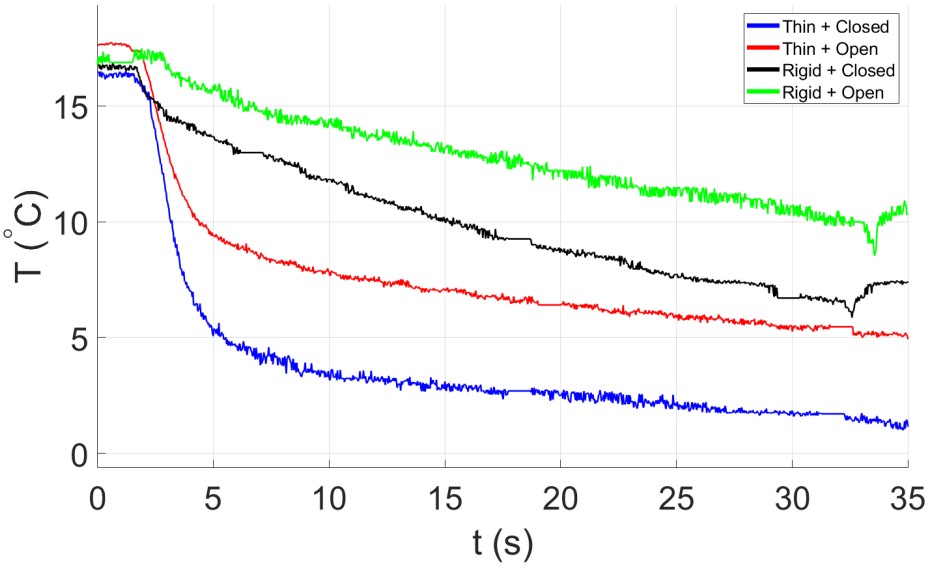

Figure 5.22: Temperature evolution over time from infrared imaging taken at a point at the edge of the thin panel portion for for combinations of cavity closure conditions and panel thickness.

Figure 5.22 shows that, as expected, the thin panels cool down faster because of their lower thermal inertia. However, unlike the no-shock-generator case, the absolute temperatures differ from case to case, depending on the cavity closure. One possible explanation would be that, similar to the no-shock-generator case, the cavity temperature rises when the cavity is left open. However, as shown in Figure 5.23b, this is not the case, as the cavity temperature seems to remain constant after start-up. Similar to what is concluded in subsection 5.3.1, further thermal research is needed to understand the differences that are shown in Figure 5.22. Also shown in Figure 5.23 is the ΔT recorded by the thermocouples (see Figure 5.23b).

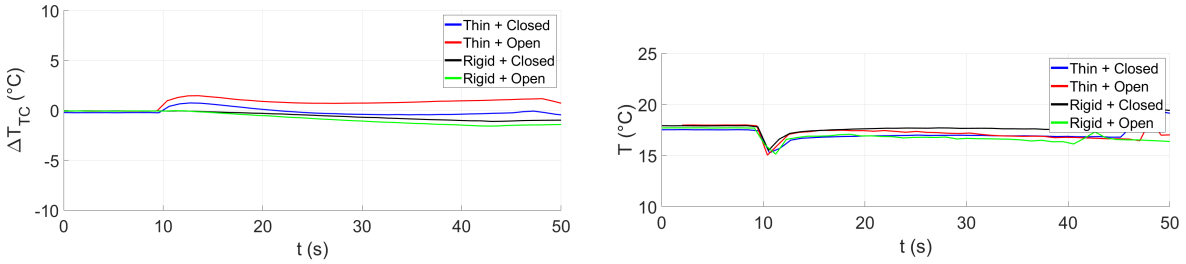

(a) (b)

Figure 5.23: Temperature difference from thermocouples at bottom of the panel (a) and cavity temperature (b) over time for combinations of cavity closure conditions and panel thickness. Shock generator is present.

Unlike Figure 5.21, Figure 5.23a shows a positive ΔT at tunnel start-up for the thin panels, meaning that there must have been a temperature rise in the thin panel at the start of the run. This could well be because of the sensibility of the TC to wind tunnel start-up phenomena. This hypothesis is supported by the fact that this rise does not appear in the IR data and that IR imaging is a non-intrusive measurement technique. Combining this hypothesis with the larger response time of the TC could explain the discrepancy between the IR and TC results.

5.3.3 Temperature Effects Over Time

A test with a flexible panel and open cavity was executed at a lower acquisition frequency ($f = 400$ Hz), which allowed for a longer acquisition time ($t_{acq} = 20$ s). This in turn made it possible to observe the evolution of the amplitude of the oscillation over time. As the acquisition frequency is low, it is not possible to perform a spectral analysis and observe possible changes in mode shapes over time. It is possible, however, to decompose the panel motion in three distinct components, as follows:

$$z(\vec{x},t) = \overline{z}(\vec{x}) + \tilde{z}(\vec{x},t) + \tilde{z}'(\vec{x},t), \tag{5.2}$$

where $\overline{z}$ is the mean deformation of the panel, $\tilde{z}$ a moving averaged signal of the original deformation motion[2], centred around the mean deformation value in each point, and $\tilde{z}'$ the oscillation around the moving averaged motion. Of interest in this subsection are $\tilde{z}$ and $\tilde{z}'$, as those are the components that could be affected by changes in temperature over time. Different points are taken at several locations along the mid-chord and mid-span locations, of which their oscillation in time is tracked and decomposed as proposed in Equation 5.2. The fluctuations $\tilde{z}'$ for these different points are shown in Figure 5.24. Note that these fluctuations are all centred around the sliding averaged, but for clarity are all offset by an integer value; this is done such that all the signals do not overlap and clarity is improved.

[2]Moving average uses 2000 frames around temporal point to produce the averaged value in that point in time.

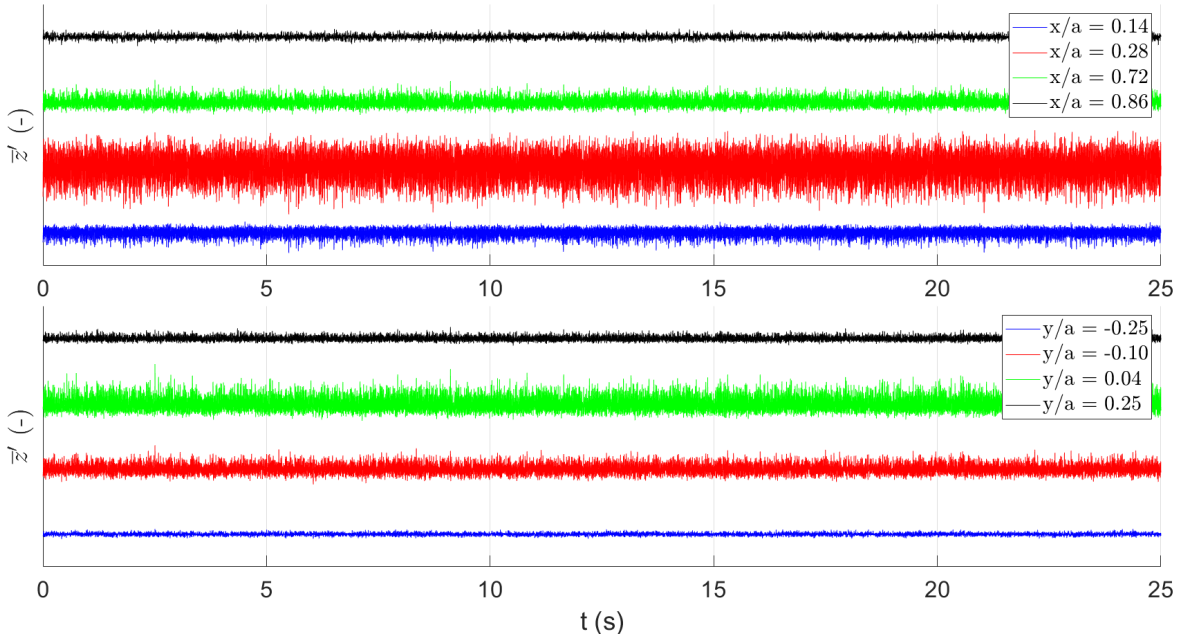

Figure 5.24: Fluctuations $\tilde{z}'$ around moving averaged panel motion at different points along $y = 0$ (upper) and $x = 0.5$ (lower).

From Figure 5.24 there does not seem to be a significant change in the amplitude of the oscillations over time. Thus, it seems that the amplitude of oscillations in time is not affected by the change in temperature. Moving to the moving averaged signal, $\tilde{z}$, firstly the signals in time at the mid-span location ($y = 0$) is presented in Figure 5.25.

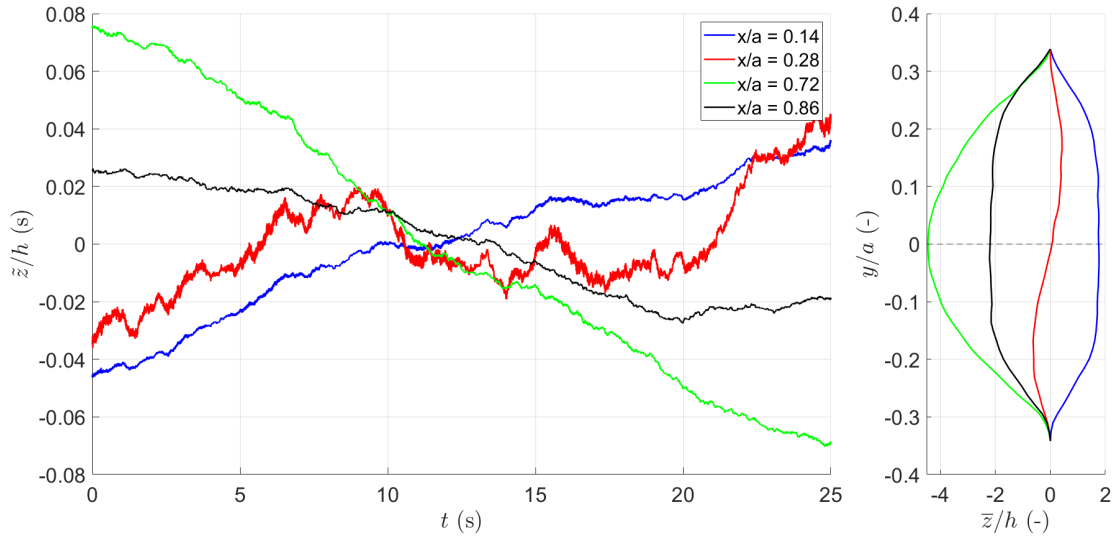

Figure 5.25: Moving averaged signal of panel motion $\tilde{z}$ (left) at $y = 0$ and different streamwise locations over time and the mean spanwise deformation shape at the respective streamwise points.

In contrast to the fluctuations $\tilde{z}'$, the moving averaged signal does change over time. This shows that instead of the amplitude of oscillation changing, it is the mean deformation of the panel that changes over time. A comparison with the mean spanwise deformation shape shows that the direction of this change depends on whether the mean deflection is upwards or downwards. A generalised observation is

that if the mean is upward, it changes towards a more upward position, while if the mean is downward, it changes to a more downward one. In other words: the mean deformation of the panel moves towards more extreme positions. These changes can certainly not be neglected as for some locations the change is of almost 15% of the panel thickness, especially if this trend continues over time. A similar trend can be observed in Figure 5.26, but instead spanwise points along the mid-chord position are taken. Confirming the trend in Figure 5.25, as the mean deformation at the mid-chord is downward, the change in deformation over time becomes even more downward. Both in Figure 5.25 and Figure 5.26 the change is more extreme for locations towards the centre of the panel, where the deformations are also the largest.

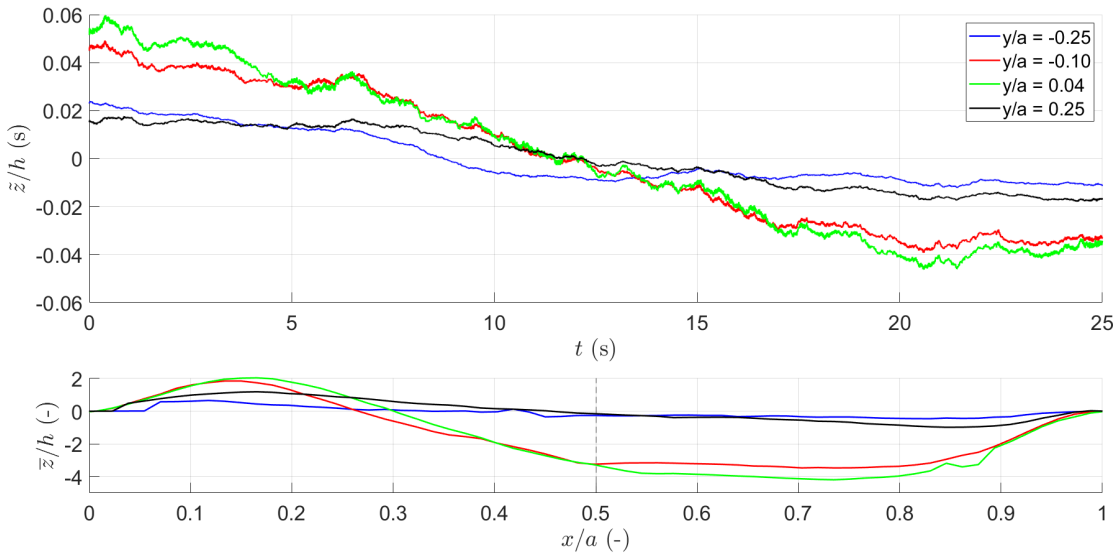

Figure 5.26: Moving averaged signal of panel motion $\tilde{z}$ (left) at $x = 0.5$ and different spanwise locations over time and the mean streamwise deformation shape at the respective spanwise points.

First it was hypothesised that the change of mean deformation over time was due to changes in cavity pressure over time. However, this hypothesis was discarded as the pressure loss during the run was of order 0.001 bar. That is why it is more likely that the change is due to temperature effects over time. This would be in agreement with research by Brouwer et al. (2023), where it was observed that the mean deformation of an upward deflected panel would increase even more with a lower ΔT, as is the case for the current study (see Figure 5.21 showing that ΔT decreases over time for a flexible panel with open cavity). Furthermore, they observed a small difference in the panel modes, but again, this analysis is not possible for the current study due to the low acquisition frequency used for this longer test; the shorter tests at higher frequency do not exhibit a large ΔT after start-up, and therefore cannot be used for a modal analysis. In conclusion, the change in mean deformation shape of the panel during the run is attributed to the change in ΔT over time, as is in agreement with Brouwer et al. (2023) and due to the exclusion of significant cavity pressure changes.

6

Mean Deformation Effects on SWBLI

While the previous chapter focused on the panel dynamics, the aim of this chapter is to take a closer look at the flow over the panel and the differences between the different cases considered. Previously, three cases were studied: the open-cavity, the ventilated cavity, and the closed-cavity case. In the following part, two additional cases are considered: the rigid, flat panel and the rigid deformed (RD) panel. The latter panel has the mean deformation taken from the open-cavity case, and is therefore also similar to the mean deformation of the ventilated case. Thus, it is possible to study what the effect is on the SWBLI of a fluttering panel, with and without resonance oscillations, and what the effect is of the shape of the panel, once ”frozen” (i.e. without the ability to move). In section 6.1, a comparison is made between the different cases in terms of the mean flow properties of the flow components. Then, section 6.2 and section 6.3 continue the comparison between the cases, but in terms of the interaction length and the separation dynamics respectively. Finally, section 6.4 attempts to identify the coupling between the DIC and PIV results, such that the presence of fluid-structure can be identified. This is done for the open-cavity and the ventilated case, as those are similar cases, for which the panel can move.

6.1 Cavity Closure Effect on Mean Flow Properties

In this section, a comparison is made between the different cases in terms of the average flow fields. The method by which these average flow fields are computed is described in subsection 4.3.1. The average flow field of the horizontal and vertical velocity components for the baseline SWBLI case (i.e. the rigid plate) is shown in Figure 6.1. Note that for comparison with other cases, the flow fields are normalised with the freestream velocity, as measured in each case respectively.

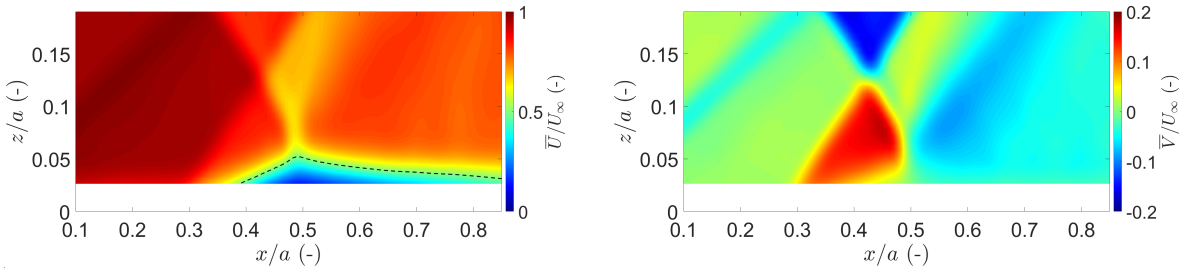

(a) Horizontal velocity component

(b) Vertical velocity component

Figure 6.1: Mean horizontal (left) and vertical (right) velocity components over the mid-span of a rigid plate.

From Figure 6.1, the main SWBLI features can be recognised. The impinging and reflected shock waves are visible by the drop in the horizontal velocity component after each shock (see Figure 6.1a) and the change in direction of the vertical velocity component after each shock (see Figure 6.1b). In addition to this, an expansion fan is visible after the point where the incident shock interacts with the shear layer. This is indicated by the acceleration of the horizontal flow field and the deflection of the vertical velocity component. Furthermore, in Figure 6.1b a weak Mach wave is visible, emanating from the leading edge of the panel (the leading edge itself is out of the FOV). This is created by the tiny steps

created by the clamping pieces, which are shown in Figure 3.3. It can be observed that close to the wall ($z/a < 0.026$), the flow field is not resolved. This is due to the masking procedure as described in subsection 4.1.1, to avoid the interference of the laser sheet reflection on the cross-correlation process. This unresolved region differs from case to case, and is larger for the flexible panels, where the laser reflections are expanded over a larger region as a consequence of the unsteady behaviour of the panel.

Additionally, the mean flow fields for both the open-cavity and the ventilated case are considered, which are presented together in Figure 6.2. By quick comparison, the flow fields show similar flow features and the small differences that are present (e.g. the separation region) are not treated in this section.

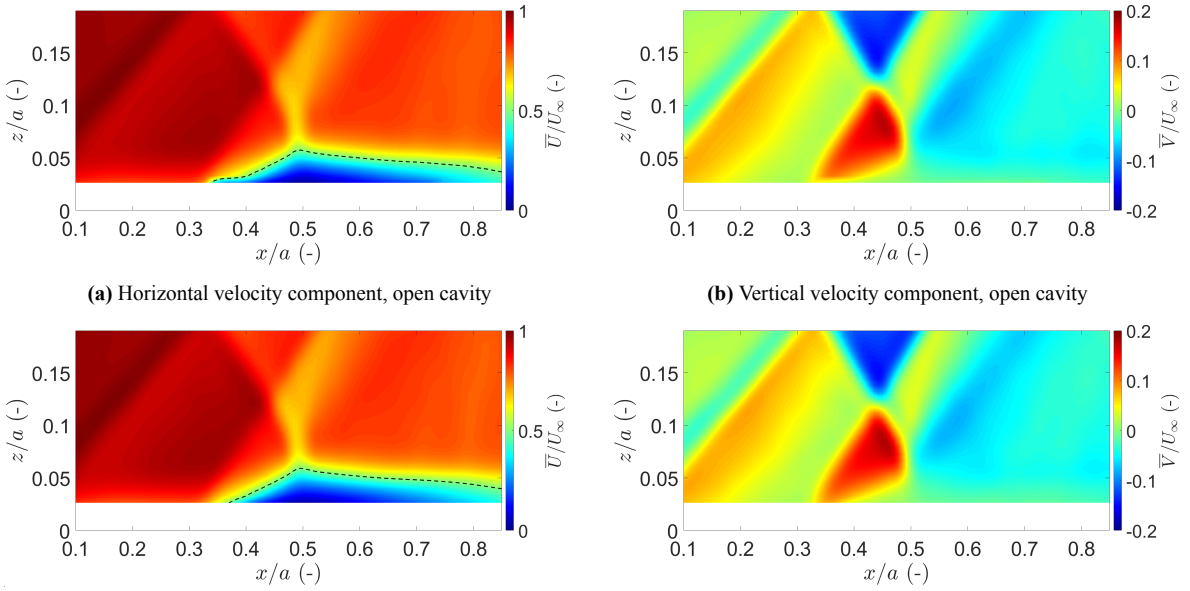

(a) Horizontal velocity component, open cavity

(b) Vertical velocity component, open cavity

(c) Horizontal velocity component, ventilated cavity

(d) Vertical velocity component, ventilated cavity

Figure 6.2: Mean horizontal (left) and vertical (right) velocity components over the mid-span of a panel with open cavity (upper) and the ventilated case (lower).

The most noticeable difference between the rigid and flexible panels is the leading edge wave. This difference is the most visible in the vertical velocity components, where there is a strong flow deflection upwards. Additionally, the magnitude of the velocity drops by a factor 0.96, which also shows that this wave can not be considered a Mach wave anymore, but as a weak shock wave. The reason why this wave is stronger compared to the baseline case is because of the upward deflection of the panel at the leading edge, as is shown in Figure 5.6. As the flow turns into itself, a compression wave is formed. Finally, the RD case is considered, which in terms of mean surface deformation corresponds to the cases as shown in Figure 6.2. However, in this case, the panel was not allowed to move, therefore it does not exhibit any dynamic deformations around the mean.

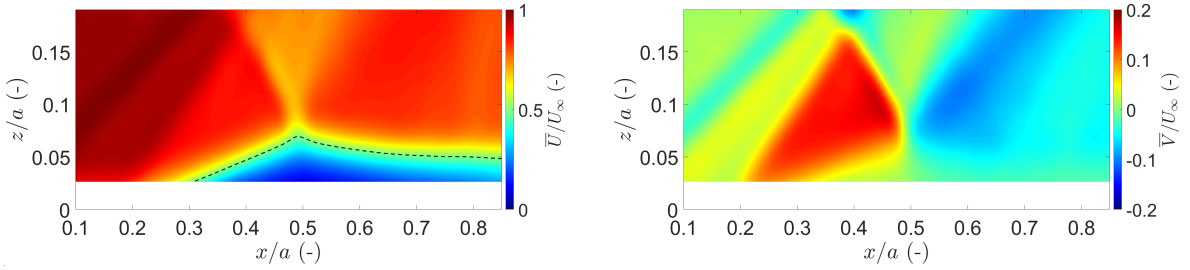

(a) Horizontal velocity component

(b) Vertical velocity component

Figure 6.3: Mean horizontal (left) and vertical (b) velocity components over the mid-span of a rigid mean deformed panel.

Upon inspection of the flow field, there are quite some noticeable differences. First of all, the leading edge shock seems to be weaker with respect to the flexible panels. Nonetheless, there is a small upward deflection of the flow (see Figure 6.3b) because of this leading edge phenomenon, due to the mean upward curvature of the panel at its start. From an overall comparison between the cases, it can therefore be concluded that in presence of a mean upward deflection of the panel at its leading edge, a stronger compression wave is formed, substantially deflecting the flow upward with respect to the rigid baseline case. When comparing the flexible and RD panels, it would be expected that because of the up-and-down motion of the panel around the mean, the flow would turn upward more and less in time respectively. Yet, for the flexible panels this deflection is stronger than for the rigid case. As the PDF of the panel motions (see Figure 5.7) does not show a particular bias towards an upward or downward motion, this difference is probably not due to any non-linear effects of the panel motion, but rather due to mismatches of the panel model when clamped inside the wind-tunnel.

Another significant difference is the larger separation area and the upstream shift of the reflected shock wave. In Figure 6.3a it is even shown that, on average, the separation region extends to above $z = 0$. Due to this upstream shift, the reflected shock wave also interacts at a more upstream location with the impinging shock wave, thus increasing the "triangular" region between the separation bubble, reflected shock wave and transmitted shock wave. The location of the reflected shock wave corresponds to the point of maximum mean displacement of the panel (at the centreline), suggesting that for a rigid plate, the mean deformation of the plate could drive the point of separation. This theory is reinforced by the fact that after the point of maximum deflection, the plate moves down, thus making the flow turn onto itself, in turn creating compression waves. This compression creates an adverse pressure gradient that makes the flow more prawn to separation. Further discussion on the separation dynamics is left to section 6.3.

It must me noted that the ventilated and RD cases showed an anomaly with respect to the other cases, which is not visible in Figure 6.3. From the cross-correlation results, the freestream velocity for these cases resulted to be equal to $U_\infty \approx 575\,\mathrm{m/s}$, which is in large contrast to $U_\infty \approx 500\,\mathrm{m/s}$ for the other cases. The reason for this difference can be linked to an incident during the experimental campaign, where one of the BNC cables, connecting the laser to the PTU, broke. The tests after this incident (the test order is shown in Table A.4) were the ventilated and RD cases. This makes it highly likely that in the pursuit of the problem source, some laser settings were changed, thus changing the time between two frames for the last two runs. Other sources for this differences can be excluded as follows: assuming the velocity would be physical, it would mean that also the Mach number would have changed from $M = 2.0$ to $M = 2.27$, as the total temperature and pressure did not change in between the runs. Theoretically, the total temperature needed for the flow to be at $M = 2.0$ would follow from:

$$T_0 = T_\infty \left(1 + \frac{\gamma - 1}{2} M^2\right) = \frac{a^2}{\gamma R}\left(1 + \frac{\gamma - 1}{2} M^2\right) = \frac{U_\infty^2}{M^2 \gamma R}\left(1 + \frac{\gamma - 1}{2} M^2\right), \tag{6.1}$$

using the isentropic flow relations and that $a = \sqrt{\gamma RT}$. Using $U_\infty = 575\,\mathrm{m/s}$ and $M = 2$ in Equation 6.1 results in $T_0 = 372\,\mathrm{K}$. This shows that either the total temperature consistently increased for two runs by around 80 K or that the Mach number increased. The first was not observed (T_0 was always around 293 K), and can therefore be excluded. The latter can be excluded for the reason that mechanically speaking, is is highly unlikely that the wind tunnel, using a Mach block designed for $M = 2$, would suddenly produce a higher Mach number. Furthermore, by inspection of the two similar cases in Figure 6.2, a significant Mach effect would have to be observed after normalising the flow velocities with the respective freestream velocities. As this is also not the case, it is concluded with high confidence that the observed difference in absolute velocity is due to acquisition software differences as a consequence of issues during the experimental campaign, rather than the velocities being physical.

6.2 Interaction Length

First, the mean interaction length is characterised. In general, the interaction length is defined by the distance between the reflected shock foot and the projected point of the impingement shock at the surface. In previous research performed by Allerhand (2020) and Aditya (2022), two different approaches were taken for shock foot location. Allerhand directly used the reflected shock wave, while Aditya projected the transmitted reflected shock onto the surface. Both methods are used in this section for comparison. For a more detailed discussion on the projection method, refer to subsection 4.3.5. The results for the study of the interaction length are presented in Table 6.1. The projected shock locations are normalised with the panel length a and the interaction length with the boundary layer thickness δ_{99}.

Table 6.1: Impinging shock and reflected shock foot locations projected with different methods and the resulting interaction lengths for different cavity closure conditions.

Case	x_{imp}/a	$x_{refl,foot}/a$	L_{int} [mm]	L_{int}/δ_{99}	$x_{refl,proj}/a$	$L_{int,proj}$ [mm]	$L_{int,proj}/\delta_{99}$
Rigid	0.579	0.268	39.10	7.52	0.268	34.32	6.60
Open	0.592	0.287	38.17	7.34	0.300	36.45	7.01
Ventilated	0.593	0.292	40.00	7.69	0.296	39.57	7.61
Closed	0.597	0.292	39.31	7.56	0.296	38.90	7.48
RD	0.594	0.183	52.61	10.12	-	-	-

From the results in Table 6.1 a couple of observations can be made. First of all, following the approach of Allerhand (2020), the interaction length seems to decrease when going from the rigid flat panel to the flexible panels. This is in direct contrast with the observations of both Allerhand and Aditya (2022), where it was concluded that the flexible panels increased this interaction region. However, a direct comparison with Allerhand might not be possible because a different impingement location was used. At the same time, the findings do not agree with Aditya, who used the same impingement location.
The reason for the discrepancy in results can be found when using the interaction length method used by Aditya. The changes in projected shock foot locations with respect to the method of Allerhand mainly shows that, especially for the rigid case, the reflected shock and the transmitted shock shift significantly with respect to one another (e.g. see Figure 6.1). This is likely due to the differences in interaction between the leading edge wave and the impingement shock between the different cases. Although this was not captured within the FOV, it is for this reason that the projection of the impingement shock does not correspond to the chosen inviscid projection point of 0.55. This shift is clearly visible once a mean deformation is introduced, making the leading edge wave stronger compared to the rigid flat panel, as discussed in section 6.1. Moreover, as was already clearly visible from Figure 6.3, the interaction length of the rigid deformed panel is much larger than the other cases because of the upstream shift of the reflected shock wave. No data for the location of the reflected shock using the method used by Aditya is presented in Table 6.1, as there not enough points could be taken on the transmitted shock. This is due to the reflected shock wave interaction more upstream with the impinging shock, thus moving al-

most all of the transmitted reflected shock out of the FOV. Although the method used by Aditya shows closer agreement to what was found by Allerhand and Aditya, it is believed that the method used by Allerhand is more accurate, and the specific conditions and strength of the leading edge wave can have a significant effect on the defined interaction length.

6.3 Separation Region

Strongly connected to the interaction region, is the separation region. Similar to Allerhand, an equal, cropped FOV is chosen for all the cases for fair comparison, even if some cases have more vectors closer to the wall. The separation region for all the cases between $x/a = 0.2 - 0.85$ and $z/a = 0.03 - 0.08$ is shown in Figure 6.4 in terms of the probability of separation. This is calculated as the percentage of negative vectors in a specific point which have a negative velocity taken over all the frames in time. Doing this for all the points results in the probability contours shown in the figure.

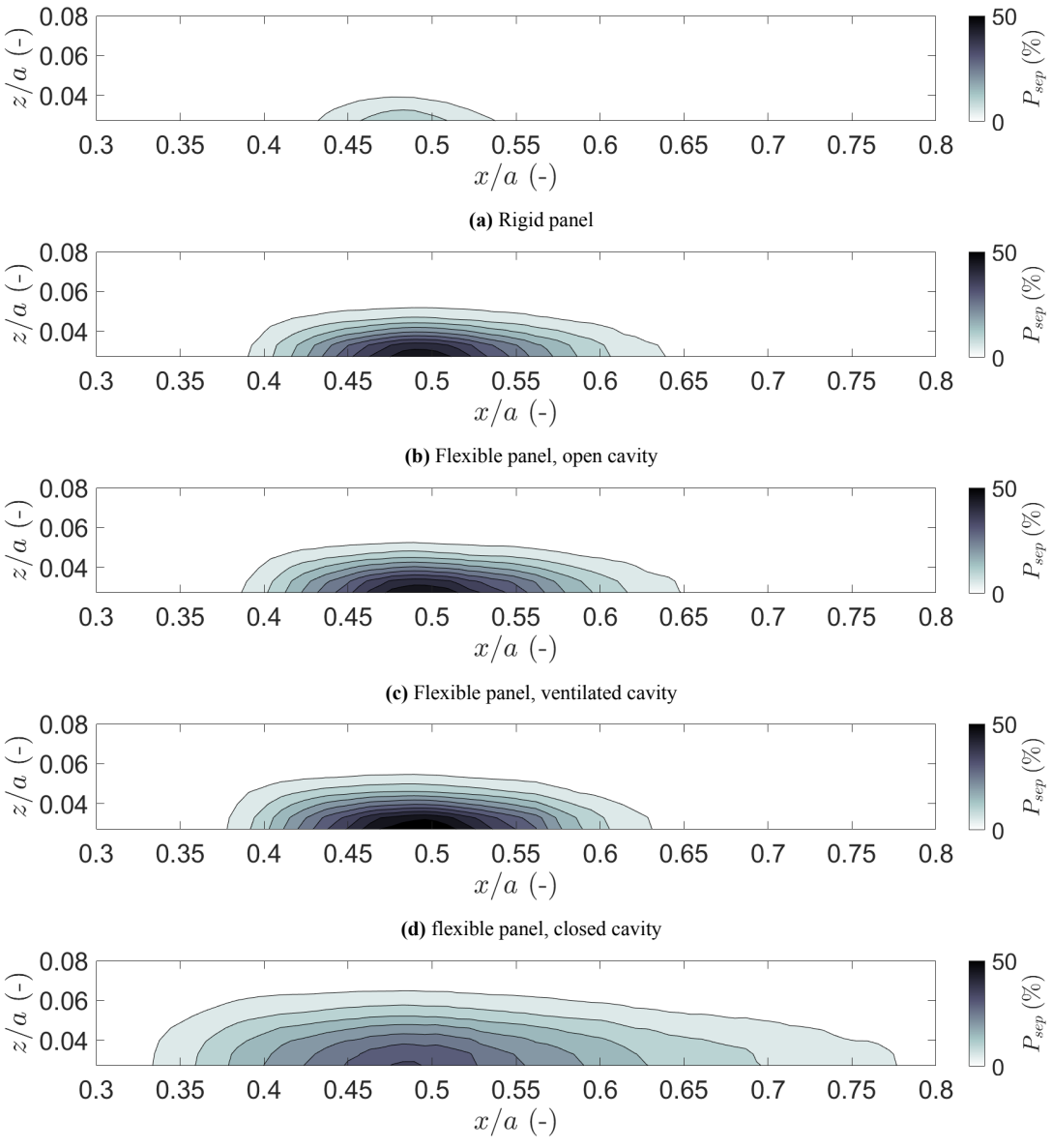

(a) Rigid panel

(b) Flexible panel, open cavity

(c) Flexible panel, ventilated cavity

(d) flexible panel, closed cavity

(e) Rigid mean deformed panel

Figure 6.4: Separation probability at panel mid-span plate for different cavity closure conditions.

What is remarkable is that while the interaction length was larger for the rigid flat plate compared to the flexible plates, the separation area is much smaller. This is probably due to the fact that the separation region is largely determined by the static deformation of the flexible panels, while the location of the reflected and impinging shock wave location does not vary significantly. A way to quantify this is by integrating the probability distribution over the shown area, as proposed by Giepman et al. (2018):

$$A_{sep} = \iint P_{sep}(x, z)dxdz, \tag{6.2}$$

where A_{sep} is the separation area and P_{sep} the probability distribution as a function in space. As shown in Table 6.2, indeed A_{sep} is the smallest for the rigid case. This would be even more evident when taking vectors closed to the surface, which are not visible in the current FOV. For the flexible cases, the panel even goes to negative z-values, thus having an even larger separation region.

Table 6.2: Mean separation area for investigated cases at panel mid-span location in the range $x/a = 0.2 - 0.8$ and $z/a = 0.03 - 0.08$.

Case	A_{sep}/δ_{99}^2
Rigid	0.134
Open	0.79
Ventilated	0.84
closed	0.95
RD	1.49

As stated at the start of this chapter, it is possible to observe the effect of both mean and dynamic deformations, as there are three cases with similar mean deformation but different dynamic deformations. While from the mean flow fields in section 6.1 it might not have been directly visible, Figure 6.4 reveals an interesting trend. First of all, a mean deformation already partially drives the separation area; the best would be to have a flat rigid plate. However, once a mean deformation is present, the smaller the dynamic deformations, the larger the separation. This trend arises by observing the differences between the open-cavity case, where the oscillations are the largest, the ventilated case, where the oscillations are less (see Figure 5.7), and the RD case, where there are no oscillations.

Although the general separation features for the baseline and flexible cases agree, the results for the RD case seem to be in direct contrast with Laguarda et al. (2024). In that research, it was argued that the main flow features, such as reflected shock location and separation area, are determined by the mean deformation, while the dynamic motion has a negligible effect. This is supported by results from other research such as Brouwer et al. (2017, where static deformations are shown to have a great impact on the separation characteristic. At the same time, this research also concludes that depending on the forcing of the flow by the dynamic panel oscillations, the separation length might change too. The discrepancy obtained in the current research with Laguarda et al. (2024) might be due to a number of factors. First of all, the panel boundary conditions were not the same, as Laguarda et al. (2024) used a panel with free sides. Therefore, even if the PIV was performed at the mid-plane, the separation area can be affected by three-dimensional effects, induced both by the wind tunnel boundaries (see section 5.1) and the three-dimensional deformation of the panel. A numerical study by Kokkinakis et al. (2023) shows how in particular the spanwise distribution is affected by three-dimensional modes, and thus indicates the importance of including three-dimensional effects when comparing two separate cases. Furthermore, in the numeric simulation, the panel was kept at a constant temperature, while for the current study, not only the temperature changes over time, but the material used to 3D-print the mean deformation was different from aluminium, thus also creating a difference with the other cases in this study itself. Other studies, such as Zhu et al. (2017), have shown that the wall temperature not only can have an effect on

the panel deformations, but also on the separation area on top of the panel. The aforementioned study of Zhu et al., for example, suggests a formula which relates the wall temperature directly to the length of the separation bubble. Finally, the presence of the leading edge (shock) waves (not present in the study of Laguarda et al.) is also shown to have significant effects on the SWBLI structure downstream.

In spite of this, the current research agrees with Laguarda et al. that the presence of dynamic motion on a flexible panel can aggravate the undesirable features of SWBLI and therefore not be used as passive flow control devices. Moreover, an argument can be made that as for the ventilated case the panel deformation is similar to the open-cavity case (see Figure 5.6) and the panel oscillations are significantly less (Figure 5.7), the ventilated panel behaviour starts to converge towards a rigid, mean deformed panel. Hence, it is expected that it would display mean field characteristics in between the open-cavity and rigid deformed case. However, this is not the case, as instead the mean characteristics are very similar to the open-cavity case. Thus, either the ventilated case resembles a rigid deformed case and the theory of Laguarda et al. (2024) is found to be true for this study as well (meaning that for the rigid deformed panel in the current study, there are too many differences), or there are some dynamic motions by panel and reflected shock that keep the separated region to a certain extent. The latter can be caused by the dynamic motions energising the boundary layer. In addition to this, research by Kokkinakis et al. (2023) has shown that not only the deformation amplitude, but also the deformation rate plays an important role in the SWBLI response. However, for all these theories, the results produced in the current study do not provide sufficient closure.

6.4 Reflected Shock Wave Motion

After identifying both structural and flow features separately, this section aims to couple the two measurements to identify the fluid-structure interaction. This interaction was observed by Allerhand (2020), who did simultaneous DIC and PIV experiments, thus being able to directly compare the data taken in the exact same conditions. Allerhand, Aditya (2022) and Laguarda et al. (2024) all confirm that once coupled, the main frequency contribution of the separation shock foot motion becomes similar to the frequency of the first panel oscillation mode, thus identifying the fluid-structure interaction.

As described in subsection 4.3.5, computing the PSD on the obtained signal for the reflected shock wave motion should give its frequency of oscillation. Figure 6.5 shows both the obtained time history of the signal (for a restricted interval) and its respective PSD for the entire acquisition time. For the cases where a flexible panel was used, also the spectral content of the panel motion from the DIC experiments are reported in the same plot, to identify any similarities.

From the open-cavity PSD, it is not directly evident that the panel and the shock are coupled together; only the high frequency content of both signals shows similar behaviour. Therefore, with the current data, the presence of fluid-structure interaction for the open-cavity case is unclear. In addition to this, it can be seen that most of the energy is contained in the higher frequency oscillations, which is confirmed by the fast oscillation of the signal in time (see left figure).

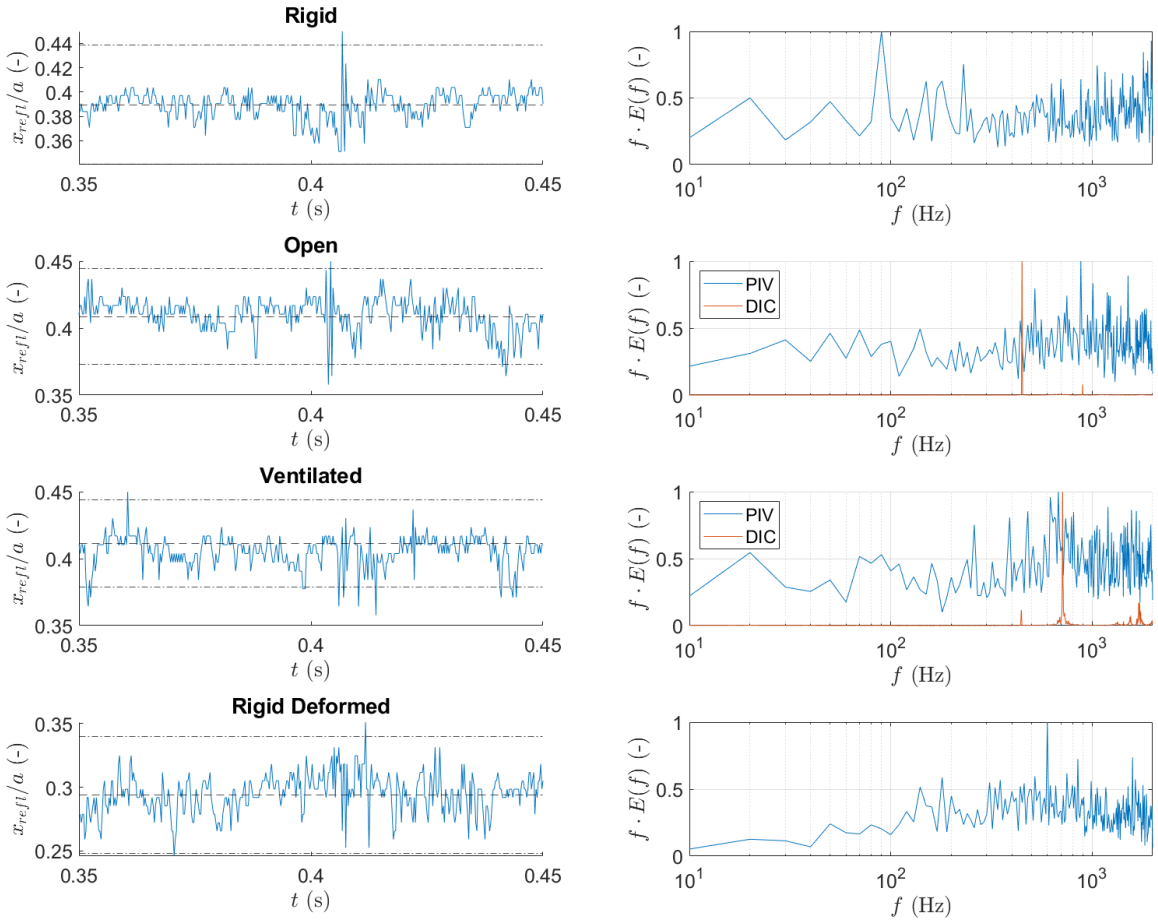

Figure 6.5: Reflected shock wave motion and its respective PSD for the different investigated cases, normalised with the maximum PSD value. PSD of the panel motion from the DIC experiments included for the flexible panels.

This can be solved in the future by increasing both the spatial and temporal resolution of the recordings.

A stronger argument can be made for the coupling of structure and flow for the ventilated case, as (broadband) peaks are present for the reflected shock motion at the locations of the sharp peaks of the panel motion. The difference in identification of fluid-structure coupling between the DIC and PIV runs uncovers a potential problem for the experimental research on this phenomenon inside the ST-15 wind tunnel facility. Previous studies on panel flutter inside the same facility have all mentioned the presence of specific wind tunnel vibrations, which sometimes also changed in between runs. As both previous and current studies have shown that these vibrations also go into the open cavity and start driving the panel motion, the results in Figure 6.5 suggest that these vibrations might have been different between the two runs. At the same time, the ventilated cavity case shows that potential changes in wind tunnel vibrations between runs going into the cavity are filtered out by the cavity plate, thus allowing for more valid comparisons between one run and another. This hypothesis is consistent with what was reported in section 5.2, which also highlights the significant difference between open and closed cavities in the ST-15 wind tunnel. Furthermore, discrepancies with schlieren measurements inside the cavity (see Figure 5.4) shows the difficulty in obtaining consistent measurements with the open cavity. Further investigation on these changing vibrations should be done by obtaining reliable data for proper analysis on the reflected shock wave motion for different cavity conditions.

When looking at the regular SWBLI case (rigid panel), most of the energy is contained in the lower frequency, as is characteristic for an SWBLI structure. For the same facility, (van Oudheusden et al., 2011) find this reflected shock wave unsteadiness to be present at frequencies below 200 Hz, even with broader peaks below 100 Hz. Furthermore, experiments from Dussauge et al. (2006) confirm this frequency regime for regular SWBLI, where instead of the frequency, the Strouhal number is reported ($S_L = fL_{sep}/U_\infty$). This Strouhal number range around 0.02-0.05 corresponds to these lower frequencies as reported above. When looking, however, at the RD case, a clear peak is present around 600 Hz, which would suggest that even if there is no dynamic motion, the mean deformed panel still triggers a periodic motion of the reflected shock wave. However, the results in the current study do not provide sufficient support for this conclusion, in particular because this is based on a singular experiment.

It is also possible to visualise the standard deviation of the vertical velocity component, as the fluctuation of this component in time can be used as an indicator for the shock motion because of its significant change over the shock (van Oudheusden et al., 2011). The standard deviation should then reveal the unsteadiness of this component and its main excursion domain. The standard deviation of the vertical velocity component for the cases considered is shown in Figure 6.6.

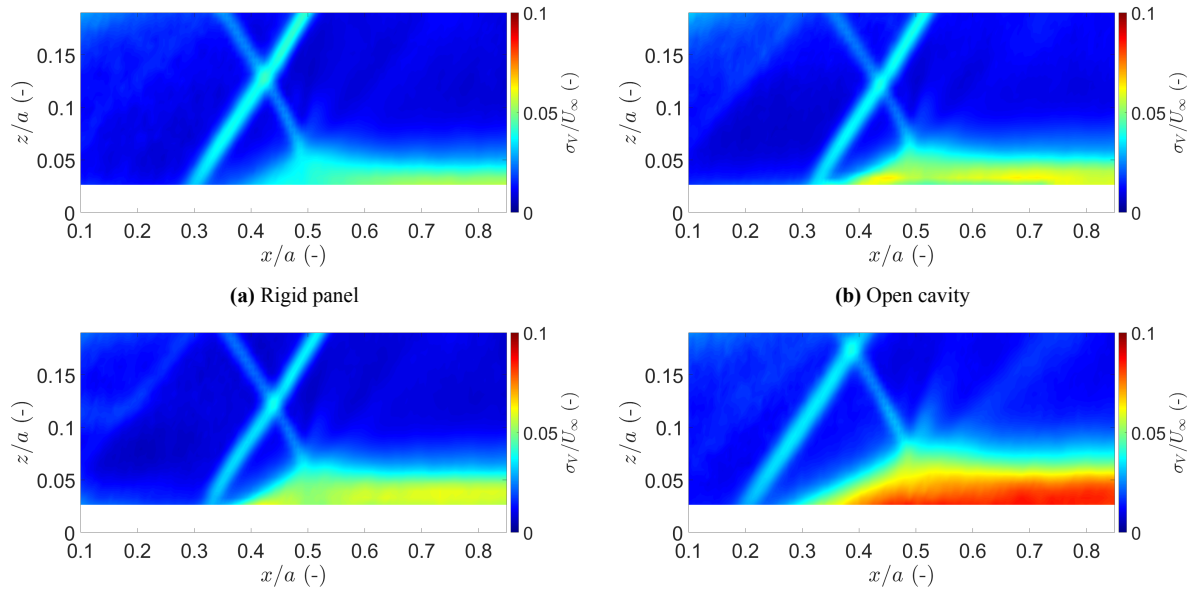

(a) Rigid panel

(b) Open cavity

(c) Ventilated cavity

(d) Rigid deformed panel

Figure 6.6: Standard deviation of vertical velocity component for investigated cases.

From Figure 6.6, there is no evident difference in the excursion of the reflected shock wave between the cases, except that for the ventilated case it seems a bit smaller. There is, however, a significant difference in the unsteadiness of the separation region, which is in agreement with what was discussed in section 6.3. Again, the unsteadiness of the reflected shock wave for the flexible panels are very similar, showing that in terms of mean quantities, despite the difference in amplitude and spectral content of oscillations, the two cases are much alike. Furthermore, the large unsteadiness found in the separation region for the RD case is in agreement with the larger separation area found for this configuration. A direct comparison with the other cases is, however, difficult as the interaction structure is shifted and the confidence in the correctness of the results is low.

7

Conclusions & Recommendations

The aim of this chapter is to present the most important results, based on the posed research objective and questions. The conclusions are presented in section 7.1, while the recommendations based on those conclusions are given in section 7.2.

7.1 Conclusions

In this research, an experimental investigation was conducted in the ST-15 wind tunnel facility at Delft University of Technology on shock-induced panel flutter. In particular, the objective was to study the effect of mean panel deformations on the fluttering behaviour of the panel and the shock structure over the panel. Previous studies in the same facility on this subject (Aditya, 2022; Allerhand, 2020; Mathijssen, 2022) have shown successfully the coupling between panel and flow, also known as fluid-structure interaction (FSI). However, all of these studies raised concerns on the presence of wind tunnel vibrations which could influence the FSI. Thus, the current study also put effort into documenting different sorts of boundary conditions present by experimenting inside a wind tunnel; one of these being the cavity closure, connecting flow downstream of the test section and the cavity underneath the test section. Similar test conditions to previous studies were used, which resulted in the use of a $0.3\,\text{mm}$, fully clamped thin panel of aspect ratio 1.5 (CCCC1.5) at a freestream Mach number and total pressure of $M_\infty = 2.0$ and $p_0 = 2.5$ bar, respectively.

Oil flow visualisation experiments were performed, aimed at understanding the three-dimensional effects present when testing inside a confined test section. Without the presence of a shock generator, the influence of the sidewalls is noticeable in the form of a small separation area. This however has a negligible effect on the centre of the panel. Furthermore, oil flow patterns on flexible plates show some streamline curvature, which can be directly linked to the deformation of the panel. These deformations, in turn, were connected to the measured pressure inside the cavity, where a higher pressure led to a more upward deformation, and lower pressure to an opposite deformation. The presence of a shock generator also resulted in the presence of a shock-wave/boundary-layer interaction (SWBLI) on top of the panel. The interaction of this shock structure with the walls of the wind tunnel resulted in three-dimensional effects, in particular on the spanwise difference in shape of the separation bubble. Again, based on the deformation of the angle, the separation area was affected in different ways: an upward deflection would reduce separation, while downward deflections would increase it. This is found to be consistent with the finding of Tripathi et al. (2021).

The difference in pressure between the runs was created by the closure of the cavity. In previous occasions, the cavity was always left open, meaning flow downstream of the test section was allowed to flow down into the cavity, because of the geometry of the ST-15 wind tunnel. Schlieren images performed in the current study showed strong pressure waves entering this cavity when open, which is in line with was observed by Aditya (2022). Following the recommendation by previous study in the same facility, tests were conducted where the cavity was closed. This was done in two ways: one where a plate closed off the entire cavity and one where the same plate had nine small holes in it. The latter case, also referred to as the ventilated case, was used such that the pressure inside the cavity would be equal to the

open-cavity case, without the strong pressure waves entering this area. Closing the cavity resulted in a higher cavity pressure, which would not go to a consistent value between several runs. Nevertheless, by use of the digital image correlation technique (DIC), the mean deformation for this case was found to be entirely above $z = 0$ and show fluttering behaviour at the aft part of the panel for certain cavity pressures. This is in contrast with the open-cavity and ventilated case, which displayed similar mean deformations (because of similar cavity pressure) in the form of a sine wave. The latter results, obtained with an inviscid impingement location of $x_{imp} = 0.55a$, is consistent with the shape found by Aditya (2022) at the same conditions. Comparing the open-cavity and ventilated cases showed a remarkable difference in fluttering behaviour. POD analysis showed that the open-cavity case is dominated by a first bending mode (92% relative energy content) at a frequencies of 489 Hz. The subsequent modes with a significant energy contribution oscillate at the harmonics of the first mode (898 Hz and 1347 Hz), indicating resonance behaviour of the panel motion. Closing the cavity, but leaving the nine holes open, resulted again in a similar first bending mode as the most dominant one, but with much lower relative energy content of 56%. Moreover, the panel would flutter at other frequencies with respect to the open-cavity case, without the presence of harmonics, suggesting that closing the cavity filters away the strong pressure waves coming inside this area and allowing the panel to oscillate "freely". Additionally, without the pressure waves forcing the panel into resonance, the oscillation amplitude is also lower for this case. Finally, phase-averaging analysis on the DIC results showed the division of the flutter motion into four phase, where the shape of the phases are completely dominated by the first bending modes.

In addition to the study on confinement effects and the motion of the panel, the current study also put some effort in documenting the thermal behaviour of the panel. This was done by means of infrared (IR) imaging on top of the panel and the use of T-type thermocouples (TC) at the bottom of the panel, inside the cavity. As expected, the flexible thin panels showed to cool down quicker than the rigid panels, because of their lower thermal inertia. Without the presence of the shock generator, the cavity temperature was observed to increase, most likely due to the strong pressure waves. Once closing the cavity, this temperature increase was shown to disappear. Significant temperatures up to 70 °C where observed at the bottom of the thin panel with open cavity, which by the current study are deemed non-physical, as that would mean that there would be a thermal gradient of 65 °C within the thickness of the panel, by connecting IR and TC data. Direct comparison of both techniques showed that the use of thermocouples might not be suitable for the quick temperature changes in time. Both with and without the shock generator, the temperature gradient, ΔT, between the thin portion and frame of the panel showed similar trends, where for the rigid panels, this temperature gradient would be close to zero, as the thickness is equal everywhere; for the thin cases, the panel would cool down more than for the open-cavity case, which is believed to be connected to the differences in cavity temperature between the cases. A longer test ($t_{acq} = 20$ s), highlighted the change in amplitude of the oscillations with respect to the mean over time, which is believed to be connected to the change in ΔT over time. This observation shows agreement with experiments by Brouwer et al. (2023).

In conclusion, the boundary condition that was found to be the strongest factor affecting the panel motion was the cavity closure. As a direct consequence of this, the cavity pressure was affected, having a strong influence on the mean deformation displaced by the panels. Additionally, temperature effects have been found to not be entirely negligible either over time.

Particle image velocimetry (PIV) data has shown that the mean SWBLI structure over the panel is highly dependent on the mean deformation. Direct comparison of a rigid flat plate and a rigid, manufactured panel, with the same mean deformation as the open-cavity and ventilated case, shows an increase in separation area and an upstream shift of the reflected shock wave, which is believed to be connected to the point where the mean deformation reaches its maximum. The presence of dynamic oscillations

shows a decrease in the separation area, where the more the panel vibrates, the smaller the separation area. Still, the separation area is larger than the rigid flat plate. Therefore, consistent with Laguarda et al. (2024), the presence of dynamic motion on a flexible panel is deemed undesirable and unfeasible as a form of passive flow control mechanism. However, the current research differs from Laguarda et al. (2024), as the rigid, mean deformed panel (RD) shows that the SWBLI structure is not only affected by the mean deformation of the panel, but also by the dynamic deformations. The current study brings forward different reasons for this discrepancy, such as the panel boundary conditions (all sides clamped compared to two sides free) and temperature effects (varying temperature in space and time compared to isothermal plate). These temperature effects might also cause the current study to show inconsistencies as the material used to 3D-print the mean deformed panel was different than the used aluminium for the other panels, creating different thermal responses of the panel. Finally, the presence of (strong) leading edge waves is shown to interact with the impinging shock wave, thus partially affecting the SWBLI structure. This leading edge wave was not present in the numerical study as this wave is induced by the clamping pieces inside the wind tunnel.

Finally, a comparison of PSD analysis on both the motion of the panel and the reflected shock wave showed agreement in the present frequencies for the ventilated case, suggesting the presence of FSI, as also found by previous studies (Aditya, 2022; Allerhand, 2020; Mathijssen, 2022). However, for the open-cavity case, this agreement was not found. Not only did the frequencies found between DIC and PIV not match, but they also did not match with frequencies found inside the cavity by means of schlieren imaging. It is therefore likely that between runs, something changes in the wind tunnel environment, thus also changing the present wind tunnel vibrations. With the open cavity, these vibrations are then able to travel inside the cavity and force the panel from underneath. The fact that these inconsistencies disappear when closing the cavity supports this argument, where closing the cavity can be seen as a filter to this vibrations and letting the panel move freely, and as a consequence, show consistent coupling with the panel for non-simultaneous measurements.

7.2 Recommendations

Although the concerns about wind tunnel vibrations affecting the study on the shock-induced panel flutter have been addressed in this study, a lot is still unclear about the source of these vibrations. This current study shows that closing the cavity would already be a way to get rid of resonance effects when studying the panel, but to make a strong case for the repeatability of results for non-simultaneous DIC and PIV measurements, more tests would have to be conducted at sufficiently high quality, such that the oscillations of the shock structures can be captured well. Furthermore, this would also give the chance to understand the impact of the mean deformation of the panel on the excursion of the reflected shock foot.

Moreover, it is not only proposed to completely close the cavity, but also to connect it to a pump, such that the cavity pressure can be set by the wind tunnel user. This would ensure consistent measurements and allow for making the panel flutter more or less, based on the flutter boundary of the panel. In general, before conducting any new fundamental research into shock-induced flutter in this facility, it is recommended to fully address the aforementioned wind tunnel vibrations, and whether or how they change between runs. This would ensure that future observations are easier to analyse, without the doubt whether the results are fully physical or due to any wind tunnel vibrations.

Finally, on the study of the effect of the mean deformation on the SWBLI structure, a couple of recommendations can be made. Firstly, it is proposed to design a rigid deformed panel out of the same material as the other panels (aluminium). This way, any phenomena introduced by differences in thermal behaviour are reduced to a minimum. Such a panel could be manufactured by use of different process such milling. Furthermore, it would be interesting to do a numerical study which does not use a CCFF panel, but a fully clamped CCCC panel of the same aspect ratio. This way, it could be studied whether three-dimensional panel behaviour has a significant effect on the shock structure. In addition to this, instead of using an isothermal panel, the use of a more physical thermal model would show thermal effects on the flow structure, if there are any. On the experimental side, to have more similar conditions to the numerical study of Laguarda et al. (2024), a two dimensional panel (i.e. deformation is equal across the whole span of the wind tunnel) could be manufactured, thus excluding any significant three-dimensional effect at the mid-span plane inside the wind tunnel.

References

Acosta, A. R., & Austin, J. M. (2024). Experimental Investigation of an Impinging Shock-Boundary Layer Interaction on a Compliant Panel in Mach 4 Flow. In *AIAA SCITECH 2024 Forum*. https://doi.org/10.2514/6.2024-1153

Aditya, A. (2022, February). *Experimental Study of Shock Wave/Boundary-Layer Interactions over Fluttering Panels* [Master's thesis, Delft University of Technology].

Allerhand, P. Q. (2020, August). *An Experimental Investigation of Shock-Induced Panel Flutter Using Simultaneous PIV and DIC* [Master's thesis, Delft University of Technology].

American Society for Testing and Materials. (1993). *Manual on the Use of Thermocouples in Temperature Measurement* (4th ed.).

Anderson, J. D. (2017). *Fundamentals of aerodynamics* (6th ed.). McGraw-Hill.

Aranyi, P., Janiga, G., Zehringer, K., & Thevenin, D. (2013). Analysis of different pod methods for piv-measurements in complex unsteady flows. *International Journal of Heat and Fluid Flow*, *43*, 204–211.

Babinsky, H., Oorebeek, J., & Cottingham, T. (2013). Corner effects in reflecting oblique shock-wave/boundary-layer interactions. *51st AIAA Aerospace Sciences Meeting including the New Horizons Forum and Aerospace Exposition*. https://doi.org/10.2514/6.2013-859

Babinsky, H., & Harvey, J. K. (2011, November). *Shock wave-boundary-layer interactions*. Cambridge University Press.

Beberniss, T. J., Spottswood, S. M., & Eason, T. (2011). High-speed digital image correlation measurements of random nonlinear dynamic response. *Conference Proceedings of the Society for Experimental Mechanics Series*, *6*, 171–186. https://doi.org/10.1007/978-1-4614-0222-0_22

Beberniss, T. J., Spottswood, S. M., Perez, R. A., & Eason, T. G. (2016). Nonlinear Response of a Thin Panel in a Multi-Discipline Environment: Part I - Experimental Results. *Conference Proceedings of the Society for Experimental Mechanics Series*, 237–248.

Beresh, S. J., Clemens, N. T., & Dolling, D. S. (2002). Relationship between upstream turbulent boundary-layer velocity fluctuations and separation shock unsteadiness. *AIAA Journal*, *40*, 2412–2422. https://doi.org/10.2514/2.1609

Boyer, N. R., McNamara, J. J., Gaitonde, D. V., Barnes, C. J., & Visbal, M. R. (2018). Features of shock-induced panel flutter in three-dimensional inviscid flow. *Journal of Fluids and Structures*, *83*, 490–506. https://doi.org/10.1016/j.jfluidstructs.2018.10.001

Boyer, N. R., McNamara, J. J., Gaitonde, D. V., Barnes, C. J., & Visbal, M. R. (2021). Features of panel flutter response to shock boundary layer interactions. *Journal of Fluids and Structures*, *101*. https://doi.org/10.1016/j.jfluidstructs.2020.103207

Brouwer, K. R., Gogulapati, A., & McNamara, J. J. (2017). Interplay of surface deformation and shock-induced separation in shock/boundary-layer interactions. *AIAA Journal*, *55*(12), 4258–4273. https://doi.org/10.2514/1.J056030

Brouwer, K. R., Perez, R. A., Beberniss, T. J., & Spottswood, S. M. (2023). Aeroelastic response of a thin panel excited by a separated shock–boundary layer interaction. *Physics of Fluids*, *35*. https://doi.org/10.1063/5.0175161

Brouwer, K. R., Perez, R. A., Beberniss, T. J., Spottswood, S. M., & Ehrhardt, D. A. (2021a). Fluid-structure interaction on a thin panel including shock impingement effects. *AIAA Scitech 2021 Forum*. https://doi.org/10.2514/6.2021-0910

Brouwer, K. R., Perez, R. A., Beberniss, T. J., Spottswood, S. M., & Ehrhardt, D. A. (2021b). Experiments on a thin panel excited by turbulent flow and shock/boundary-layer interactions. *AIAA Journal*, *59*, 2737–2752. https://doi.org/10.2514/1.J060114

Bruce, P. J. K., Burton, D. M. F., Titchener, N. A., & Babinsky, H. (2011). Corner effect and separation in transonic channel flows. *Journal of Fluid Mechanics*, *679*, 247–262. https://doi.org/10.1017/jfm.2011.135

Clemens, N. T., & Narayanaswamy, V. (2014). Low-frequency unsteadiness of shock wave/turbulent boundary layer interactions. *Annual Review of Fluid Mechanics*, *46*, 469–492. https://doi.org/10.1146/annurev-fluid-010313-141346

D'Aguanno, A. (2023). *Physics and control of transonic buffet* [Doctoral dissertation, Delft University of Technology].

D'Aguanno, A., Allerhand, P., Schrijer, F., & van Oudheusden, B. (2023). Characterization of shock□induced panel futter with simultaneous use of dic and piv. *Experiments in Fluids*, *64*. https://doi.org/10.1007/s00348-022-03551-1

Délery, J., & Dussauge, J.-P. (2009). Some physical aspects of shock wave/boundary layer interactions. *Shock Waves*, *19*, 453–468. https://doi.org/10.1007/s00193-009-0220-z

Doerffer, P., Hirsch, C., Dussauge, J.-P., Babinsky, H., & Barakos, G. N. (2010, November). *Unsteady Effects of Shock Wave induced Separation* (1st ed.). Springer. https://doi.org/10.1007/978-3-642-03004-8

Dolling, D. S. (2001). Fifty years of shock-wave/boundary-layer interaction research: What next? *AIAA Journal*, *39*, 1517–1531. https://doi.org/10.2514/2.1476

Dowell, E. H. (1970). Panel flutter: A review of the aeroelastic stability of plates and shells. *AIAA Journal*, *8*, 385–399. https://doi.org/10.2514/3.5680

Dowell, E. H. (1972). *Panel flutter* (tech. rep.). NASA Langley Research Center.

Dowell, E. H. (1974). *Aeroelasticity of plates and shells* (1st ed.). Springer.

Dowell, E. H., & Bendiksen, O. (2010, December). *Panel flutter*. Wiley. https://doi.org/10.1002/9780470686652.eae152

Dupont, P., Haddad, C., Ardissone, J. P., & Debiève, J. F. (2005). Space and time organisation of a shock wave/turbulent boundary layer interaction. *Aerospace Science and Technology*, *9*, 561–572. https://doi.org/10.1016/J.AST.2004.12.009

Dussauge, J.-P., Dupont, P., & Debiève, J.-F. (2006). Unsteadiness in shock wave boundary layer interactions with separation. *Aerospace Science and Technology*, *10*(2), 85–91. https://doi.org/https://doi.org/10.1016/j.ast.2005.09.006

Ganapathisubrama, B., Clemens, N. T., & Dolling, D. S. (2007). Effects of upstream boundary layer on the unsteadiness of shock-induced separation. *Journal of Fluid Mechanics*, *585*, 369–394. https://doi.org/10.1017/S0022112007006799

Giepman, R. H. M., Schrijer, F. F. J., & van Oudheusden, B. W. (2018). A parametric study of laminar and transitional oblique shock wave reflections. *Journal of Fluid Mechanics*, *844*, 187–215. https://doi.org/10.1017/jfm.2018.165

Gramola, M., Bruce, P. J., & Santer, M. (2020). Response of a 3d flexible panel to shock impingement with control of cavity pressure. *AIAA Scitech 2020 Forum*, *1 PartF*, 1–17. https://doi.org/10.2514/6.2020-0314

Grilli, M., Schmid, P. J., Hickel, S., & Adams, N. A. (2012). Analysis of unsteady behaviour in shock-wave turbulent boundary layer interaction. *Journal of Fluid Mechanics*, *700*, 16–28. https://doi.org/10.1017/jfm.2012.37

Grossman, I. J., & Bruce, P. J. K. (2019). Sidewall gap effects on oblique shock-wave/boundary-layer interactions. *AIAA Journal*, *57*(6), 2649–2652. https://doi.org/https://doi.org/10.2514/1.J057952

Humble, R. A., Elsinga, G. E., Scarano, F., & van Oudheusden, B. W. (2009). Three-dimensional instantaneous structure of a shock wave/turbulent boundary layer interaction. *Journal of Fluid Mechanics*, *622*, 33–62. https://doi.org/10.1017/S0022112008005090

Kingsbury, N. R. (1990). *Aerospace technology: Technical data and information on foreign test facilities* (tech. rep.). U.S. General Accounting Office.

Kislaya, A. (2016, August). *Estimation and reduction of peak-locking errors in PIV measurements* [Master's thesis, Delft University of Technology].

Kokkinakis, I. W., Drikakis, D., Spottswood, S. M., Brouwer, K. R., & Riley, Z. B. (2023). High-speed shock-boundary-layer interaction over deformed surfaces. *Physics of Fluids*, *35*. https://doi.org/10.1063/5.0172475

Laguarda, L., Hickel, S., Schrijer, F. F. J., & van Oudheusden, B. W. (2024). Shock-wave/turbulent boundary-layer interaction with a flexible panel. *Physics of Fluids*, *36*. https://doi.org/10.1063/5.0179082

Ligrani, P. M., McNabb, E. S., Collopy, H., Anderson, M., & Marko, S. M. (2020, December). Recent investigations of shock wave effects and interactions. https://doi.org/10.1186/s42774-020-0028-1

Mathijssen, L. C. J. M. (2022, January). *An experimental study on supersonic panel flutter using simultaneous digital image correlation & schlieren* [Master's thesis, Delft University of Technology].

McKeon, B., & Engler, R. (2007). Pressure measurement systems. In C. Tropea, A. L. Yarin, & J. F. Foss (Eds.), *Springer handbook of experimental fluid mechanics* (pp. 179–214). Springer Berlin Heidelberg. https://doi.org/10.1007/978-3-540-30299-5_4

Melling, A. (1997). Tracer particles and seeding for particle image velocimetry. *Experiments in Fluids*, *8*, 1406–1416.

Meng, X., Ye, Z., Ye, K., & Liu, C. (2020). Analysis on location of maximum vibration amplitude in panel flutter. *Proceedings of the Institution of Mechanical Engineers, Part G: Journal of Aerospace Engineering*, *234*, 457–469. https://doi.org/10.1177/0954410019876529

Morgan, B., Duraisamy, K., Nguyen, N., Kawai, S., & Lele, S. K. (2013). Flow physics and rans modelling of oblique shock/turbulent boundary layer interaction. *Journal of Fluid Mechanics*, *729*, 231–284. https://doi.org/10.1017/jfm.2013.301

Muhlstein, L., Gaspers, P. A., & Riddle, D. W. (1968). *An experimental study of the influence of the turbulent boundary layer on panel flutter* (tech. rep.). NASA Langley Research Center.

Pan, B., Xie, H., Wang, Z., Qian, K., & Wang, Z. (2008). Study on subset size selection in digital image correlation for speckle patterns. *Opt. Express*, *16*(10), 7037–7048. https://doi.org/10.1364/OE.16.007037

Pasha, A. A., & Sinha, K. (2012). Simulation of hypersonic shock/turbulent boundary-layer interactions using shock-unsteadiness model. *Journal of Propulsion and Power*, *28*, 46–60. https://doi.org/10.2514/1.B34191

Pasquariello, V. (2018). *Analysis and contol of shock-wave / turbulent boundary-layer interactions on rigid and flexible walls* [Doctoral dissertation, Technischen Universität München].

Pasquariello, V., Hickel, S., Adams, N., Hammerl, G., Pasquariello, V., Hickel, S., Adams, N. A., Hammerl, G., Wall, W. A., Daub, D., Willems, S., & Gülhan, A. (2015). Coupled simulation of shock-wave/turbulent boundary-layer interaction over a flexible panel. https://www.researchgate.net/publication/279512920

Pasquariello, V., Hickel, S., & Adams, N. A. (2017). Unsteady effects of strong shock-wave/boundary-layer interaction at high reynolds number. *Journal of Fluid Mechanics*, *823*, 617–657. https://doi.org/10.1017/jfm.2017.308

Piponniau, S., Dussauge, J. P., Debiève, J. F., & Dupont, P. (2009). A simple model for low-frequency unsteadiness in shock-induced separation. *Journal of Fluid Mechanics*, *629*, 87–108. https://doi.org/10.1017/S0022112009006417

Poggie, J., Bisek, N. J., Kimmel, R. L., & Stanfield, S. A. (2015). Spectral characteristics of separation shock unsteadiness. *AIAA Journal*, *53*, 200–214. https://doi.org/10.2514/1.J053029

Priebe, S., Wu, M., & Martín, M. P. (2009). Direct numerical simulation of a reflected-shock-wave/turbulent-boundary- layer interaction. *AIAA Journal*, *47*, 1173–1185. https://doi.org/10.2514/1.38821

Raffel, M., Kähler, C., Willert, C., Wereley, S., Scarano, F., & Kompenhans, J. (2018). *Particle Image Velocimetry: A Practical Guide* (3rd). Springer. https://doi.org/10.1007/978-3-319-68852-7

Ragni, D., Schrijer, F., van Oudheusden, B., & Scarano, F. (2011). Particle tracer response across shocks measured by piv. *Journal of Fluid Mechanics*, *50*, 53–64. https://doi.org/https://doi.org/10.1007/s00348-010-0892-2

Reu, P. (2013). Stereo-rig design: Lighting—part 5. *Experimental Techniques*, *37*(3), 1–2. https://doi.org/https://doi.org/10.1111/ext.12020

Roncella, R., Romeo, E., Barazzetti, L., Gianinetto, M., & Scaioni, M. (2012). Comparative analysis of digital image correlation techniques for in-plane displacement measurements. *2012 5th Inter-*

national Congress on Image and Signal Processing, 721–726. https://doi.org/10.1109/CISP.2012.6469731

Sabnis, K., & Babinsky, H. (2023). A review of three-dimensional shock wave–boundary-layer interactions. *Progress in Aerospace Sciences*, *143*, 100953. https://doi.org/10.1016/J.PAEROSCI.2023.100953

Scanivalve. (n.d.). *DSA3217/3218 Series Pressure Scanner Digital Sensor Array: Operation and Service Manual*. Scanivalve Corporation. Liberty Lake, WA.

Schreier, H., Orteu, J.-J., & Sutton, M. A. (2009). *Image Correlation for Shape, Motion and Deformation Measurements: Basic Concepts, Theory and Applications* (1st ed.). Springer. https://doi.org/https://doi.org/10.1007/978-0-387-78747-3

Settles, G. S. (2001). *Schlieren and Shadowgraph Techniques: Visualizing Phenomena in Transparent Media* (1st ed.). Springer-Verlag Berlin Heidelberg GmbH.

Shahriar, A., & Shoele, K. (2024). Nonlinear shock-induced flutter of a compliant panel using a fully coupled fluid-thermal-structure interaction model. *Journal of Fluids and Structures*, *124*, 104047. https://doi.org/10.1016/j.jfluidstructs.2023.104047

Shinde, V. J., & Gaitonde, D. V. (2022). Features of oblique shock wave turbulent boundary layer interaction. *AIAA Science and Technology Forum and Exposition, AIAA SciTech Forum 2022*. https://doi.org/10.2514/6.2022-1975

Shinde, V. J., McNamara, J., Gaitonde, D., Barnes, C., & Visbal, M. (2019). Transitional shock wave boundary layer interaction over a flexible panel. *Journal of Fluids and Structures*, *90*, 263–285. https://doi.org/10.1016/J.JFLUIDSTRUCTS.2019.07.007

Shinde, V. J., McNamara, J. J., Gaitonde, D. V., Barnes, C. J., & Visbal, M. R. (2018). Panel flutter induced by transitional shock wave boundary layer interaction. *2018 Fluid Dynamics Conference*. https://doi.org/10.2514/6.2018-3548

Sirovich, L. (1967). Turbulence and the dynamics of coherent structures. i - coherent structures. ii - symmetries and transformations. iii - dynamics and scaling. *Quarterly of Applied Mathematics*, *45*, 561–571. https://doi.org/10.1090/qam/910463

Solomon Jr, O. M. (1991). *PSD Computations Using Welch's Method* (tech. rep.). Sandia National Labs. Albuquerque, NM (United States).

Souverein, L. J., Dupont, P., Debiève, J. F., Dussauge, J. P., Oudheusden, B. W. V., & Scarano, F. (2010). Effect of interaction strength on unsteadiness in turbulent shock-wave-induced separations. *AIAA Journal*, *48*, 1480–1493. https://doi.org/10.2514/1.J050093

Spottswood, S. M., Eason, T., & Beberniss, T. (2012). Influence of shock-boundary layer interactions on the dynamic response of a flexible panel. *Proceedings of the ISMA-2012*, 603–616.

Spottswood, S. M., Beberniss, T. J., Eason, T. G., Perez, R. A., Donbar, J. M., Ehrhardt, D. A., & Riley, Z. B. (2019). Exploring the response of a thin, flexible panel to shock-turbulent boundary-layer interactions. *Journal of Sound and Vibration*, *443*, 74–89. https://doi.org/10.1016/j.jsv.2018.11.035

Sun, Z. (2014). *Micro ramps in supersonic turbulent boundary layers: An experimental and numerical study* [Doctoral dissertation, Delft University of Technology].

Tripathi, A., Gustavsson, J., Shoele, K., & Kumar, R. (2021). Response of a compliant panel to shock boundary layer interaction at mach 2. *AIAA Scitech 2021 Forum*, 1–15. https://doi.org/10.2514/6.2021-0489

Tripathi, A., Sheehan, M., Gustavsson, J., & Kumar, R. (2024). Effect of mach number on fluid structure interaction over a compliant panel. *AIAA SCITECH 2024 Forum*. https://doi.org/10.2514/6.2024-2676

van Oudheusden, B., Jöbsis, A., Scarano, F., & Souverein, L. (2011). Investigation of the unsteadiness of a shock-reflection interaction with time-resolved particle image velocimetry. *Shock Waves*, *50*, 397–409. https://doi.org/https://doi.org/10.1007/s00193-011-0304-4

Varigonda, S., & Narayanaswamy, V. (2023). Fluid structure interactions generated by an oblique shock impinging on a thin elastic panel. *Journal of Fluids and Structures*, *119*, 103890. https://doi.org/https://doi.org/10.1016/j.jfluidstructs.2023.103890

Vedeneev, V. V. (2012). Panel flutter at low supersonic speeds. *Journal of Fluids and Structures*, *29*, 79–96. https://doi.org/10.1016/j.jfluidstructs.2011.12.011

Visbal, M. (2014). Viscous and inviscid interactions of an oblique shock with a flexible panel. *Journal of Fluids and Structures*, *48*, 27–45. https://doi.org/10.1016/j.jfluidstructs.2014.02.003

Wang, B., Sandham, N. D., Hu, Z., & Liu, W. (2015). Numerical study of oblique shock-wave/boundary-layer interaction considering sidewall effects. *Journal of Fluid Mechanics*, *767*, 526–561. https://doi.org/10.1017/jfm.2015.58

Welch, P. (1967). The use of fast fourier transform for the estimation of power spectra: A method based on time averaging over short, modified periodograms. *IEEE Transactions on Audio and Electroacoustics*, *15*, 70–73.

Willems, S., Gülhan, A., & Esser, B. (2013). Shock induced fluid-structure interaction on a flexible wall in supersonic turbulent flow, 285–308. https://doi.org/10.1051/eucass/201305285

Williams, R. D., & Babinsky, H. (2022). Corner effects on the unsteady behaviour of compression corner shock wave/boundary layer interactions. *AIAA Science and Technology Forum and Exposition, AIAA SciTech Forum 2022*. https://doi.org/10.2514/6.2022-1181

Xiang, X., & Babinsky, H. (2019). Corner effects for oblique shock wave/turbulent boundary layer interactions in rectangular channels. *Journal of Fluid Mechanics*, *862*, 1060–1083. https://doi.org/10.1017/jfm.2018.983

Zhou, H., Wang, G., Li, Q. Z., & Liu, Y. (2023). Numerical study on the nonlinear characteristics of shock induced two-dimensional panel flutter in inviscid flow. *Journal of Sound and Vibration*, *564*. https://doi.org/10.1016/j.jsv.2023.117893

Zhu, X.-K., Yu, C.-P., Tong, F.-L., & Li, X.-L. (2017). Numerical study on wall temperature effects on shock wave/turbulent boundary-layer interaction. *AIAA Journal*, *55*(1), 131–140. https://doi.org/10.2514/1.J054939

A

Test Matrices Experimental Campaigns

Campaign 1: Schlieren

Table A.1: Test matrix for Schlieren test campaign. θ_{SG} = shock generator angle, RP = rigid plate, TP = fully clamped thin plate with $AR = 1.5$, C = closed cavity, O = open cavity, T_0 = total temperature inside settling chamber, p_0 = total pressure set in wind tunnel.

Run No	Date & Time	$\theta_{SG}[^\circ]$	Panel	Cavity	$T_0[^\circ C]$	p_0[bar]
1	09/02/24 & 10h15	12	RP	C	18.1	2.5
2	09/02/24 & 10h55	12	TP	C	17.9	2.5
3	09/02/24 & 11h02	12	TP	O	17.1	2.5
4	09/02/24 & 12h10	12	RP	O	17.6	2.5
5	09/02/24 & 13h21	15	RP	O	17.7	2.5
6	09/02/24 & 13h46	15	RP	C	17.4	2.5
7	09/02/24 & 14h10	15	TP	C	17.4	2.5
8	09/02/24 & 14h23	15	TP	O	16.2	2.5
9	09/02/24 & 15h28	NO	TP	O	17.4	2.5
10	09/02/24 & 15h38	NO	TP	C	16.5	2.5
11	09/02/24 & 16h05	NO	RP	C	16.8	2.5
12	09/02/24 & 16h14	NO	RP	O	16.0	2.5

Campaign 2: Infrared Imaging and Oil Flow Visualisation

Table A.2: Test matrix for infrared imaging and oil flow visualisation test campaign. IR = infrared imaging, OFV = oil flow visualisation, θ_{SG} = shock generator angle, RP = rigid plate, TP = fully clamped thin plate with $AR = 1.5$, C = closed cavity, O = open cavity, T_0 = total temperature inside settling chamber, p_0 = total pressure set in wind tunnel.

Run No	**Date & Time**	Technique	$\theta_{\mathbf{SG}}[^\circ]$	**Panel**	**Cavity**	$\mathbf{T_0}[^\circ\mathbf{C}]$	$\mathbf{p_0}$**[bar]**
1	13/03/24 & 14h40	IR	NO	TP	O	17.7	2.5
2	13/03/24 & 15h02	IR	NO	TP	C	17.1	2.5
3	14/03/24 & 16h45	IR	NO	TP	O	17.6	2.5
4	14/03/24 & 17h10	IR	NO	TP	C	17.1	2.5
5	15/03/24 & 14h23	IR	NO	TP	O	18.2	2.5
6	15/03/24 & 15h00	IR	NO	TP	C	17.1	2.5
7	15/03/24 & 16h10	IR	NO	TP	O	17.2	2.5
8	18/03/24 & 08h55	IR	NO	TP	O	17.7	2.5
9	18/03/24 & 10h25	IR	NO	RP	O	17.3	2.5
10	18/03/24 & 11h05	IR	NO	RP	C	16.7	2.5
11	18/03/24 & 12h02	IR	NO	RP	C	14.6	2.5
12	18/03/24 & 14h12	IR	12	RP	C	17.1	2.5
13	18/03/24 & 15h00	IR	12	RP	O	17.0	2.5
14	18/03/24 & 16h15	IR	12	TP	O	17.0	2.5
15	18/03/24 & 16h45	IR	12	TP	C	16.3	2.5
16	19/03/24 & 11h43	OFV	12	TP	C	18.6	2.5
17	19/03/24 & 14h24	OFV	12	TP	C	18.4	2.5
18	19/03/24 & 16h17	OFV	12	TP	O	18.1	2.5
19	20/03/24 & 09h05	OFV	12	RP	O	17.7	2.5
20	20/03/24 & 10h04	OFV	12	RP	C	17.5	2.5
21	20/03/24 & 11h05	OFV	12	TP	C	17.1	2.5
22	20/03/24 & 12h01	OFV	NO	RP	C	17.1	2.5
23	20/03/24 & 13h45	OFV	NO	TP	O	17.1	2.5
24	20/03/24 & 14h57	OFV	NO	RP	O	17.1	2.5
25	20/03/24 & 16h00	OFV	NO	TP	C	17.3	2.5
26	16/04/24 & 14h27	OFV	12	TP	C	18.6	2.5
27	16/04/24 & 15h20	OFV	12	TP	O	17.8	2.5

Campaign 3: Digital Image Correlation

Table A.3: Test matrix for DIC test campaign. θ_{SG} = shock generator angle, RP = rigid plate, TP = fully clamped thin plate with $AR = 1.5$, C = closed cavity, CO = closed but with open holes, O = open cavity, f_{acq} = acquisition frequency, T_0 = total temperature inside settling chamber, p_0 = total pressure set in wind tunnel.

Run No	Date & Time	$\theta_{SG}[^\circ]$	Panel	Cavity	f_{acq}[kHz]	$T_0[^\circ C]$	p_0[bar]
1	27/05/24 & 17h13	12	TP	O	5	19.1	2.5
2	28/05/24 & 09h01	12	TP	CO	5	18.9	2.5
3	28/05/24 & 10h34	12	TP	C	5	18.8	2.5
4	28/05/24 & 13h06	12	TP	CO	5	19.0	2.5
5	28/05/24 & 16h03	12	TP	C	5	18.9	2.5
6	28/05/24 & 16h19	12	TP	O	5	18.4	2.5
6	28/05/24 & 16h30	12	TP	O	0.4	18.2	2.5
7	29/05/24 & 14h10	12	RP	O	5	19.0	2.5

Campaign 4: Particle Image Velocimetry

Table A.4: Test matrix for PIV test campaign. θ_{SG} = shock generator angle, RP = rigid plate, TP = fully clamped thin plate with $AR = 1.5$, RD = rigid deformed plate, C = closed cavity, CO = closed but with open holes, O = open cavity, f_{acq} = acquisition frequency, T_0 = total temperature inside settling chamber, p_0 = total pressure set in wind tunnel.

Run No	Date & Time	$\theta_{SG}[^\circ]$	Panel	Cavity	f_{acq}[kHz]	$T_0[^\circ C]$	p_0[bar]
1	07/06/24 & 11h23	12	RP	O	4	19.0	2.5
2	07/06/24 & 13h15	12	TP	O	4	19.5	2.5
3	07/06/24 & 13h40	12	TP	C	4	19.4	2.5
4	07/06/24 & 16h10	12	TP	CO	4	19.5	2.5
5	07/06/24 & 16h49	12	RD	O	4	20.1	2.5

B

Technical Drawings

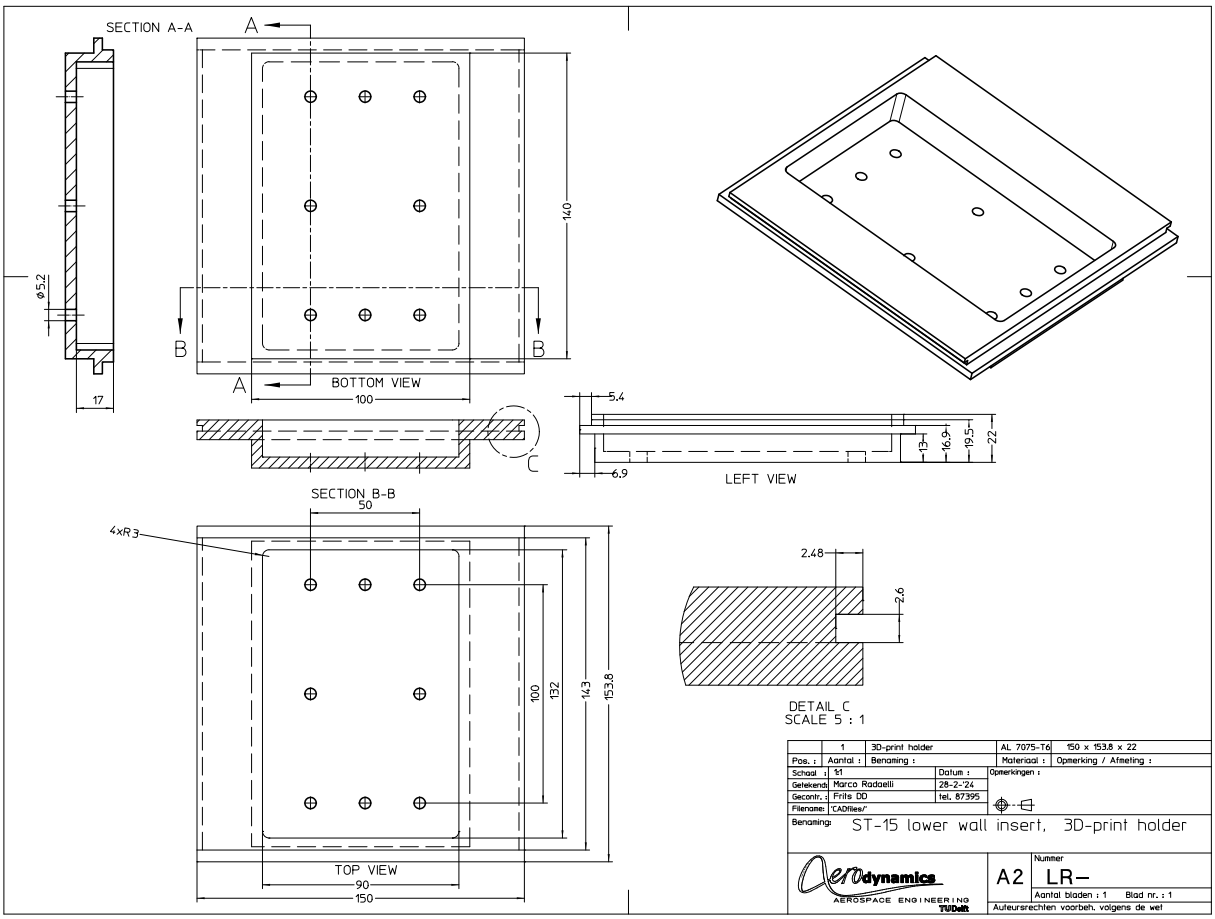

Figure B.1: Technical drawing of ST-15 lower wall insert, designed as a holder for 3D printed panels.

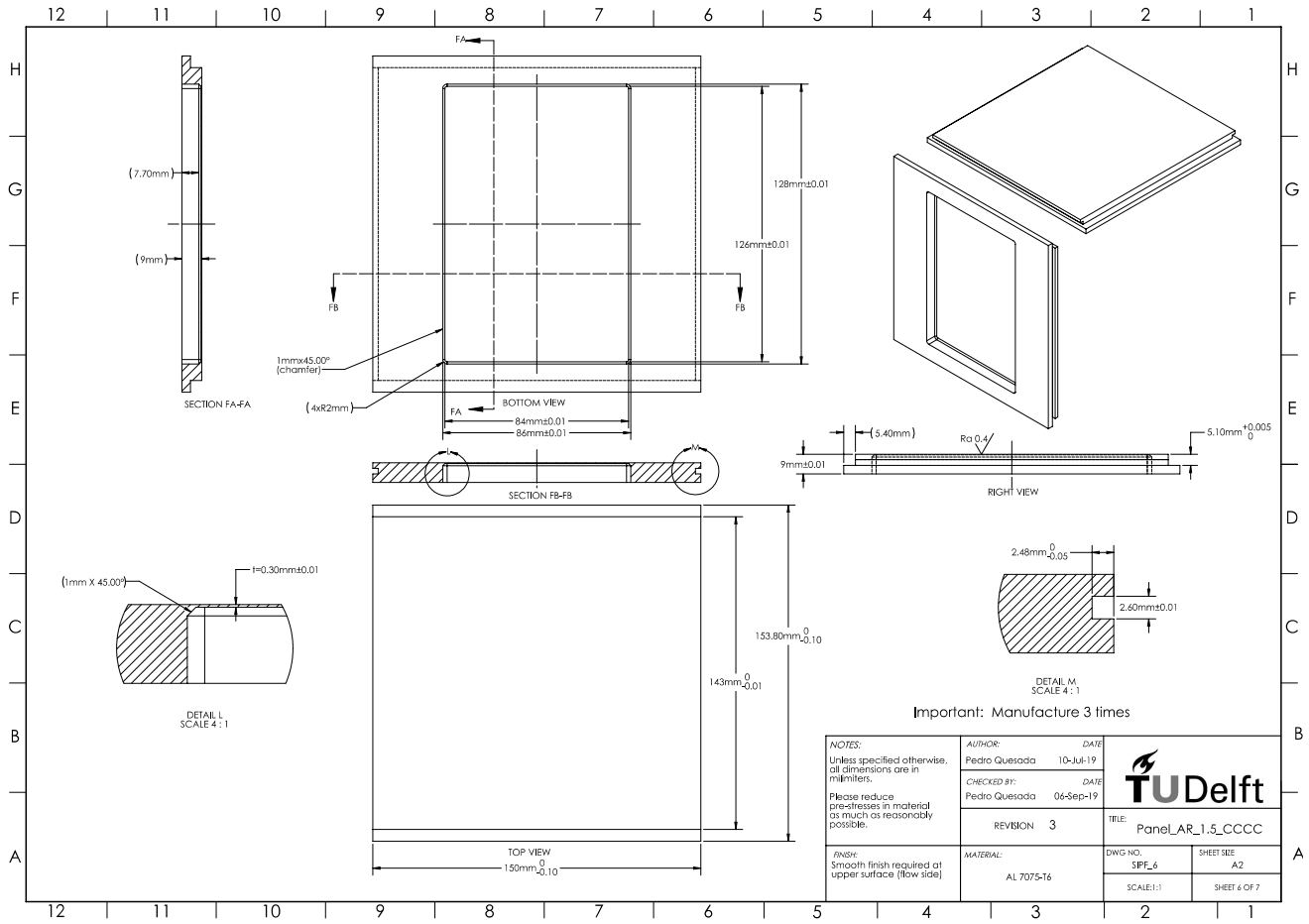

Figure B.2: Technical drawing of fully clamped thin panel (0.3 mm) with AR = 1.5 (Allerhand, 2020).